Formation of Biomimetic Membranes on Inorganic Supports of Different Surface Morphology and Macroscopic Geometry

by

Carrie Eggen

A Dissertation Presented in Partial Fulfillment
of the Requirements for the Degree
Doctor of Philosophy

Approved April 2011 by the
Graduate Supervisory Committee:

Jerry Y.S. Lin, Chair
Lenore Dai
Kaushal Rege
Trevor Thornton
Bryan Vogt

ARIZONA STATE UNIVERSITY

May 2011

ABSTRACT

Biological membranes are critical to cell sustainability by selectively permeating polar molecules into the intracellular space and providing protection to the interior organelles. Biomimetic membranes (model cell membranes) are often used to fundamentally study the lipid bilayer backbone structure of the biological membrane. Lipid bilayer membranes are often supported using inorganic materials in an effort to improve membrane stability and for application to novel biosensing platforms. Published literature has shown that a variety of dense inorganic materials with various surface properties have been investigated for the study of biomimetic membranes. However, literature does not adequately address the effect of porous materials or supports with varying macroscopic geometries on lipid bilayer membrane behavior. The objective of this dissertation is to present a fundamental study on the synthesis of lipid bilayer membranes supported by novel inorganic supports in an effort to expand the number of available supports for biosensing technology. There are two fundamental areas covered including: (1) synthesis of lipid bilayer membranes on porous inorganic materials and (2) synthesis and characterization of cylindrically supported lipid bilayer membranes.

The lipid bilayer membrane formation behavior on various porous supports was studied via direct mass adsorption using a quartz crystal microbalance. Experimental results demonstrate significantly different membrane formation behaviors on the porous inorganic supports. A lipid bilayer membrane structure was formed only on SiO_2 based surfaces (dense SiO_2 and silicalite, basic conditions) and γ-alumina (acidic conditions). Vesicle monolayer adsorption was observed on γ-alumina (basic conditions), and yttria stabilized zirconia (YSZ) of varying roughness. Parameters such as buffer pH, surface chemistry and surface roughness were found to have a significant impact on the vesicle adsorption kinetics. Experimental and modeling work was conducted to study formation and characterization of cylindrically supported lipid bilayer membranes. A novel sensing technique (long-period fiber grating refractometry) was utilized to measure the formation mechanism of lipid bilayer membranes on an optical fiber. It was found that the membrane formation kinetics on the fiber was similar to its planar SiO_2 counterpart. Fluorescence measurements verified membrane transport behavior and found that characterization artifacts affected the measured transport behavior.

To my mother, father, and sister

for their continuous support and encouragement.

ACKNOWLEDGMENTS

This dissertation is dedicated to my family for their continuous support during my graduate studies. Their continued prayers, encouragement and understanding are the only reason I am where I am today. I am especially thankful to my sister for her careful and thoughtful revisions of this dissertation.

I would like to thank my advisor, Dr. Jerry Lin, for introducing me to academic research and a novel and exciting research area. His dedication to research, his management style and his commitment to fostering student independence will continue to influence me throughout my career. I would like to thank Dr. Lenore Dai, Dr. Kaushal Rege, Dr. Trevor Thornton, and Dr. Bryan Vogt for their valuable time and effort to serve on my committee.

I am grateful for Dr. Hai Xiao at the Missouri University of Science and Technology for allowing me to spend months in his lab with unlimited use of his resources and students. Special thanks go to Tao Wei, John Montoya, and Hongbiao Duan for their expertise in optical sensors and their willingness to help with my project. Also, I am thankful to Dr. Bryan Vogt for allowing me to use his lab, equipment and resources. Much of this work would not be possible without his generosity. I would also like to thank Dr. Alexander Zolochevsky and Galyna Goncharova from Kharhov Polytechnic University (Kharkov, Ukraine) for their expertise in mathematical modeling and their assistance with this project.

I would like to thank current and previous group members for their support and friendship throughout the years because without them I wouldn’t be where I am today: Teresa Rosa, Matt Anderson, Shriya Seshadri, Tyler Norton, Nick Linneen, Jay Kniep, Jessica O'Brien-Abraham, Deepak Singh, Xiaoli Ma, Mikel Duke, Vineet Gupta, Qinghua Yin, Xiaotong Wei, Jiansheng Li, Masakoto Kenazashi, Bo Lu, Haibing Wang, Jose Landeros, Zhenxia (Fiona) Zhao, Zebao (Peter) Rui, Chao Ji, and Ding Wang. Very special thanks are in order to Teresa Rosa for her valuable time and careful revisions of this dissertation.

Many thanks go to Fred Peña for his continued technical support and friendship during my undergraduate and graduate years at ASU. Additionally, I would like to thank various staff members at Arizona State University for their assistance in a wide variety of ways throughout my graduate career: Zhenquan Liu (assistance with SEM); Doug Daniel (assistance with confocal microscopy); Kenneth Mossman (assistance with AFM); Timothy Karcher (assistance with thin film deposition); Emmanuel Soignard (assistance with XRD); David Ladner (assistance with DLS); Paul Westerhoff (use of the DLS); Michael Dodson (assistance with contact angle and FTIR measurements); Cecile Rondeau (assistance with chemical ordering); Claire Zanakis (department accounting); Paul Grillos (academic advising); Brian Goehner (academic advising).

TABLE OF CONTENTS

Page

Chapter

APPENDIX

APPENDIX Page

LIST OF TABLES

Table Page

LIST OF FIGURES

Figure Page

Figure Page

Figure Page

LIST OF PREVIOUS PUBLICATIONS

The following chapters are modified versions of papers published or to be submitted for publication:

Chapter 2

Eggen, C.L., Wang, H., Lu, Bo., Vogt, B.D., Lin, Y.S. (2011) Formation of Lipid Bilayer Membranes and Vesicle Monolayer Adsorption on Porous Inorganic Supports. *Acta Biomaterialia*, Manuscript in preparation.

Chapter 3

Eggen, C.L., Lin, Y.S., Wei, T., Xiao, H. (2010). Detection of lipid bilayer membranes formed on silica fibers by double-long period fiber grating laser refractometry. (2010). *Sensors and Actuators B, 150*, 734–741

Chapter 4

Eggen, C.L., Goncharova, G., Zolochevsky, A., Lin, Y.S. (2011). A Modeling and Experimental Study on the Lateral Fluidity of Lipid Membranes Supported on a Silica Optical Fiber. *Journal of Non-Crystalline Solids*, Manuscript in preparation.

Chapter 1

GENERAL INTRODUCTION

1.1. Cell membranes

Cells are the fundamental building blocks of every living creature, plants or animals, and are responsible for the efficient function of a living organism. Each cell is composed of several different components that together enable the cell to optimally function. The three most important organelles include the nucleus (functions in the cell to replicate DNA and RNA), mitochondria (energy production), and endoplasmic reticulum (protein synthesis). The cell is encapsulated within a plasma (cell) membrane for both protection of the cell interior from the extracellular environment and for maintaining ion gradients across the membranes [Campbell & Farrell, 2003].

The backbone of the cell membrane is a lipid bilayer membrane, a structure that prevents the transport of the majority of molecules in the intracellular space. The cell membrane is embedded with a variety of biomolecules, each with a specific and important role for cell function. Proteins embedded within the bilayer allow selective transport of ions specific to that particular protein; for example, Gramicidin allows for selective transport of monovalent ions (such as Na^+) but rejects divalent ions (such as Ca^{2+}) [Alvarez-Leefmans & Delpire, 2009]. Molecular recognition is completed by receptors; for example, an important receptor type is for low-density lipoproteins, which regulate cholesterol within the bloodstream [Campbell & Farrell, 2003].

Structural integrity of the membrane is maintained through cholesterol embedded within the bilayer membrane [Campbell & Farrell, 2003].

1.2. Lipid bilayer membranes

The lipid bilayer membrane is comprised of amphipathic molecules, molecules with both polar and non-polar properties. Phospholipids are commonly utilized in lipid bilayer synthesis and are composed of one polar head group and two hydrocarbon tails. Phosolipids are characterized by two traits: (1) the length and degree of saturation of the hydrophobic tail, and more importantly, (2) the structure of the polar head. The structure of the polar head group is defined by the nature of the second alcohol esterified with various molecules to the phosphoric acid.

The five most important phospholipids are summarized in Figure 1-1. The moieties summarized in Figure 1-1b-f are the portions of the head group (Figure 1-1a) that are esterified in the phosphoric acid (at the circled “x” location). The head group structure defines the overall molecular charge, which is heavily influenced by the esterified moiety. In Figure 1-1a, the hydrophobic tails are denoted by R_1 and R_2, and often have different chain lengths and degrees of saturation within the same lipid molecule.

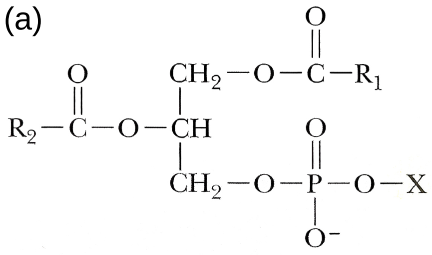

(b) $-CH_2CH_2\overset{+}{N}(CH_3)_3$ (c) $-CH_2CH\left(\overset{+}{N}H_3\right)COO^-$

(d) $-CH_2CH_2NH_3^+$ (e) $-CH_2CH(OH)CH_2OH$

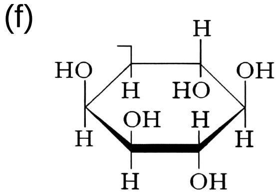

Figure 1-1. Typical lipid structures (b-f) esterifed to the (a) phosphoric acid - (b) choline, (c) serine, (d) ethanolamine, (e) glycerol and (f) inositol.

While the head group charge may vary, aqueous immersed double-tailed lipids self-assemble to form a lipid bilayer structure (see Figure 1-1). The hydrophilic portion is denoted by the sphere, while the hydrophobic tails are denoted by the two tails. As shown in Figure 1-2, the lipid bilayer structure is a double layer of lipid molecules that are arranged to minimize water exposure to the hydrophobic portion of the lipid molecule.

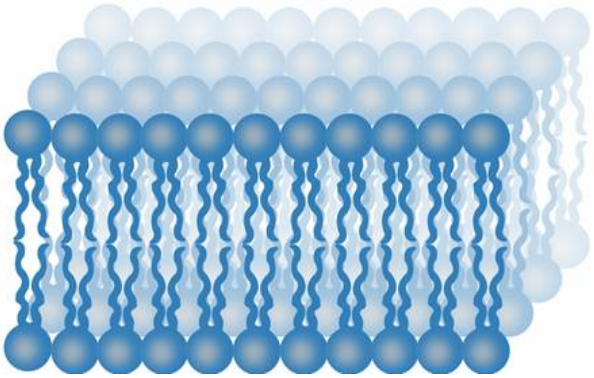

Figure 1-2. Schematic of the lipid bilayer membrane structure.

1.3. Model lipid bilayer membranes

The cell membrane is a complex structure composed of lipids and proteins. Cell membranes are important to the efficient function of the cell's interior organelles with its rigid, impermeable native structure as well as the ability to selectively transport ions with embedded proteins. While the role of the cell membrane as a whole is well understood, the exact mechanism of each individual membrane component is not well known. The role of the lipid bilayer membrane backbone (without other embedded cellular components) in cell membrane behavior is important to isolate and is of great interest in current research efforts. Isolation of lipid bilayer membrane behavior will enhance the understanding of the dynamic binding and/or transmembrane behaviors while eliminating the influence from the bilayer structure itself.

Lipid bilayer membranes (termed biomimetic membranes if serving as a cell membrane model) have become accepted models for cell membranes, as they possess similar properties (e.g., bilayer structure, impermeability to polar molecules without embedded proteins). The simple membrane model allows for a study of lipid bilayer membranes in a controlled setting in order to isolate bilayer functions. This allows the scientific community to decouple the behavior of the lipid bilayer and embedded proteins.

1.4. Unsupported membranes

Early work studying lipid bilayer membranes involved aperture supported membranes, and are often termed black lipid membranes. This free-spanning configuration allows for accessibility of each side of the membrane, which would allow for the study of ionic transport across the membrane structure. Typically, the aperture diameter is on the micron scale [Wiedemann et al., 2004], but recent work has synthesized submicron apertures for applications to unsupported membrane work [Han et al., 2007; Simon et al., 2007].

A significant advantage to unsupported lipid bilayer membranes is that its structure is similar to its native in vivo state and thus the natural behavior of the membrane can be observed. Additionally, the unsupported membrane allows for natural embedding of proteins, which promotes their natural function within a lipid bilayer membrane. These two advantages allow for the study of protein function; this behavior is often measured using electrochemical techniques (such as impedance spectroscopy [Purrucker et al., 2004] or cyclic voltametry [Wiedemann et al., 2004]). Typical properties of unsupported lipid membranes can be found in Table 1-1 below.

Table 1-1. *Typical synthetic lipid bilayer membrane properties*

Property	Variable	Value	Reference
Breakdown voltage	V_b	2.5×10^6 V	Tien & Ottova-Leitmannova, 2003
Equilibrium potential over SPB	V_e	0 V	Tien & Ottova-Leitmannova, 2003
Capacitance	C_m	0.5 – 1 μF/cm^2	Tien & Ottova-Leitmannova, 2003
Compressibility coefficient		~5 N/m^2	Hladky & Gruen 1982
Diffusion coefficient on glass	D_{total}	1-8 μm^2/s	Salafsky et al., 1996 Stelzle et al., 1992 Groves & Boxer, 1995
Refractive Index	N	1.45-1.53	Salamon & Tollin, 2001 Shouten et al., 1999
Resistance	R_m	10^8-10^9 Ωcm^2	Tien & Ottova-Leitmannova, 2003
Typical interfacial free energy (surface tension)		0.8-2 mJ/m^2	Nehr et al., 1977, Hladky & Gruen, 1982 Tien & Ottova, 2001
Viscosity	V	~10-3 kg/ms	Tien & Ottova-Leitmannova, 2003 Larsson et al., 2003
Water permeability		8-24 μm/s	Tien & Ottova-Leitmannova, 2003

While unsupported lipid membranes can be very useful, the membranes are often very unstable and are difficult to prepare [Reimhult, 2006]. The final membrane structure is very sensitive to contamination. The preparation process involves the evaporation of a solvent, and if residuals are present, it may affect membrane properties, such as thickness, elasticity and electrical properties [Reimhult, 2006]. Additionally, unsupported membranes are rarely stable for more than a few hours [Tien, & Ottova-Leitmannova, 2003], which limits its characterization (and general usefulness) beyond short term electrical conductance measurements.

1.5. Supported membranes

To improve the limitations presented by unsupported lipid bilayer membranes, research has been focused on supported lipid bilayer membrane systems. Supported lipid bilayer membranes have significantly improved membrane stability from hours to days [Purrucker et al., 2001]. There are several types of supports that have been investigated, including dense, porous and spherical supports.

1.5.1. Dense planar supported membranes

Supported lipid bilayer membranes are lipid bilayer membranes tethered to a support surface. A wide variety of supporting materials have been used for lipid membrane deposition in an effort to expand the materials available for industrial applications. Many types of dense supports with various surface properties have been intensely studied to fundamentally understand how lipid membranes interact with support surfaces. The most common support used is SiO_2 (silica glass) [Johnson et al., 2002] due to its wide availability. Other common oxide (or of similar structure) supports include SiN_3 [Reimhult et al., 2003], TiO_2 [Hennesthal & Steinem, 2000; van Oudenaarden & Boxer, 1999; Starr and Thompson, 2000], $SrTiO_3$ [Starr and Thompson, 2000], and ITO [Groves et al., 1998]. Common metals used are gold [Groves, et al., 1998;

Richter et al., 2003], silver [Knoll, 1998], aluminum [Hennesthal & Steinem, 2000], platinum [Tjarnhage & Puu, 1996; Puu & Gustafson, 1997], and chromium [Groves et al., 1998]. Organic materials, such as gels [Lu et al., 1996; Uto et al., 1994] and grafted polymers [Sackmann & Tanaka, 2000; Tanaka & Sackmann, 2005] have been used as supports for lipid bilayer membranes.

It has been found that the bilayer membrane structure or properties are significantly affected by the support material. Published work has determined that while the support materials improve stability, the surface properties (such as chemistry or degree of hydrophilicity) directly affect the final structure of the lipid bilayer membrane in addition to the intra- and inter-membrane transport properties. Within literature, only glass, SiO_2, and Si_3N_4 supports have promoted the formation of lipid bilayer membranes. Other hydrophilic materials have shown vesicle monolayer adsorption without rupture; the reason for this phenomenon is not completely understood. Bilayer formation and interaction with the support is discussed in detail in subsequent sections.

While there are numerous benefits of supported bilayer membranes, the support material can inhibit natural membrane behavior. Published literature has shown that a small water layer with a thickness of 10 Å exists between the support surface and the lipid bilayer membrane [Zwang et al., 2010], providing a small separation distance between the two materials. While this separation distance exists, it does not provide sufficient distance for successful incorporation of protein ion channels that would function in their native state. The close proximity to the support surface causes the proteins to denature and become tethered to the support thus quenching their functionality [Castellana & Cremer, 2006]. The dense nature of the support also eliminates the accessibility of both sides of the membrane which would promote transmembrane gradient studies.

1.5.2. Planar porous supported lipid bilayer membranes

Porous supports offer the dual advantage of stability enhancement offered by the dense supports as well as providing easy access to each side of the membrane for applications in ionic transport. Limited work has been done to expand the availability of porous supports to bilayer membrane technology. Hennesthal & Steinem [Hennesthal and Steinem, 2000] have shown that lipid structures can be formed on the surface of gold-coated alumina. This work used atomic force microscopy (AFM) to study the structure of the membrane, but did not study the formation mechanism or characterize additional membrane properties of the lipid bilayer membrane on a porous gold surface. Weng et al., [Weng et al., 2004a; Weng et al., 2004b] have worked to understand the formation process and membrane diffusion behavior on silica xerogels (a porous silica surface); their group demonstrated how porosity affects the behavior of membranes on silica surfaces (an increase in the formation time required to synthesize a continuous membrane while decreasing the transport behavior due to the surface contours). Nellis et al. [2007] studied the transport behavior of several porous oxide and organic xerogels via fluorescence studies (FRAP); however, the study does not detail the formation process of lipid bilayer membranes on the various support materials which is important towards the overall understanding of inorganically supported lipid bilayer membranes. Widespread application of supported lipid bilayer membrane technology would require a more in-depth study of porous supported lipid bilayer membranes on surfaces with a range porosities and chemistries.

1.5.3. Support geometry

The geometry of a support material may also affect the bilayer membrane behavior. The majority of the supports have a planar geometry, their size on the order of 5-10 cm^2 [Johnson et al., 2002; Richter et al., 2003; Knoll, 1998; Hennesthal & Steinem, 2000; Lu & Ottova, 1996; Uto et al., 1994; Sackmann & Tanaka, 2000; Tanaka & Sackmann, 2005; Richter et al., 2006] and are so chosen based on desired applications. Planar supported membranes are often selected due to their ease in synthesis and characterization. The vast majority of studies characterizing lipid bilayer membranes have been planar supported membranes.

In a few cases, silica spherical supports (beads) have also been utilized as supporting materials for lipid bilayer membrane deposition [Baksh et al., 2004; Bayerl & Bloom, 1990; Linseisen et al., 1997; Scott & Jones, 2002; Buranda et al., 2003]. These studies verified membrane lateral fluidity [Baksh et al., 2004] and stability [Bayerl & Bloom, 1990], thus verifying membrane biomimetic membrane deposition feasibility. Due to the small surface area of the support, it was determined that the diffusivity was limited due to unmet underlying conditions (i.e. an insufficient fluorescent sink for fluorescent recovery).

1.6. General synthesis methods of supported lipid bilayer membranes

1.6.1. General synthesis methods

Reproducible synthesis of supported lipid bilayer membranes is typically performed using two general methods: successive monolayer deposition and vesicle fusion. Successive monolayer deposition is typically conducted using Langmuir-Blodgett technology. This technology creates organized two-dimensional monolayer structures of amphiphilic molecules on a solid supporting material; monolayers deposited in succession can yield a final lipid bilayer membrane structure [Girard-Egrot & Blum, 2007]. This technique allows for high reproducibility in membrane continuity and thickness and has the ability to synthesize a membrane over a large area. Additionally, this method promotes bilayer deposition on a wide range of support surfaces (assuming compatibility between lipid and surface chemistry) as well as synthesis of complicated multi-layer lipid structures [Girard-Egrot & Blum, 2007]. While this technique is useful for synthesizing a lipid bilayer structure, exposure to air during synthesis may result in peeling or may allow for sample contamination that would damage the membrane structure and integrity [Peterson, 1990].

The second technique used to synthesize supported lipid bilayer membranes is vesicle fusion, and is the most widely used technique for membrane synthesis [Valenzuela, 2007]. Vesicle deposition is a process in which vesicles spontaneously fuse and rupture on a support surface to form a lipid bilayer membrane. Vesicles are lipid bilayer structures in a spherical conformation encapsulating an aqueous solution within its center. Vesicles can be classified as multilamellar or unilamellar, with its lamellarity dependent on the number of lipid bilayers layers present in the vesicle shell, as shown in Figure 1-3. The vesicles used as precursors to the formation of a single lipid bilayer membrane are typically unilamellar vesicles due to the presence of a single bilayer in its shell.

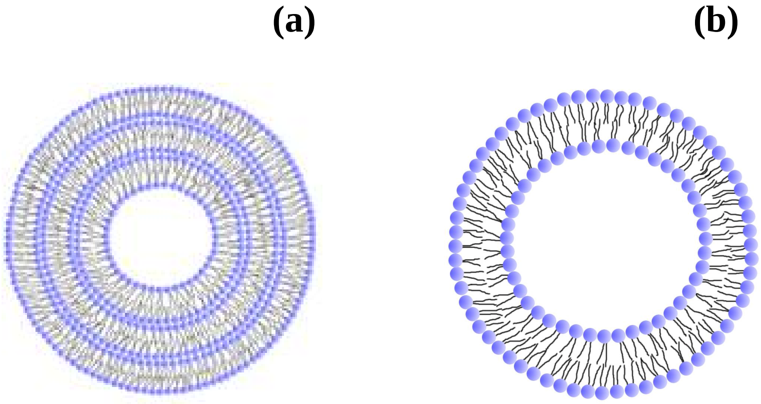

Figure 1-3. Schematics of (a) multilamellar vesicles and (b) unilamellar vesicles.

1.6.2. Unilamellar vesicle synthesis

There are several methods used to form unilamellar vesicles: extrusion, freeze thawing and ultrasonication [Martin, 2007]. All methods begin with multilamellar vesicles (Figure 1-3a) and processing techniques are used to reduce the lamellarity of the sample. Extrusion typically utilizes polycarbonate membranes (50-200 nm), using a pressure system to pass the multilamellar vesicles through the membrane. Multiple passes through the membrane (usually an odd number to prevent contamination) are conducted to synthesize a vesicle solution with a uniform diameter distribution near to the membrane pore diameter. Freeze thawing is a commonly used method used in conjunction with extrusion, and is comprised of an equal number of freeze steps and thaw steps. Together, these two steps will cause the vesicles to rupture and reform to minimize its free energy. Multiple phases of vesicle rupture and reformation will result in a unilamellar vesicle (Figure 1-3b).

The third method used for synthesis of unilamellar vesicles is ultrasonication, performed in a water bath or using a probe. This method delivers ultrasonic waves to the multilamellar vesicles causing them to break. Upon re-aggregation, the vesicles form a vesicle of a smaller diameter and often of less lamellarity. After sonication, samples prepared using a tip sonicator require centrifugation to remove remnant metal particles from the sonicator tip. Bath sonicated vesicle preparation procedures are often preferred as they eliminate tip contamination.

1.7. Lipid bilayer membrane formation

The formation of lipid bilayers on flat dense substrates by vesicle fusion has been extensively studied by Kasemo and coworkers [Keller & Kasemo, 1998; Keller et al., 2000; Zhdanov & Kasemo, 2001] and Boxer and coworkers [Johnson et al., 2002; Schonherr et al., 2004]. The lipid bilayer formation process progresses via vesicle adsorption and vesicle rupture to form a supported lipid bilayer. While fusion and rupture are two unique processes, they do not occur in a stepwise fashion, often occurring simultaneously and via several mechanisms to form a continuous lipid bilayer membrane (Figure 1-4, adapted from Richter et al., 2003).

Initially, vesicle adsorption occurs randomly across the surface (Figure 1-4a). As time progresses, vesicles continue to adsorb onto the surface and follow one of two behaviors: small vesicles (d_m<D_c, where d_m = vesicle diameter and D_c = critical vesicle diameter) adsorb on the surface and undergo vesicle-vesicle fusion to form large vesicles (D_c<d_m) (Figure 1-4b) or vesicles of sufficient size to rupture (D_c>d_m) directly adsorb onto the support surface and do not interact with other vesicles adsorbed on the surface (Figure 1-4c). The vesicles continue to populate the surface until the substrate reaches an appreciable vesicle concentration (an appreciable surface vesicle concentration is dependent on the bulk vesicle concentration [Zhdanov & Kasemo, 2001]), but typically ~15% of the total lipid mass required for a single lipid bilayer to form [Johnson et al., 2002]. At this critical vesicle coverage, the adsorbed vesicles rupture and form lipid bilayer islands across the support surface (Figure 1-4d/e). During the vesicle rupture process, vesicles are simultaneously adsorbing on the surface. The un-ruptured vesicles interact with the lipid bilayer islands causing the vesicles to rupture and increase the density of bilayer islands across the surface. This process continues until a continuous supported lipid bilayer membrane is formed (Figure 1-4f).

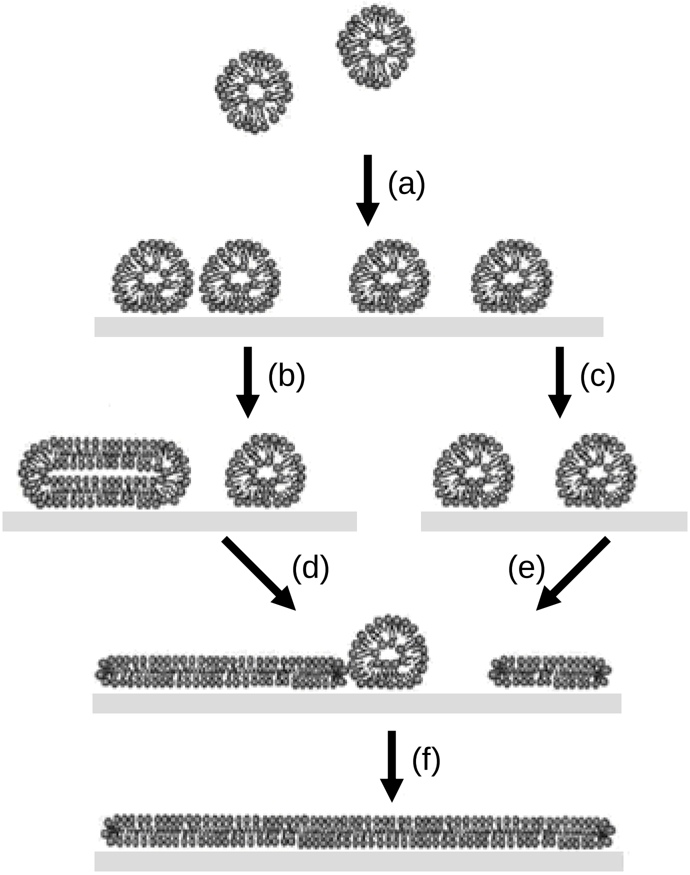

Figure 1-4. Vesicle deposition and rupture on SiO_2 surfaces (not drawn to scale).

The formation mechanism can be correlated to the data shown in Figure 1-5 [adapted from Keller & Kasemo, 1998], which is dynamic mass adsorption behavior measured by a quartz crystal microbalance. The experimental output is frequency, which decreases due to mass adsorption on the surface of the resonator; the frequency shift can be correlated to mass adsorption through the Sauerbrey equation. This equation states that a decrease in frequency correlates to an increase in mass. A typical formation curve on SiO_2 can be found in Figure 1-5 below.

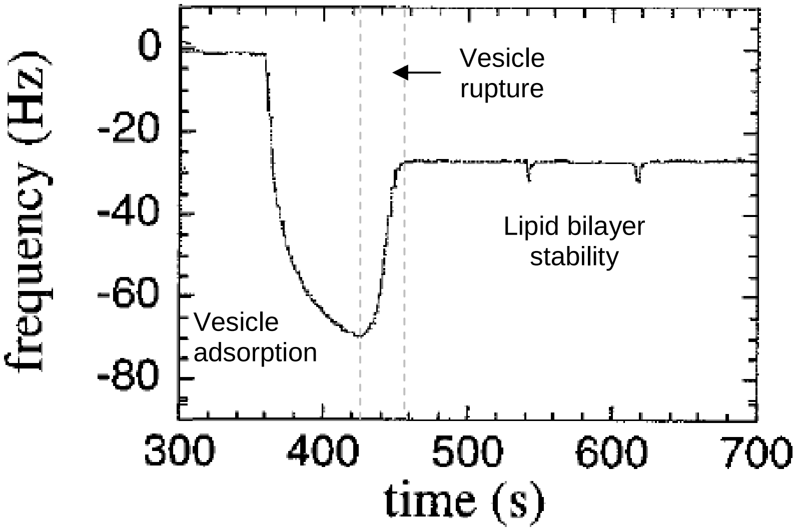

Figure 1.5. A typical lipid membrane formation process on SiO_2.

Figure 1-5 shows an initial frequency decrease, which can be correlated to vesicle adsorption (mass uptake) on the surface (Figures 1-4a/b). After a point, the df/dt reverses and a frequency increase is seen; this can be correlated to vesicle rupture and a mass decrease (Figure 1-4c/d); the mass decrease can be correlated to vesicle rupture and release of the encapsulated water in its center. The frequency continues to increase until it reaches steady state where a stable lipid bilayer is formed (Figure 1-4e). This behavior seen in Figure 1-5 is the typical behavior of the formation of a single lipid bilayer membrane on a SiO_2 surface.

While a wide range of materials have been examined as potential supports for supported lipid bilayer membrane technology, the formation mechanism described in Figure 1-4 and Figure 1-5 is only valid for SiO_2 and Si_3N_4 materials [Reimhult, 2003].

The chemistry of the support surface is a critical parameter for the formation of a single lipid bilayer membrane. Keller & Kasemo [Keller & Kasemo, 1998] monitored the vesicle adsorption behavior on three different surfaces to evaluate the vesicle adsorption behavior on each surface. Surfaces chosen were either hydrophobic (methyl-terminated thiols anchored on gold) or hydrophilic (SiO_2 and oxidized gold) surfaces. Keller & Kasemo found that the vesicle adsorption behavior showed an exponential frequency decrease with each gold-based system, while the SiO_2 experienced the typical lipid bilayer membrane formation behavior as described in Figure 1-4 and Figure 1-5. The final frequency shift on the methyl-terminated gold surface was half of the final frequency shift of SiO_2 indicating a lipid monolayer has been formed (half of the frequency shift indicates half of the adsorbed mass). This result is expected due to the hydrophobic interactions between the surface and the hydrophobic lipid tails which would yield a lipid monolayer on its surface. The formation behavior on oxidized gold yielded an exponential frequency decrease upon vesicle adsorption; this is indicative of irreversible vesicle adsorption yielding a stable vesicle monolayer on the surface. This has been shown on materials such as TiO_2 [Reimhult et al., 2002], platinum [Reimhult et al., 2003], chromium and ITO [Groves et al., 1998]. Published literatures has found that this type of behavior is characteristic of nearly all non-SiO_2 hydrophilic surfaces.

While considerable research has been conducted to understand the formation of supported lipid bilayer membranes, it is still unknown why vesicles adsorb with rupture on SiO_2 surfaces, while vesicles adsorb without rupture on virtually all other hydrophilic surfaces. It has been hypothesized that the difference in behavior may be attributed to surface polarizability or charge [Reimhult et al., 2002; Reimhult et al., 2003], however a systematic study examining this behavior is lacking.

A literature review has also found that lipid chemistry also significantly affects the formation of bilayer membranes. As shown in Figure 1-1, there is a wide range of polar head groups that can be used for lipid bilayer synthesis. To optimize lipid bilayer formation, there must be a charge difference between the support surface and the lipid molecules that would facilitate attraction and deposition of vesicles. Richter et al. [2006] investigated the effect of lipid charge (by varying lipid composition) on the binding and rupture of vesicles. The lipids chosen were DOPC (zwitterionic) and DOPS (negatively charged). Richter et al. found that vesicles composed predominately of lipids with a negative charge do not adsorb to a SiO_2 surface; this can be attributed to the charge match between the surface and the lipid molecule due to the negative charge on both surface and lipid. As the charge is balanced from a negative to a zwitterionic charge, the formation behavior shifted from zero adsorption (1:2, DOPC:DOPS) to vesicle adsorption without rupture (1:1, DOPC:DOPS) to lipid bilayer formation (4:1, DOPC:DOPS). Therefore, the lipid bilayer membrane and support system must be designed to consider the surface interaction, which will greatly influence the final structure of the film.

1.8. Lipid bilayer membrane characterization

Within the published literature, supported lipid bilayer membranes are characterized using several techniques. While there are a plethora of techniques that are used to study lipid bilayer membranes, three important techniques are frequently employed to characterize membrane properties, as summarized below.

1.8.1. Direct mass adsorption

Direct mass adsorption is frequently used to study lipid bilayer membrane formation kinetics using a quartz crystal microbalance (QCM). The quartz crystal is a piezoelectric material and when exposed to an AC voltage, the quartz resonates at a pre-determined frequency (typically 5 or 6 Hz, but occasionally 3 or 9 Hz crystals are also used). Using the Sauerbrey equation, the frequency shift can be correlated to mass adsorption and desorption of rigid films. The formation process of lipid membranes has been studied using direct mass accumulation techniques, to study the effect of lipids of differing chemistries (both singularly and as mixtures) [Richter et al., 2003] and of supports with differing surface chemistries [Keller & Kasemo, 1998].

1.8.2. Fluorescence microscopy

Fluorescence microscopy, and more specifically fluorescence recovery after photobleaching (FRAP), is a useful technique often used to verify membrane continuity and to measure biological membrane diffusion [Richter et al., 2006]. Typically, membrane lipids are not inherently fluorescent and require the covalent attachment of a fluorescent tag (typically fluorescent tags include NBD-PE or Texas Red) in a ratio of 1-3 mol% for microscopic measurement. FRAP analysis measures the diffusion and lateral mobility of a membrane by bleaching a select area of the membrane and monitoring the fluorescence recovery within the bleached region. A typical membrane diffusion coefficient on glass can range between 1-5 $\mu m^2/s$ [Baksh et al., 2004], but can vary based on the substrate, tag, membrane composition, and membrane preparation procedures used.

1.8.3. Atomic force microscopy

Atomic force microscopy (AFM) is a surface probing technique that is often used to evaluate a film surface. AFM employs a tip mounted on a cantilever, which is scanned along a sample surface; the deflections of the cantilever map the surface topography. AFM is also used to determine surface topography of the membrane and is useful for evaluating surface continuity and studying the effect of membrane defects [Reviakine & Brisson, 2000; Johnson et al., 2002; Schonherr et al., 2004]. AFM has often been employed to monitor stages of the vesicle deposition process in an effort to better understand the formation process of bilayer membranes [Jass et al., 2000; Seantier et al., 2004]. Additionally, AFM has been used to characterize the continuity of a supported lipid bilayer structures on gold-coated anopore membranes [Hennesthal & Steinem, 2000].

1.9. Supported lipid bilayer membrane applications

Supported lipid bilayer membranes are excellent candidates for biosensing applications. Lipid bilayers create a biocompatible film on nearly any transducer surface and allow for a wide range of adsorption capabilities; these unique properties create a nearly universal biosensor [Martin, 2007]. Additionally, the natural environment provided by the lipid bilayer allows a binding analyte to retain many naturally occurring properties to provide optimal sensing results [Martin, 2007].

Lipid membrane technology has been applied to a wide variety of applications. Fundamentally, lipid membranes have been utilized as model membranes for a range of in vivo membranes, such as plasma, mitrochondrial, nerve, light sensitive, and visual receptor membranes [Tien & Ottova, 2001 and references therein]. Researchers have made significant strides in the understanding of the membrane types above through the isolation of critical receptors or protein channeling kinetics which have led to breakthroughs in understanding their individual roles in cell functionality.

1.10. Project objectives and dissertation organization

1.10.1. Project objectives

Published literature has shown that there are a significant number of supporting materials examined as potential supports for supported lipid bilayer membrane technology. Dense supports with a wide range of surface properties have been investigated to understand their interaction with biological membranes. Minimal work has been conducted to understand the bilayer membrane properties on porous supports, which would simultaneously improve stability while providing unsupported regions for transmembrane flow studies. Additionally, the vast majority of the work in this field has focused on planar supports with only a small number of studies on spherical supports. Expansion of the supports to a cylindrical geometry would expand the available applications to optical fiber biosensing.

This dissertation will investigate novel supports for supported lipid bilayer membrane technology. There are two fundamental areas that will be studied: (1) improvement in the available porous materials for use in supported bilayer membrane technology and (2) expansion of the available support materials to cylindrical geometries for potential applications in biosensing.

Objective 1

In order to investigate vesicle adsorption behavior on porous supports, four types of porous materials were chosen for study: zeolite (silicalite), γ-alumina, mesoporous zirconia (yttria stabilized, YSZ) and macroporous YSZ. The vesicle adsorption process will be monitored using a quartz crystal microbalance under a variety of conditions in an effort to understand their effect on formation. Surface chemistry will be investigated using dense silica and γ-alumina. Buffer pH will be investigated using mesoporous YSZ and γ-alumina. Surface roughness will be compared using materials of comparable surface chemistry: dense silica and zeolite (SiO_2 materials), mesoporous and macroporous YSZ (zirconia materials).

Objective 2

In order to investigate lipid bilayer membrane behavior on cylindrical supports, silica optical fibers (125 μm diameter) were chosen as supporting materials. Kinetic formation behavior will be measured using a novel optical technique, long period fiber grating refractometry (LPFGs). A novel sensing scheme composed of two LPFGs in series will be used to counter environmental conditions that may affect the sensitive data collection during the formation of a lipid bilayer. Gramicidin containing bilayer membranes will be investigated to understand their effect on the formation of these membranes. Because the behavior of lipid bilayer membranes greatly affects the performance of optical biosensors, the diffusion characteristics of cylindrically supported lipid bilayer membranes will be investigated. Experimental artifacts will be explored in order to yield the true diffusion behavior. Finally, theoretical modeling will be applied to confirm the unique observed experimental behavior.

The research objectives listed above provide a significant contribution to supported lipid bilayer membranes. The fundamental study of lipid bilayer membrane formation on porous substrates and cylindrical substrates will help the membrane community understand the capabilities of these membranes supported on novel materials. This study will also provide insight on the factors influencing membrane formation behavior, such as surface effects, solution effects, and characterization effects. Finally, the expansion of the available support materials will enhance application potential to future biosensing technologies.

1.10.2. Structure of the dissertation

This dissertation is divided into two parts, each one accomplishing the aforementioned objectives. Chapter 2 will address objective 1 and will show the effect of porous materials on the formation process of lipid membranes. Chapters 3 & 4 will address objective 2. Chapter 3 will detail the formation process of a lipid bilayer membrane on a dense cylindrical fiber using a novel sensing technique, long period fiber grating refractometry. Chapter 4 will address the dynamic transport behavior of membranes on cylindrical supports and will address system artifacts associated with characterization using experimental and theoretical techniques. Chapter 5 summarizes the work reported in this dissertation and discusses future directions for the development of novel biosensing technology.

Chapter 2

FORMATION OF LIPID BILAYER MEMBRANES AND MONOLAYER VESICLE ADSORPTION ON POROUS INORGANIC THIN FILMS

2.1. Introduction

As discussed in Chapter 1, the majority of the work studying lipid bilayer membranes employs dense supporting materials due to their wide availability and ease of supported membrane characterization. While dense supports offer many advantages to studying membrane behavior, the support material can inhibit natural membrane properties. Additionally, the dense properties of the film also limit accessibility of each side of the lipid bilayer membrane thus eliminating the ability for investigating transmembrane chemical gradients [Hennesthal & Steinem, 2000; Reimhult & Kumar, 2011]. These limitations significantly affect the future application of lipid bilayer membrane technology.

Porous materials offer several advantages to the field of supported lipid bilayer membranes. The dense character of a supporting material adds stability to the membrane while the porous character of the film simultaneously adds regions of accessibility for transmembrane ion channeling studies [Reimhult & Kumar, 2011].

Within the published literature, work has been done to study the properties of pore-spanning lipid bilayer membranes on nano-sized apertures and porous supports. Simon et al. [Simon et al., 2007] synthesized pore-spanning lipid bilayer membranes on silicon materials with apertures of 300 nm, 650 nm and 1000 nm. Similarly, Han et al. [Han et al., 2007] studied pore-spanning membranes on apertures of 200 nm and 800 nm. In both studies, results determined that the stability of free-spanning membranes was increased with decreased aperture diameter. Steinem and coworkers [Hennesthal & Steinem, 2000] reported the formation of a lipid bilayer membrane on an anodically etched aluminum foil (50 nm pore diameter) modified with a 10 nm surface gold layer; the membrane continuity was measured using AFM, however membrane quality was not examined using fluorescence, acoustic or electrical techniques. Steinem and coworkers [Schmitt et al., 2007] also examined pore spanning lipid bilayer membranes on anodic alumina (60 nm pore diameter) anchored with a cholesterol derivative. This work found that quality single lipid bilayer membranes were formed with a stability exceeding 200 hours, as measured by impedance spectroscopy.

Weng et al. [Weng et al., 2004] reported the formation of eggPC lipid bilayer membranes on porous silica xerogels, finding that the increased surface area and pore distribution decreased membrane diffusivity by 75% and increased membrane formation time requirements by 30 times. Nellis et al. [2011] has studied the diffusion behavior of metal oxide and organic oxide supported lipid bilayer membranes. Using FRAP, the authors found that the structures formed on the supports recovered after bleach indicating that a lipid bilayer membrane was formed. While valuable, the formation mechanism of lipid membranes was not measured on their surfaces therefore limiting their future application potential.

While all of these studies show promising results demonstrating the concept of membrane deposition on porous supports, a systematic study of the lipid bilayer membrane formation on porous thin films of various surface chemistries and porosities is lacking.

Inorganic porous thin films are unique films with countless applications due to their ability to be engineered to possess specific material properties (i.e., surface chemistry or porosity). Inorganic porous membranes and thin films have recently gained attention for applications specifically for biological technology. For example, zeolite films and structures have recently been used as media for drug delivery and also as anti-corrosive coatings for biomedical implants due to small pore size and chemical stability [Pina et al., 2011]. Due to their current applications in biotechnology, a study investigating the formation of planar lipid bilayer membranes on a range of porous inorganic materials would benefit the application of pore-spanning lipid bilayer membranes to biotechnology.

Dense inorganic materials have been extensively used in the medical industry due to their biocompatibility and long-term stability [Hulbert, 1993]. Alumina and zirconia materials have been widely used in medical implants due to their mechanical hardness and inert chemical structure [Hulbert, 1993]. Bioglasses have been used for implant coatings to protect the substrate from corrosion and to prevent interfacial attachment to the bones [Hench & Wilson, 1993]. Because of their wide use in biomedical applications, it is a natural extension to apply these materials to biotechnology, and specifically to supported lipid bilayer membrane technology. Because of the biocompatibility of alumina and zirconia materials, these materials are ideal candidates for the novel application of porous supported lipid bilayer membranes.

This chapter will address the current limitations of pore-spanning lipid bilayer membrane technology through a systematic study investigating the formation of biological membranes on four types of porous inorganic supports: zeolite (silicalite), γ-alumina, mesoporous zirconia (yttria stabilized - YSZ) and macroporous YSZ. These specific materials were chosen due to their unique surface chemistries and porosities, characteristics which have been demonstrated to significantly affect the formation of lipid bilayer membranes. The formation process of lipid bilayer membranes via the vesicle deposition method under various conditions have been examined using direct mass adsorption measured using a quartz crustal microbalance.

2.2. Materials and Methods

2.2.1. Vesicle Synthesis and Characterization

Supported lipid bilayers were prepared via the vesicle deposition process pioneered by Tamm & Mcconnell [1985] and briefly described here. The chloroform solvent was gently removed from the eggPC molecules (L-α-phosphatidylcholine, 99%, Avanti Polar Lipids) by an inert gas stream for 30 minutes to form a lipid film on the bottom of a glass test tube. The test tube was subjected to overnight high vacuum conditions at ambient temperatures (Precision vacuum oven, Model 19, Thermo Electric Corporation) to remove residual chloroform solvent. After vacuum, the lipid film was rehydrated with a buffer solution (100 mM NaCl, 10 mM Tris, pH = 8 or 4) for 1-2 hours (NaCl - Mallinckrodt Chemicals; Tris - MP Biomedicals, LLC; H_2O - Millipore Academic filtration system (18.2 MΩ)). The hydrated lipids are vortexed (Fischer Scientific Touch Mixer, Model 232) for 10 minutes to re-suspend the lipids into solution. The lipid suspension was sonicated for 30 minutes under high power bath sonication (Laboratory Supplies Inc) to yield unilamellar vesicles (ULVs). A lipid concentration of 0.1 mg/mL was used for all experiments. Vesicle diameter was characterized using dynamic light scattering (DLS, 90 Plus, Brookhaven Instrument Corp.) DLS verified that the vesicle diameter was 180 ± 10 nm for vesicles prepared in buffer of either pH = 8 or pH = 4.

2.2.2. Thin film preparation

All thin films were prepared on 1-inch 5MHz polished crystals (AT cut, Cr/Au electrode). Prior to thin film deposition, a dual layer consisting of chromium and SiO_2 (outer layer) was deposited on the QCM crystal to promote inorganic porous thin film adhesion (RF sputtering, cryopumped Kurt J. Lesker Supersystem II). Sols or suspensions for each film type were synthesized as stated below. Each sol was added to a crystal drop wise and spin-coated at 2000 RPM. All crystals were dried in a humidity chamber at 35°C and relative humidity of 40% for 2 days and calcined at 400°C for either 12 hours (zeolite) or

6 hours (γ-alumina or zirconia). Multiple coats were applied to achieve a continuous film of a desired thickness.

MFI type zeolite suspension solutions were synthesized with a molar composition of 10 SiO_2: 2.4 TPAOH: 1 NaOH: 110 H_2O and was hydrothermally treated at 125 ^oC for 8 hours. The spincoat solution was prepared by adding 0.5 wt% hydroxyl propyl cellulose (HPC) (MW 100,000 $g.mol^{-1}$, Aldrich) and balance Millipore water (18.2 MΩ) and titrating the spincoat solution to pH 3-4 using 1M HNO_3.

Stable boehmite sol was synthesized by hydrolyzing aluminum tri-sec-butoxide in water at 90^oC under refluxing conditions. Hydrolysis and condensation of the aluminum tri-sec-butoxide yielded boehmite precipitate. The boehmite precipitate was peptized using nitric acid and further refluxed and boiled to remove the excess alcohol. Prior to spin coating, the sol was mixed with a 3 wt% poly(vinyl) alcohol (PVA, Fluka, MW = 72000) solution to improve particulate binding after coating and prevent film cracking.

Zirconia sol was synthesized by first mixing zirconium (IV) n-propoxide (Alfa-Aesar) in alcohol at ambient conditions. The zirconium n-propoxide/isopropanol mixture was added to water dropwise at 70 ^oC. The precipitate was filtered and washed several times to remove excess alcohol in the system. The precipitate was peptized in nitric acid overnight and diluted in water to yield the final sol. Prior to spincoating, the sol was mixed with a 0.07M yttrium (III) nitrate hexahydrate (Sigma-Aldrich) and a 3 wt% PVA solution to improve particulate binding after coating and to prevent film cracking.

Yttria-stabilized zirconia suspension was made by mixing yttria-stabilized zirconia powder (8 mol%, Tosoh) with nitric acid (1:2 mass ratio). The suspension was ball-milled for one week. After ball milling, the solvent ratio was adjusted to yield a 10 wt% suspension. The suspension was mixed with a 3 wt% PVA solution to improve particulate binding after coating and to prevent film cracking.

2.2.3. Thin film characterization

Inorganic thin films were characterized using x-ray diffraction (XRD, Bruker, CuK_{α}) for crystalline structure; scanning electron microscopy (SEM, Philips XL-30) for surface continuity; atomic force microscopy (AFM, Bruker Dimension 3000) for surface roughness; infrared spectroscopy (FTIR, Smart Orbit, Nicolet 6700); nitrogen porosimetry (Micromeritics ASAP2020) for porosity. Nitrogen adsorption/desorption isotherms were collected under vacuum at 77 K under microporous mode under a minimum $P/P_o = 0.14$ after degassing at 200 ^oC for at least 16 hours. There were three types of samples prepared for film characterization: powders, wafer supported films and QCM supported films. The powders were synthesized by pouring the sol or suspension as prepared above (with the addition of binding agent and water, if applicable) into a Petri dish and drying at 35 ^oC and 40% relative humidity to achieve an unsupported film. This film was calcined at 400^oC for either 12 hours (zeolite) or 6 hours (γ-alumina or zirconia) and was ground using a mortar and pestle. This powder was used for XRD, FTIR, and nitrogen porosimetry measurements. Silicon wafers were used as alternatives for the QCM crystals as they have identical surface chemistry (wafers have a 1 nm layer of SiO_2 on the surface occurring during air exposure). Wafer-supported and QCM-supported films were prepared as detailed above. Wafer supported films were used for SEM analysis, and the QCM films (same films used for kinetic studies) were used for AFM analysis. Contact angle measurements were collected using a gonimeter (Kruss EasyDrop Contact Angle Meter) (standard error of ± 5%).

2.2.4. Quartz Crystal Microbalance Experiments

The instrument used for measuring direct mass adsorption was a Maxtek Research Quartz Crystal Microbalance (QCM). Figure 2-1 shows a schematic of the QCM flow chamber used for experiments. The QCM crystals were loaded into the flow chamber and allowed to reach equilibrium overnight. Throughout all experiments, the temperature was 20 ^{o}C. The crystals maintained a stable frequency response, maintaining a <1 Hz/hr drift. Prior to the experimentation, the crystals were exposed to water for at least 3 hours to ensure that the film was completely hydrated. Tris buffer was flowed across the QCM crystal at 50 μL/min for at least 1 hour prior to measurement to ensure crystal stability. The lipid solution was flowed across the crystal surface (flow rate = 50 μL/min) at time = 0 min and the lipid bilayer formation process was recorded for each thin film type. The standard error for QCM experiments is ± 5%.

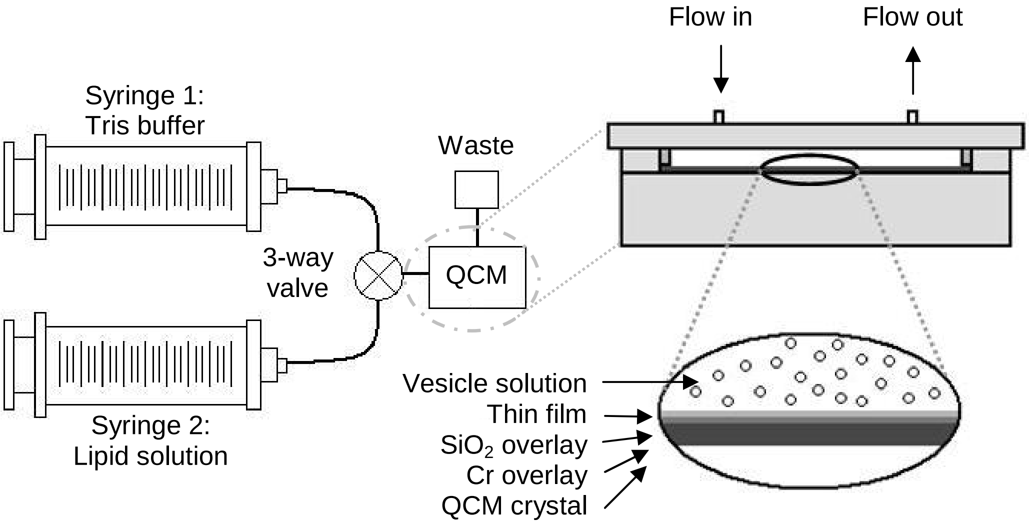

Figure 2-1. Schematic of the QCM measurement cell.

2.3. Results and Discussion

2.3.1. Porous inorganic thin film characterization

Figure 2-2 gives SEM images showing the surface morphology for each inorganic thin film. The surface morphology of the samples measured by AFM is given in Figure 2-3. Figure 2-2 shows that the surface of each film was found to be continuous, but each film had different topographical features. The zeolite and γ-alumina films appear to be relatively smooth, while the zirconia films each appear to be rough. AFM measurements confirm these results; with the RMS surface roughness of each as-synthesized thin film is summarized in Table 2-1. AFM measurements revealed that the γ-alumina surface was the smoothest surface, with a roughness of 4 nm. The zeolite and macroporous YSZ film had a similar surface roughness of 21 nm and 25 nm, respectively, but maintained distinctly different topographical features. The surface roughness of the mesoporous YSZ film was 41 nm, the roughest of all surfaced tested.

Table 2-1. *Material properties of the inorganic thin films*

Material	Surface roughness	Water Contact Angle (deg)	Pore Size (nm)	Pore Volume (cm^3/g)	Surface Area (m^2/g)
SiO_2	6 ± 0.2 nm	0	-	-	-
γ-alumina	4 ± 0.8 nm	10	3.0	0.33	432.4
Zeolite	21 ± 0.5 nm	21	0.5	0.13	224.9
YSZ (macroporous)	25 ± 3.5 nm	38	32.0	0.11	14.0
YSZ (mesoporous)	41 ± 1.2 nm	35	5.8	0.04	27.8

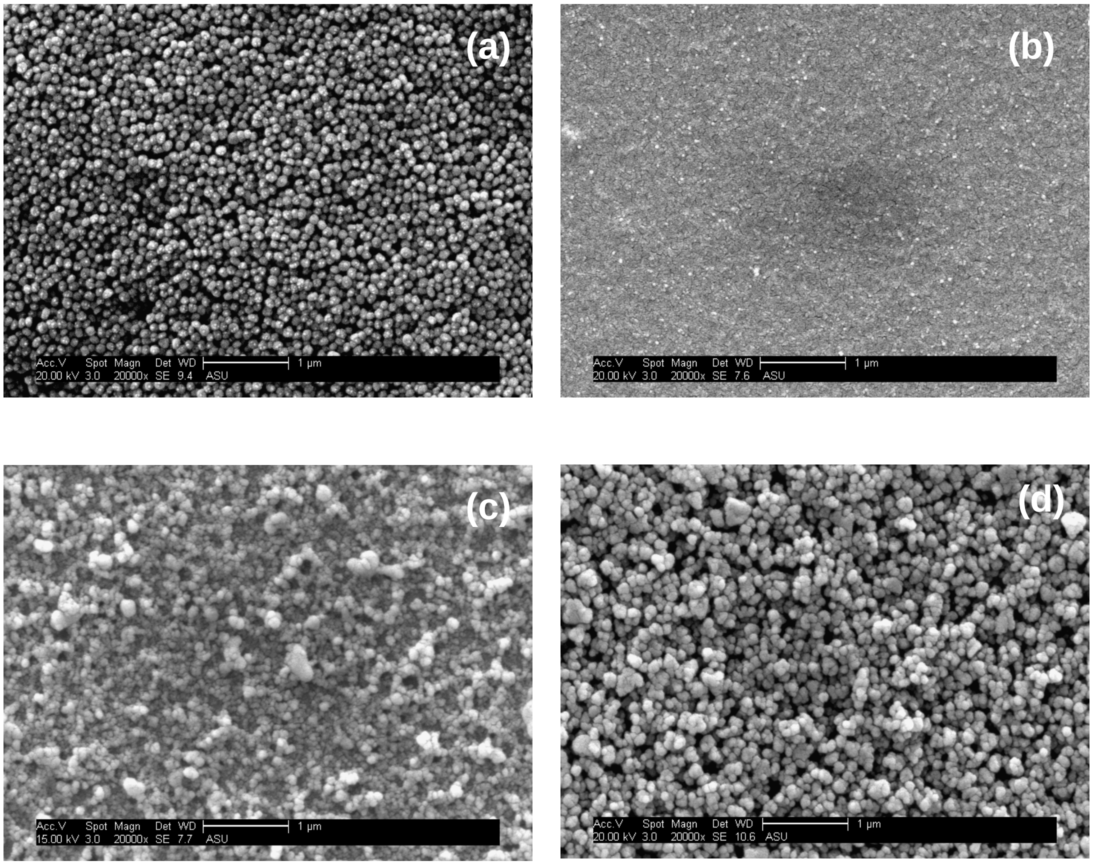

Figure 2-2. Surface micrograph images of (a) zeolite thin film, (b) γ-alumina thin film, (c) mesoporous YSZ thin film, (d) macroporous YSZ thin film (scale bar: 1 μm).

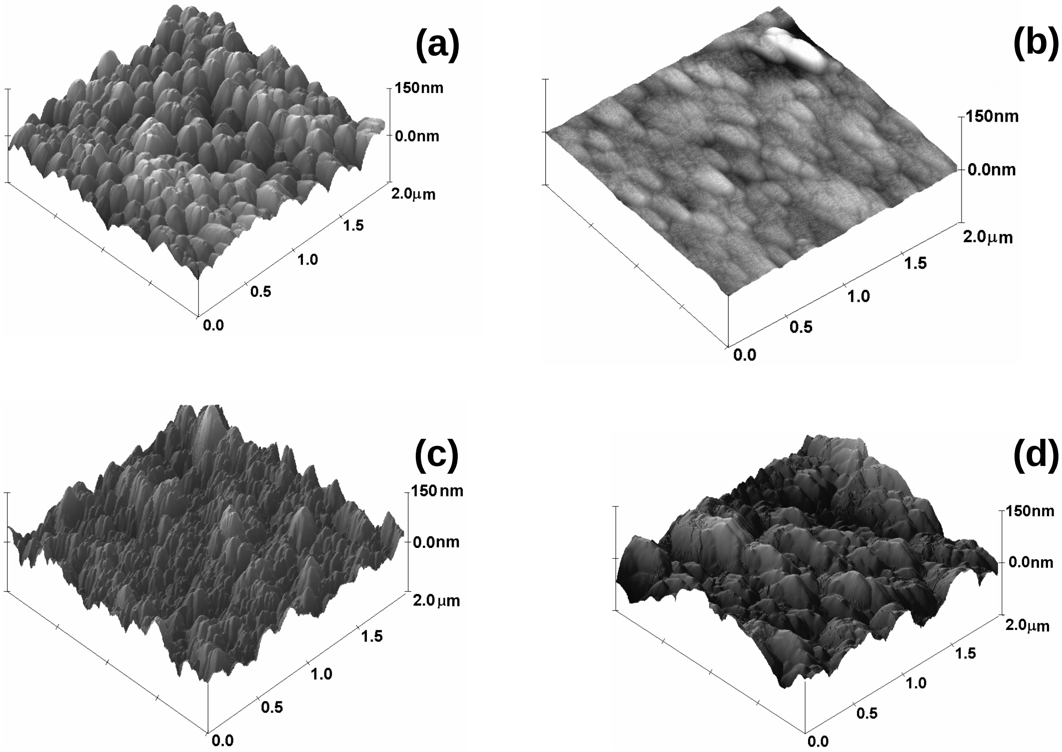

Figure 2-3. Surface morphology images evaluated by AFM – (a) zeolite, (b) γ-alumina, (c) mesoporous YSZ film, (d) macroporous YSZ film.

The zeolite film (Figure 2-2a, Figure 2-3a) is synthesized by depositing a seed layer of zeolite particles on the surface of the QCM crystal. Each seed is spherical and smooth with a 100 nm diameter (consistent to previous work by Lovallo et al. [Lovallo & Tsapatsis, 1996]). The surface roughness of the zeolite film is induced by the packing of the zeolite seeds with minimal surface roughness contribution from the individual seed surfaces. The relatively smoothness of the γ-alumina film (Figure 2-2b and Figure 2-3b) is attributed to the small particle size (roughly 10 nm).

The surface roughness differences between the mesoporous and macroporous YSZ films are attributed to different precursor preparation procedures. Mesoporous YSZ films are prepared using the sol gel method, where hydrolysis and condensation are used to synthesize stable particles in solution. After peptization, the size distribution of particles is relatively narrow because of charge stabilization on a particle surface which prevents aggregation; this particle stability is an integral property of a stable sol. The sol may have destabilized upon mixing with yttria nitrate and PVA, causing rapid aggregation of particles in solution. This process may produce a wide distribution of particle size and shape. This is confirmed through the topography of mesoporous YSZ measured by SEM (Figure 2-2c) and AFM (Figure 2-3c). In contrast, the macroporous YSZ films are synthesized by the deposition of ball milled particles with a final diameter distribution in the range of 100-200 nm in suspension. Therefore, because the particles have a relatively tight size distribution, particle packing does not induce sharp grain boundaries thus forming a YSZ surface with a smoother topography (see Figure 2-2d, 2-3d).

The porosity of each inorganic thin film was characterized using nitrogen porosimetry, with the adsorption/desorption isotherms presented in Figures 4a-4d. Pore size distributions for γ-alumina and YSZ materials are inset in Figures 4b-d and were extracted from the desorption branch using the BJH method (Figure 2-4b-d insets). Porosity properties are summarized in Table 2-1.

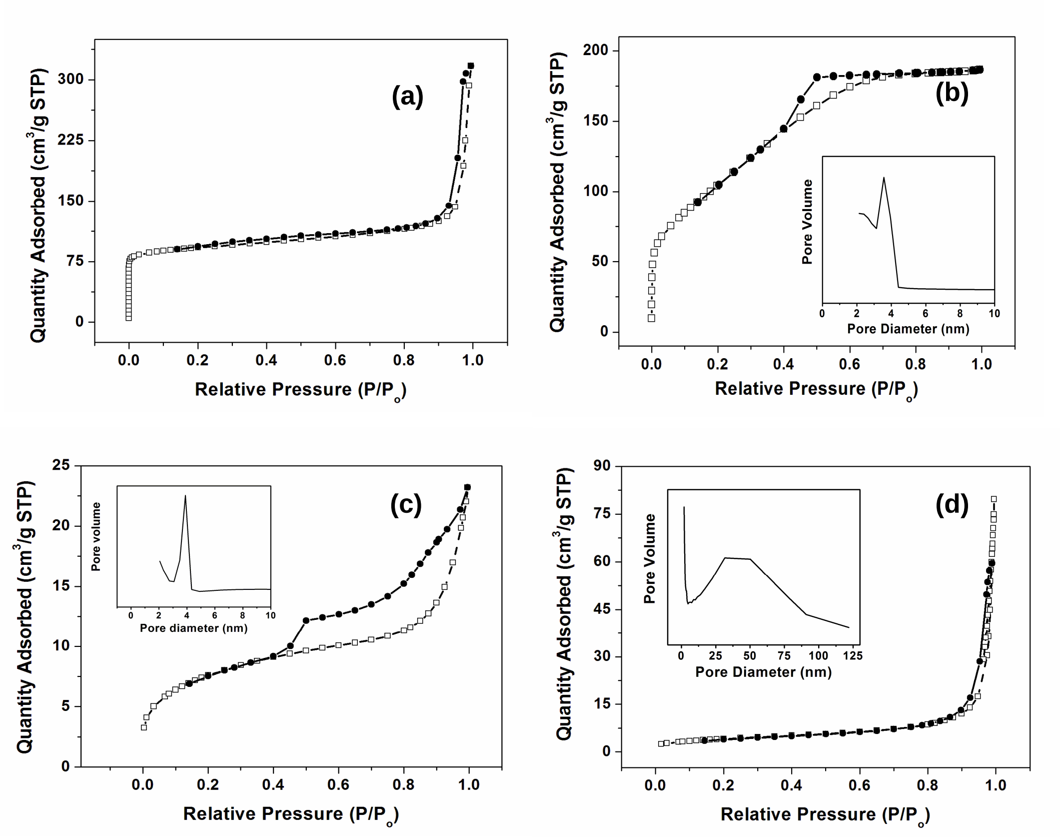

Figure 2-4. Nitrogen porosimetry adsorption/desorption curves of unsupported thin films of (a) zeolite, (b) γ-alumina, (c) mesoporous YSZ, (d) macroporous YSZ (open circles – adsorption, closed circles – desorption).

The zeolite pore diameter of 0.5 nm was calculated using the HK method; this result is consistent with previous work [Cooper & Lin, 2007]. The quantity of adsorbed nitrogen in the present study was significantly larger (300 cm^3/g) than what was found in Cooper et al. (170 cm^3/g) [37]. Additionally, the measured surface area values between studies were 224.9 m^2/g and 359 m^2/g (present vs. [Cooper & Lin, 2007]). This can be attributed to differing calcination temperatures. Within this work, all inorganic films were calcined at 400 ^{o}C to preserve the QCM crystal integrity; Cooper et al. [Cooper & Lin, 2007] calcined their samples to 650 ^{o}C. Cooper et al. [Cooper & Lin, 2007] found that an increased calcination temperature created densification of the zeolite seed layer; this causes a decrease in the mesoporous surface area while increasing the microporous surface area. This is observed in this work, as shown through surface imaging (Figures 2a and 3a) and pore size analysis (Figure 2-4a). A substantial mesoporous surface area can be seen due to the packing of the zeolite seeds. The depressed calcination temperature caused a greater instance of mesopores; this would increase the available surface area as well as the nitrogen adsorption capacity, which are both seen in this work.

Sharp peak distributions were found with γ-alumina and mesoporous YSZ materials indicating uniform mesopore diameter. Chang et al. [Chang et al., 1994] determined that a mesoporous zirconia film had a pore diameter of 3.8 nm, a pore volume of 0.11 cm^3/g, and a surface area of 57.2 m^2/g. Although sol preparation procedures between studies were identical, the calcination temperature used in Chang et al. was 450 ^{o}C whereas the calcination temperature in the present study was 400 ^{o}C. Chang et al. [Chang et al., 1994] determined that the pore size and pore volume for γ-alumina was 2.8 nm and 0.33 cm^3/g, which are in excellent agreement with the present work. However, the surface area in [Chang et al., 1994] was found to be 373 m^2/g, compared to 432.4 m^2/g in this study; this also can be explained by the difference in calcination temperatures.

A wide peak distribution was found with the macroporous YSZ film, indicating that a broad range of pore diameters were found within the unsupported film. Mercury porosimetry was used to measure the pore size distribution of identically prepared YSZ suspension; Kim et al. [Kim & Lin, 1999] determined that the pore size distribution centered around 100 nm, which is in agreement with this work.

The pore diameters of each inorganic thin film are less than 100 nm, which is considerably smaller than the 180 nm vesicle diameter used in this work. Because the pore size is comparatively smaller than a vesicle, it is likely that vesicles will not enter the support nor will the porosity have a large effect on the adsorption and rupture of vesicles on the surface of the porous inorganic thin films. While there is little expected porosity effect on adsorption on the macroscale, the porosity will contribute to the overall film roughness on the nanoscale and should be considered as a contributing (albeit small) factor to the film roughness. The porosity will be a significant factor when applying these films to transmembrane gradient studies where porosity is vital to their functionality.

Figures 2-5 and 2-6 show the XRD and FTIR spectra for each material type in an effort to characterize film crystallinity and bond structure. Figure 2-5a shows an XRD spectrum with long-range crystallinity consistent with randomly oriented zeolite [O'Brien-Abraham et al., 2007]. The XRD spectrum for γ-alumina (Figure 2-5b) shows major peaks at 45^o and 67^o, which was consistent with similarly prepared γ-alumina [Macedo et al., 2004]. Figures 5c and 5d show spectra for mesoporous and macroporous YSZ materials, respectively. The peak positions were identical between current samples and similarly prepared samples [Kim & Lin, 1998; Kim & Lin, 1999], indicating that all samples have the same material structure.

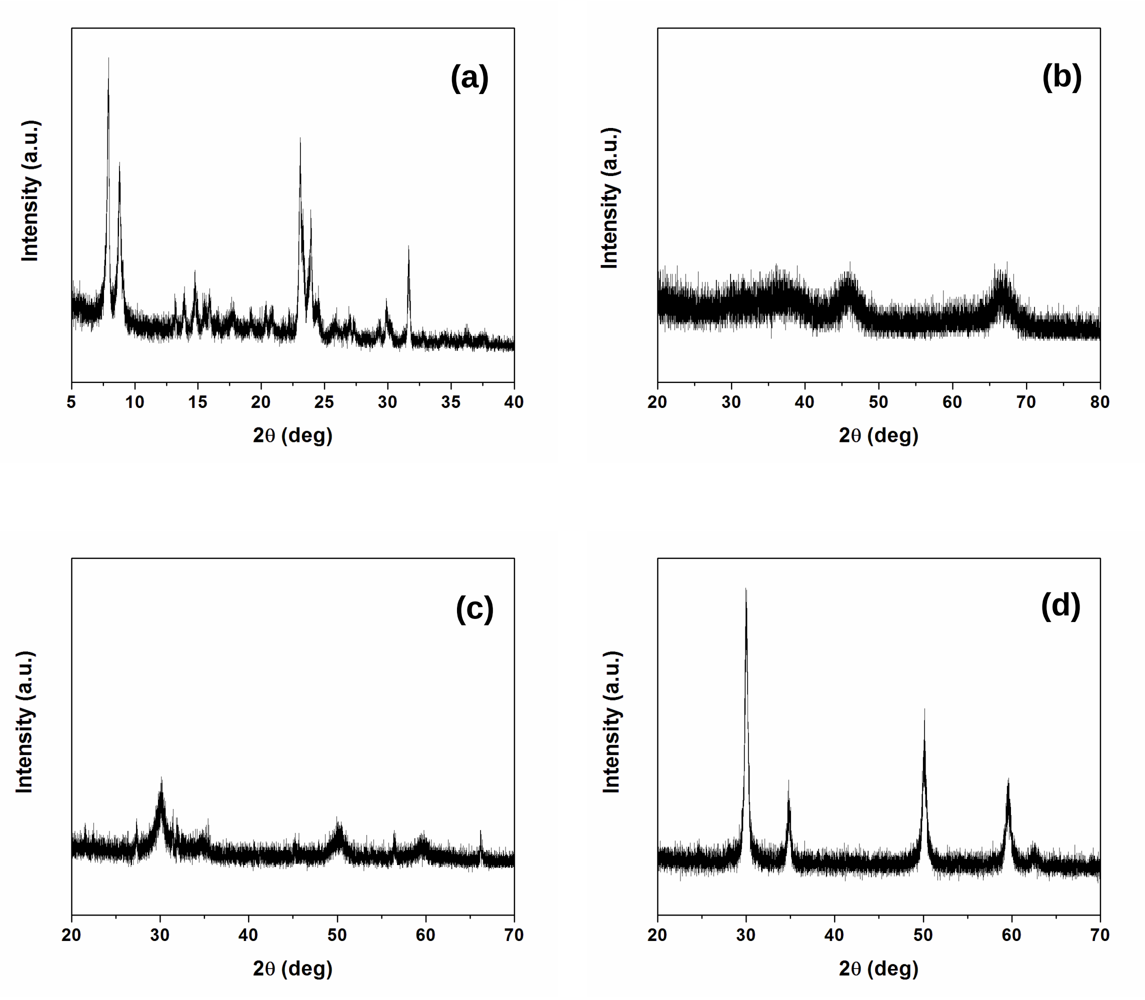

Figure 2-5. XRD patterns to verify crystallinity for (a) zeolite powder, (b) γ-alumina powder, (c) mesoporous YSZ powder, and (d) macroporous YSZ powder.

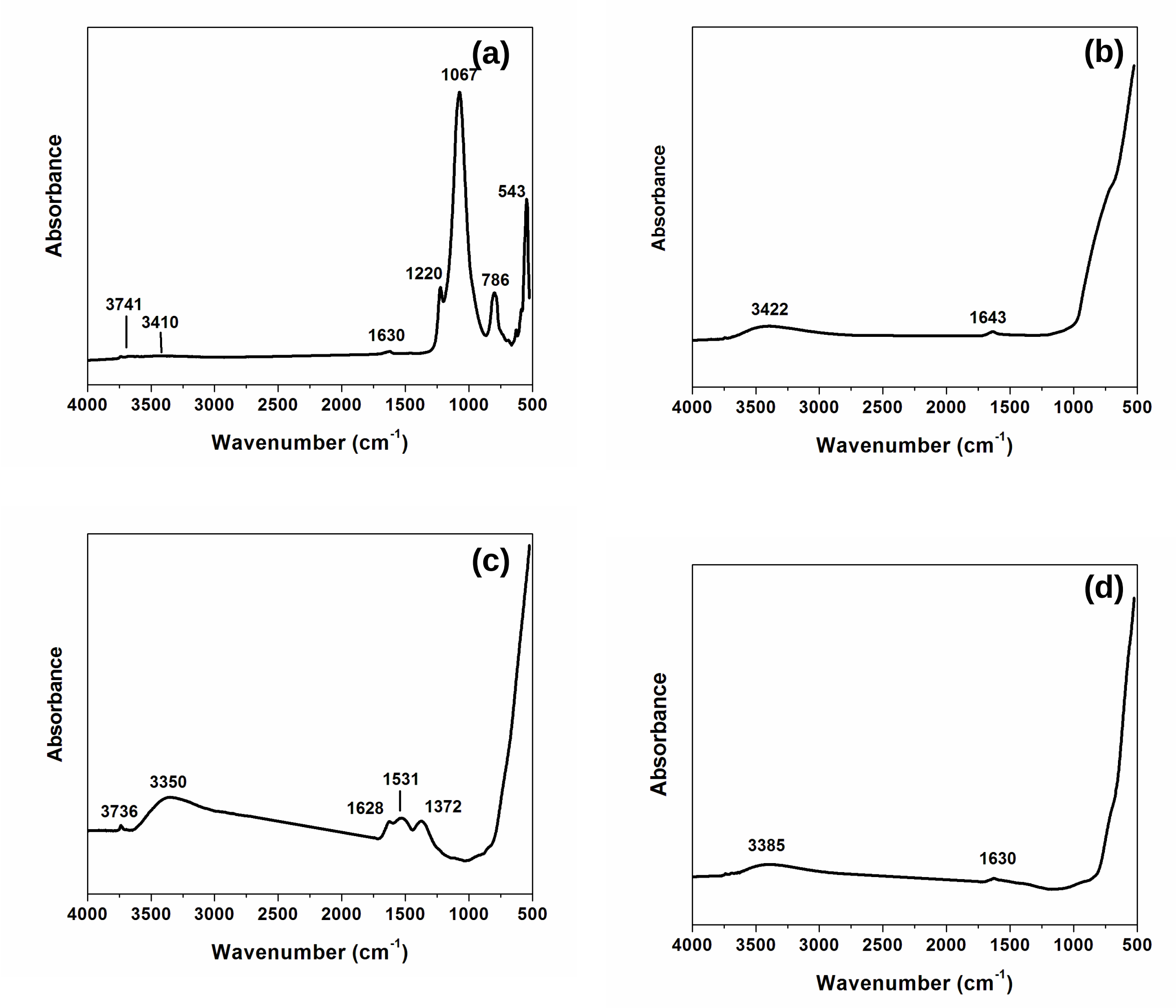

Figure 2-6. FTIR curves for (a) zeolite powder, (b) γ-alumina powder, (c) mesoporous YSZ powder, (d) macroporous YSZ powder.

The FTIR spectra for each film type can be found in Figure 2-6. The majority of the zeolite spectra (Figure 2-6a) consisted of peaks within 500-1500 cm^{-1}, indicating a Si-O-Si bonding [Tang et al., 2009]. While the peaks in the 500-1500 cm^{-1} range predominate, a small peak at 3700 cm^{-1} was observed signaling the presence of Si-OH bonds. The internal structure of zeolite is a continuous matrix of Si-O-Si bonds, which explains the accepted view that a silicalite zeolite is a hydrophobic material ([Funke et al., 1996], for example). However, at the zeolite surface, the Si-O-Si matrix is fractured leaving unstable Si-O complexes which quickly bond with hydrogen to form a stable Si-OH complexes. These Si-OH hydroxyl groups give the surface its hydrophilic character which promotes lipid bilayer membrane formation. Water was adsorbed onto all materials, as shown by the broad peak located in the 3280-3430 cm^{-1} and 1630-1640 cm^{-1} regions in Figures 2-6a-d [Zhao et al., 2006]. In Figure 2-6, regions between 500 and 1200 cm^{-1} are indicative of M-O bonds, where M is the metal of the film of interest (Al in γ-alumina [Busca et al., 1993], and likely Zr or Y in YSZ films) (Figure 2-6b-d). Additional peaks at 1531 cm^{-1} and 1372 cm^{-1} were found in the mesoporous YSZ material (Figure 2-5c), which are indicative of the formation of a bidentate complex [Dominguez Crespo et al., 2009].

Water contact angle measurements can be used to determine the surface hydrophilicity of a material, with decreasing contact angle correlating to increasing hydrophilic properties (hydrophilic materials are defined as materials with a contact angle $< 90^o$). All materials showed a water contact angle $< @^o$ indicating hydrophilic character (see Table 2-1). Together, FTIR and contact angle measurements indicate that each film is hydrophilic. It is important to note that the FTIR technique cannot be used to quantify the surface hydrophilic character of the material. The penetration depth of the IR beam into the sample can be up to 1 μm; therefore, the material properties measured with FTIR incorporate surface and internal structure properties. However, the FTIR technique indicates hydrophilicity which indicates that these materials are suitable for lipid bilayer membrane deposition.

2.3.2. Biomembrane formation: effect of surface chemistry

The lipid bilayer formation process via vesicle deposition is a delicate process that is highly influenced by the surface chemistry of the support. A wide range of surface chemistries have been studied in an effort to determine the factors governing vesicle rupture after vesicle adsorption on a support surface. A select few hydrophilic surfaces have been found to induce the formation of a lipid bilayer from vesicle rupture, including SiO_2, Si_3N_4, and mica [Egawa & Furusawa, 1999; Reimhult et al., 2003]. Additional hydrophilic surfaces, such as TiO_2 and gold coated anodic alumina [Hennesthal & Steinem; Reimhult et al., 2002], promote vesicle adsorption without vesicle rupture on each surface. SiO_2 was chosen in this work to give a baseline of the formation process occurring under current conditions. γ-alumina was chosen due to its similar surface chemistry (metal oxide) and similar surface topographies (see Table 2-1); it is ideal for study to evaluate the formation mechanism on a porous substrate of similar surface chemistry.

Figure 2-7 shows the (a) frequency response and (b) resistance response of lipid structures formed via vesicle deposition on SiO_2 and γ-alumina. These two films were chosen to study the effect of surface chemistry due to their similar surface roughness properties (see Table 2-1). Upon inspection, the dynamic behavior of the formation of lipid bilayer membranes significantly differed between the SiO_2 and γ-alumina surfaces. As shown in Figure 2-7a, the adsorption process on SiO_2 shows a dynamic lipid bilayer membrane formation behavior occurring in three phases: (1) the frequency shifts to a minimum frequency (Δf_{max} = -87 Hz) in 10 minutes, (2) a frequency increase to a steady state value (Δf_{final} = -53 Hz) in 20 minutes and (3) maintain a steady state frequency; this behavior is similar to previously published bilayer membrane formation results on SiO_2 (when considering system temperature and vesicle diameter) [Reimhult et al., 2002]. The lipid bilayer formation on γ-alumina shows a continual frequency decrease in an exponential decay behavior to a steady state frequency of Δf_{final} = -90 Hz; this behavior is similar to vesicle adsorption without rupture on TiO_2 (when considering system temperature and vesicle diameter) [Reimhult et al., 2002].

In this work, a vesicle can be defined as a shell of single lipid bilayer membrane encapsulating a volume of water. Because of its structure, the mass of each vesicle is a combination of lipid and water molecules. On a SiO_2 surface, the vesicle deposition process is composed of two basic phases, vesicle deposition and vesicle rupture, which is consistent with the frequency behavior described above. The initial frequency decrease correlates to mass adsorption on the SiO_2 surface. The frequency shift and mass adsorption relationship is correlated through the Sauerbrey equation (see equation 2.1):

$$\Delta m = -C_f / \Delta f \qquad (2.1)$$

Thus, the adsorbed mass correlates to vesicles adsorbing on the QCM crystal.

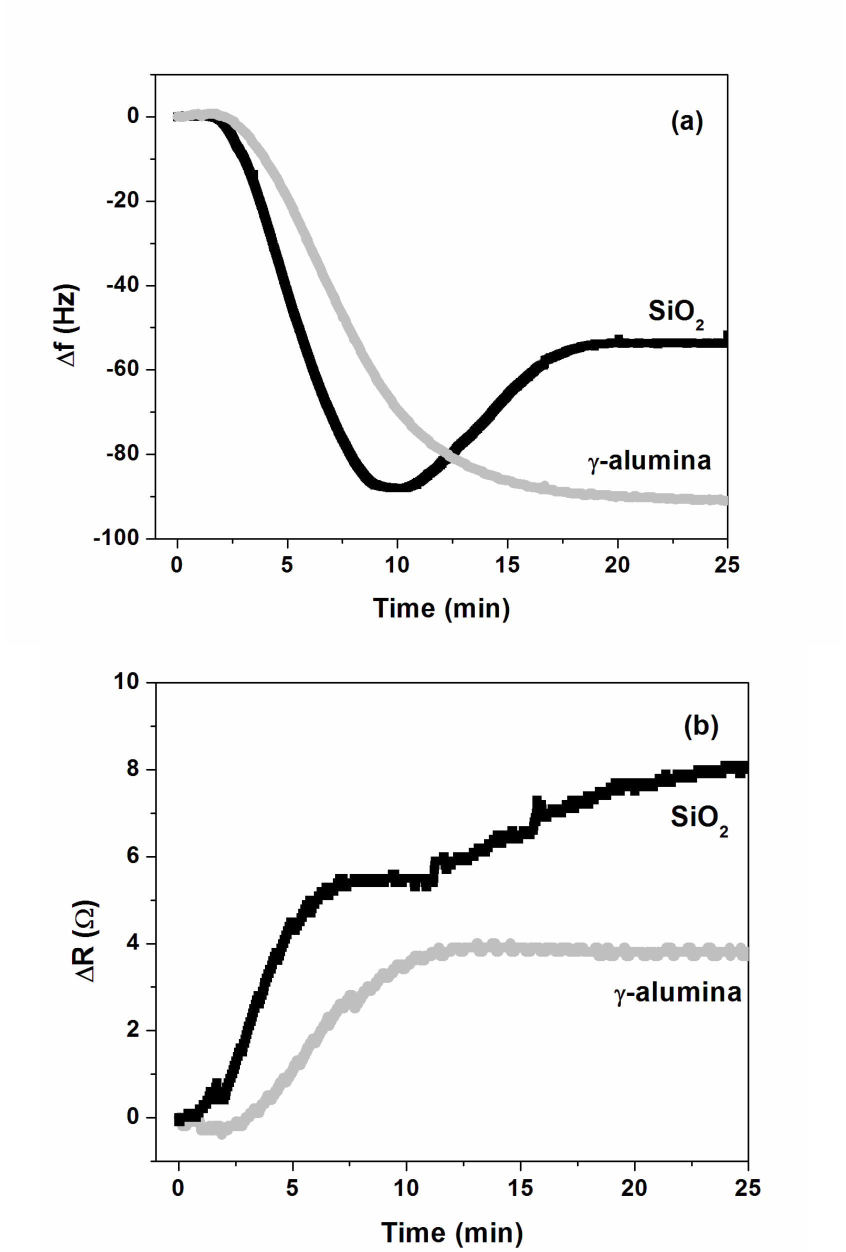

Figure 2-7. Vesicle adsorption behavior on SiO_2 (dense) (black) and γ-alumina (grey) described by (a) frequency and (b) resistance measurements (pH = 8).

The second property that can be measured using the QCM technique is the resistance of the deposited film. The resistance is a measure of the oscillation dampening of the QCM crystal [Rodahl et al., 1997]. Rodahl et al. demonstrated a direct relationship between the thickness of a viscoelastic (non-rigid) thin film and its resistance behavior. They found that as the thickness of a viscoelastic film on the QCM crystal surface increases, the dampening of the crystal oscillation also increases; likewise, a decrease in the viscoelastic film thickness decreases the film resistance to oscillation. Coupled with the frequency shifting behavior of the QCM crystal, the film resistance provides valuable information regarding the morphology of the supported film.

As previously discussed, vesicle adsorption on the QCM surface results in a frequency decrease which correlates to a mass increase in the system (sum of lipid molecules and encapsulated water within its core); this behavior is shown in Figure 2-7a. As the frequency decreases in Figure 2-7a, it is shown that the resistance of the system increases (Figure 2-7b). This can be attributed to the increased film thickness induced by adsorption of the vesicle adsorption (180nm diameter). This is consistent with the behavior described by Rodahl et al. [1997].

The second phase is characteristic of a frequency increase, which corresponds to a mass loss on the surface (Figure 2-7a). When the vesicles adsorb on the surface, they deform to increase the lipid-support contact; this deformation induces surface tension on the vesicle walls causing them to rupture. At vesicle rupture, the encapsulated water is released and the mass remaining on the support surface is only the lipid bilayer shell. Because the water mass is released from the vesicle, there is a net mass decrease of the adsorbed mass on the QCM crystal causing a system frequency increase. Once the vesicles rupture, they form small lipid bilayer membrane islands across the support surface. While vesicle rupture occurs, vesicles continue to adsorb on the surface. These adsorbed vesicles dynamically fuse with the lipid bilayer islands scattered across the crystal surface to form a continuous lipid bilayer membrane.

During this second phase, there is an overall frequency increase indicating a mass decrease within the system. When comparing the frequency increase with the resistance data in Figure 2-7b, the resistance behavior increases while the frequency shift increases. While initially contradictory to Rodahl, et al. and previous lipid bilayer membrane formation work (i.e., Keller, et al., 2000, who found that upon vesicle rupture there was a decrease in dissipation), when considering the surface properties of the present crystal the results can be explained. The crystal itself maintains a surface roughness of 6 nm, which is comparably a higher surface area than supports utilized in other formation studies. The increased surface roughness yields an increase in the available surface area for vesicle adsorption, which increases the adsorption capacity of the surface. Vesicle rupture results in a frequency increase, and should theoretically result in a resistance decrease due to the overall thinning of the film. In this work, the resistance continually increases, which can be attributed to the continual vesicle adsorption on the QCM surface. The effect of the resistance increase due to vesicle adsorption is far greater than the effect of the resistance decrease resulting from rupture; therefore, the system resistance yields a continuous increase during the lipid membrane formation process.

The final formation phase is characterized by a steady state frequency response. This steady state response is indicative of zero mass adsorption/desorption from the surface. Once the entire surface is covered by a single lipid bilayer membrane, mass will not adsorb onto or desorb from the surface of the lipid bilayer membrane, indicating the formation of a stable bilayer membrane. This is mirrored by the steady state value of the frequency response shown in Figure 2-7a for SiO_2. The resistance is also nearly at steady state, with fluctuations possibly stemming from rearrangement of the vesicles within the lipid bilayer system.

On γ-alumina, the frequency and resistance measurements were considerably different from the behavior observed on the SiO_2 surface (Figure 2-7). The frequency response decayed exponentially to a steady state value of -90Hz (Figure 2-7a), while the resistance response exponentially increased to a steady state resistance of 4Ω (Figure 2-7b). A continuous frequency decrease with time indicates continuous mass adsorption on the support surface. If the frequency data in Figure 2-7a is combined with the resistance data in Figure 2-7b, the structure of the continuously adsorbed film can be determined. The steady state resistance value is relatively low, indicating that the final film structure is not predominately viscoelastic. However, because the resistance is not near zero, the film is not a rigid film, which would indicate a single lipid bilayer membrane structure. Thus, the final film structure must be a combination of a single lipid bilayer and adsorbed vesicles within the lipid bilayer membrane. Because of the final required configuration, it is believed that the vesicles adsorb and rupture upon contact to the γ-alumina surface. While the majority of the vesicles rupture upon contact, it is believed that a small fraction of vesicles are embedded within the lipid bilayer membrane which increases the visocelasticity of the film as indicated by the steady state resistance value.

These results are contrary to work done by Groves et al. who found that vesicle fusion does not occur on aluminum oxide films [Groves et al., 1998]. However, it is believed that in their work the vesicles were weakly adsorbed to the surface and were removed during the rinsing step. This also contradicts Nellis et al. [2011] who found that alumina-xerogels promoted bilayer formation as opposed to vesicle adsorption and immediate rupture seen on γ.alumina. It is believed that the formation mechanism differences between Nellis el al. [2011] and this work are due to a difference between the charge density on the surface of the two materials.

2.3.3. Biomembrane formation: effect of buffer solution pH

Zeta potential is the electrostatic potential near to the surface of a particle in solution [Colloidal Dynamics, 1999]. Several factors affect zeta potential, including particle concentration, solution conductivity, and most importantly, solution pH. As the solution pH is varied, particle surface charge is altered due to the variation in the ionization state of the surface functional groups; typically a pH increase results in a zeta potential decrease. The zeta potential is often engineered through pH adjustment to optimize the particle-surface interaction; a greater zeta potential difference enhances the adhesion between the particle and the surface [Saravanan & Subramanian]. The zeta potential of zeolite [Noack, et al., 2006], γ-alumina [Song, 2005], zirconia [Saravanan & Subramanian] and vesicles of similar lipid chemistry [Fatouros et al., 2005] are summarized in Figure 2-8. The two pH values used in this study were pH = 8 and pH = 4.

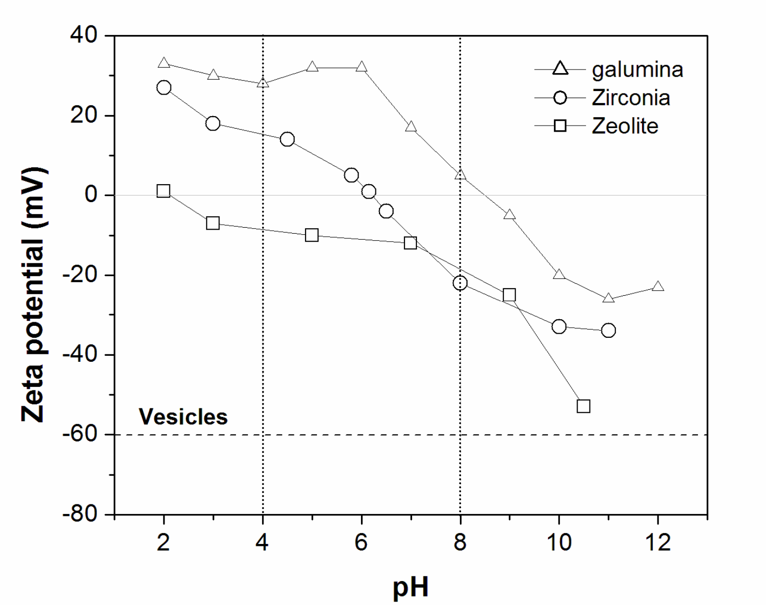

Figure 2-8. Zeta potential properties of γ-alumina, zirconia, zeolite and vesicles of similar surface chemistry to the vesicles used in this study.

2.3.3.1. γ-alumina

The lipid bilayer membrane formation process was evaluated on γ-alumina using solutions of two different pH values to evaluate the effect of solution pH on the formation of a lipid bilayer membrane. Figure 2-9 summarizes the (a) frequency and (b) resistance response for lipid bilayer formation process using a buffer solution with pH = 8 and pH = 4. As previously discussed, the frequency decreases in an exponential decay behavior when using a buffer solution of pH = 8. Combined with the resistance data, this is indicative of vesicle rupture upon contact with the surface, with a final frequency shift of Δf_{final} = -90 Hz. When the pH is adjusted from 8 to 4, the dynamic system behavior changes from a monotonically decreasing frequency shift to a multidirectional frequency shift (Figure 2-9a). Likewise, the resistance behavior experiences a steady increase followed by a change in slope. Qualitatively, the new dynamic system behavior is similar to that of bilayer formation on a SiO_2 surface, with a Δf_{max} = -84 Hz and a final Δf_{final} = -74 Hz after 12 minutes and 30 minutes, respectively.

As shown in Figure 2-8, as the pH lowered from pH = 8 to pH = 4, the magnitude separating the zeta potential of γ-alumina and the lipid vesicle increased yielding greater attraction between the vesicle particle and the γ-alumina surface. This increased attraction would alter the adhesion attraction potential between the vesicles and the support. It is believed that a decrease in the buffer pH created a charge shielding effect on the lipids causing a change in the rupture kinetics of the surface. This charge shielding may minimize the surface/vesicle charge and could reduce the rupture potential of each vesicle. The decreased rupture potential would result in a system similar to SiO_2, which would require a critical vesicle concentration on the support surface to induce vesicle rupture. The multidirectional behavior of the frequency shift in Figure 2-9a for pH = 4 indicates that adsorption does occur upon rupture as seen with the pH = 8 system. Additionally, the system resistance the pH = 4 system is high compared to the pH = 8 system; this shows that the lipid film under pH = 4 is largely viscoelastic which indicates that a high percentage of the film is comprised of embedded vesicles. This behavior is indicative of vesicle adsorption prior to rupture. The resistance multi-directional behavior shown in Figure 2-9b for the pH = 4 system indicates that rupture does occur after adsorption. However, because the magnitude of frequency increase or resistance decrease is relatively low, the response indicates that there is a high percentage of vesicles embedded within the lipid bilayer membrane on the γ-alumina system (pH = 4).

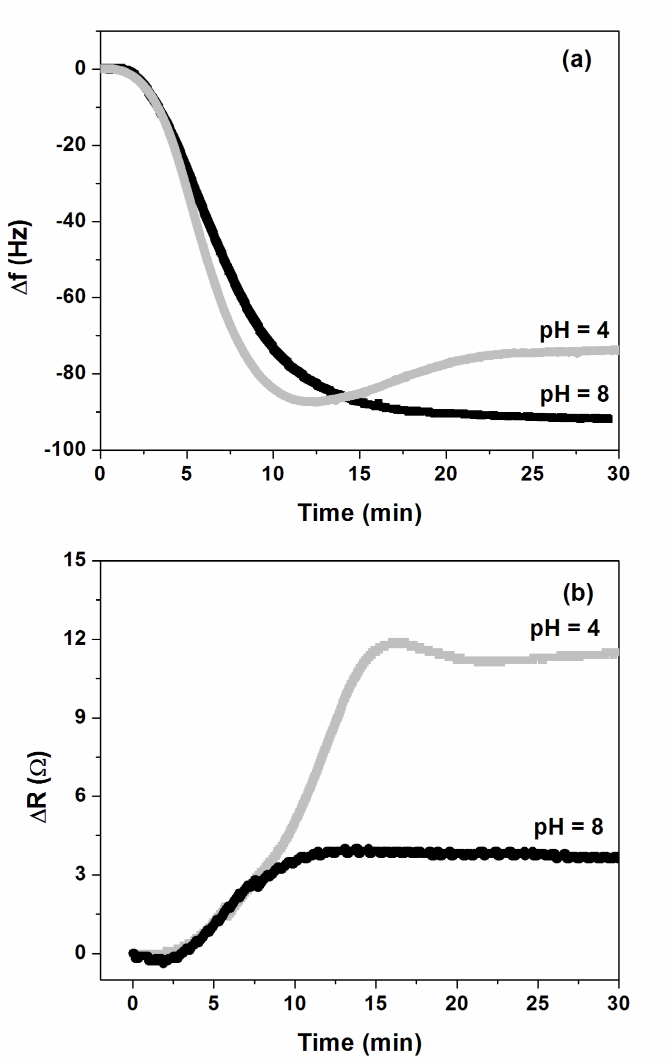

Figure 2-9. Vesicle adsorption kinetics on γ-alumina with a buffer solution at pH = 8 (black) and pH = 4 (grey) comparing (a) frequency shift and (b) resistance shift.

2.3.3.2. Mesoporous YSZ

Figure 2-10 shows the lipid bilayer formation process on mesoporous YSZ films using a solution of pH = 8 and pH = 4. The frequency shift behavior (Figure 2-10a) and resistance behavior (Figure 2-10b) between conditions is the same, with a frequency decrease in an exponential decay fashion to a maximum shift of Δf_{final} = -210 Hz (pH = 8) and Δf_{final} = -240 Hz (pH = 4), each in 250 minutes. The final resistance values were found to be $\Delta R_{ph=8}$ = 110 Ω and $\Delta R_{ph=4}$= 63 Ω. The exponential decay frequency behavior (Figure 2-10a) and the exponential increase resistance behavior (Figure 2-10b) is indicative of vesicle adsorption without rupture on the support surface. Quantitatively, the vesicle adsorption rate for vesicles using a buffer solution titrated to pH = 4 is kinetically faster than the adsorption rate under pH = 8 conditions. The gap in data points for Figure 2-10, pH = 4 was due to malfunctioning equipment, which caused a data gap. The lipid flow was constant throughout the duration of the experiment; thus, the vesicle adsorption behavior was uninterrupted throughout the experiment and data integrity before and after the malfunction is maintained.

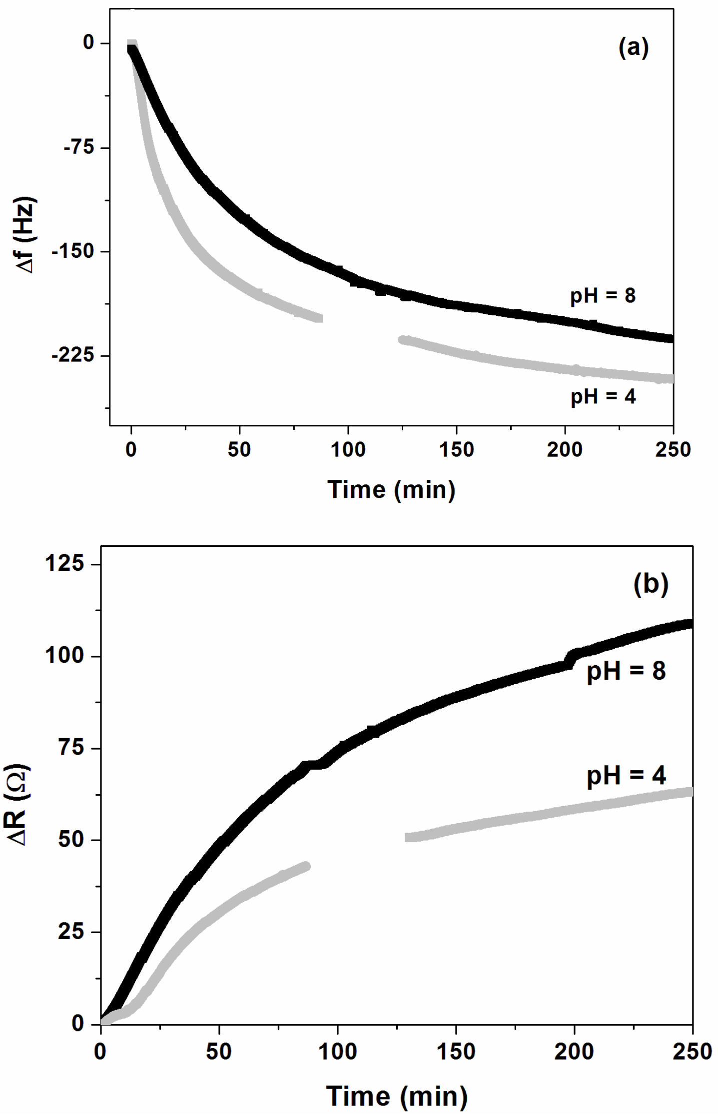

Figure 2-10. Vesicle adsorption kinetics on mesoporous YSZ using a vesicle solution at pH = 8 and pH = 4 showing (a) frequency and (b) resistance.

The mesoporous YSZ film is an MO_2/N_2O_3 hybrid system (M = Zr, N = Y) and would maintain a hybrid surface chemistry of SiO_2 and γ-alumina (Al_2O_3). Previous work has shown that surfaces with similar surface chemistry (i.e. SiO_2 and TiO_2) do not necessarily exhibit the same lipid bilayer formation mechanism [Reimhult et al., 2002]. Therefore, it is unknown if the behavior on a YSZ surface with a low (and comparable) surface roughness would behave similarly to SiO_2 or γ-alumina. Because the mesoporous YSZ film has distinct topographical features, the surface topography plays a significant role in the formation behavior of lipid structures on its surface and would most likely override the surface chemistry effect characteristic of the material. Previous work [Cremer & Boxer, 1999] has found that surface scratches or barriers hinder the formation of a continuous, fluid lipid bilayer membrane. It is believed that a rough surface inhibits rupture after vesicle adsorption due to a minimized surface/vesicle contact; this contact would be needed to induce vesicle deformation and then rupture. Therefore, due to the rough surface topography, it is predicted (and confirmed) that vesicle monolayer adsorption occurs on the mesoporous YSZ surface.

Alteration of the buffer solution pH quantitatively affected the vesicle adsorption rate (see Table 2-2), but did not change the overall system behavior. Similar to γ-alumina surface, variation in the solution pH affected the zeta potential of the material (see Figure 2-8). Therefore, the increased zeta potential difference between the vesicle and surface zeta potential would cause greater attraction between the surface and vesicle thus enhancing the vesicle adsorption rate. The increased magnitude of adsorption (difference of 15 Hz) can also be explained by increased adsorption due to the pH. Because the adsorption rate is enhanced due to the pH change, it is likely that additional vesicles were adsorbed due to an increased rate of adsorption driven by buffer solution pH. This conclusion is supported by the high resistance of the mesoporous YSZ supported film induced by the greater amount of vesicles adsorbed on the surface.

2.3.4. Biomembrane formation – effect of surface roughness

2.3.4.1. SiO_2 materials: Zeolite and SiO_2 films

SiO_2 and zeolite were chosen to evaluate the surface roughness effect because of their similar surface chemistries but varying surface roughness properties. Figure 2-11 summarizes the lipid bilayer membrane formation process [measured by (a) frequency and (b) resistance] via vesicle deposition on SiO_2 and zeolite supports. Qualitatively, the lipid bilayer membrane formation behavior measured by the frequency response is similar. On zeolite, the QCM experiences a frequency decrease until Δf_{max} = -120 Hz is reached where the frequency directionality reverses until it reaches Δf_{final} = -69 Hz. The resistance shift mirrors the frequency shifting behavior; the resistance increases to 39 Ω and reverses directionality to 33 Ω. The frequency shifts on the SiO_2 surface were Δf_{max} = -87 Hz and Δf_{final} = -53 Hz (a 30-40% difference in the adsorption/rupture frequency shifts between SiO_2 and zeolite). The resistance on the SiO_2 film increased to 6 Ω eventually reaching a maximum at 8 Ω. The frequency shifting behavior on the zeolite surface is qualitatively similar to the behavior on the SiO_2 surface, indicating the formation of a lipid bilayer membrane structure. While qualitatively similar, the quantitative kinetic behavior varies between SiO_2 and zeolite thin films.

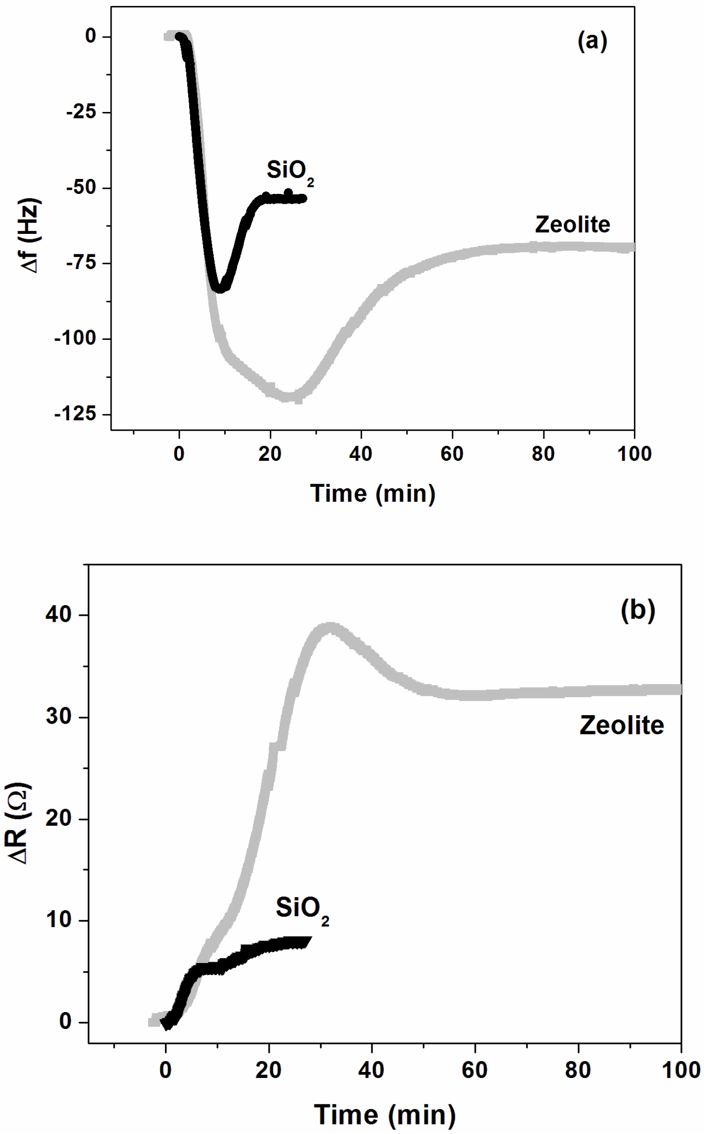

Figure 2-11. Lipid bilayer membrane formation on SiO2 and zeolite, measured by the (a) frequency and (b) resistance (pH = 8).

As shown in Figure 2-11 and summarized in Table 2-2, the lipid bilayer membrane formation process occurs more rapidly on the SiO$_2$ surface than on the zeolite surface. The vesicle adsorption rate (denoted by the frequency shift) on SiO$_2$ was found to be 8.7 Hz/min and occurred within 10 minutes, while vesicle adsorption rate on zeolite was observed to be 4.8 Hz/min within 25 minutes. The transition to the final lipid bilayer state occurred within an additional 10 minutes and 55 minutes on the SiO_2 and zeolite films, respectively. The decreased adsorption rate and required time for adsorption for the zeolite film can be explained by the increase in the available surface area on the zeolite film when compared to the SiO_2 surface; the surface area of the zeolite thin film is 400% greater than the SiO_2 surface area. Thus, due to the increasing surface area the zeolite film requires a larger quantity of vesicles to adsorb and rupture on the surface (when compared to the SiO_2 substrate) to synthesize a complete lipid bilayer membrane. Likewise, the increased zeolite surface area requires additional vesicles to reach a critical vesicle saturation required to induce vesicle rupture [Goksu et al., 2010]. As evidenced by these behaviors, the Δf_{max} was 33 Hz larger for zeolite than for SiO_2. Likewise, Δf_{final} is 16 Hz greater for the zeolite surface due to the increased mass required to synthesize a continuous lipid bilayer membrane. Similarly, the rupture kinetics can be explained by the same surface area principle. The required time for the formation of a continuous lipid bilayer membrane is greater due to the additional time required for vesicle rupture and fusion processes due to the increased support surface area [Goksu et al., 2010].

In addition to frequency, the film resistance was measured (Figure 2-11b) and can be used to further detail the formation process and final state of the membrane. As described previously, the resistance behavior of SiO_2 films showed a continuous increase in resistance, eventually reaching a steady state value of 8 Ω. This continuous resistance increase is attributed to the continuous adsorption of vesicles on the SiO_2 surface, a process that also occurs during vesicle rupture on the support surface. It is believed that the adsorption behavior dominated the resistance behavior due to the increased surface area (an increased surface area required additional adsorbed vesicles to form a continuous lipid bilayer membrane). On the zeolite surface, the resistance behavior mirrored the frequency behavior, showing a resistance increase followed by a resistance decrease. The final resistance for the zeolite supported lipid film was 39 Ω, a resistance nearly five times greater than the SiO_2 supported lipid film. This indicates that the lipid film supported on the zeolite maintained a more viscoelastic final film structure than the SiO_2 supported lipid film. This indicates a higher percentage of vesicles embedded within the zeolite supported film when compared to the SiO_2 supported film. The difference in resistance behavior can be attributed to a difference in the surface area. With the zeolite film, the surface contours limit the accessibility of adsorbed vesicles. Therefore, a higher percentage of adsorbed vesicles is required to induce vesicle interaction that would cause rupture. Due to the large amount of vesicles adsorbed on the surface, vesicle adsorption after rupture would be limited. Therefore, vesicle rupture would dominate the adsorption/rupture behavior on the zeolite surface. This would result in a resistance decrease for the zeolite supported lipid film as opposed to the resistance increase and plateau seen in the SiO_2 film.

Table 2-2. *Formation kinetics of a lipid bilayer membrane on inorganic thin films before and after vesicle rupture.*

Substrate Material	Substrate Surface Roughness	pH	Before vesicle rupture t_1 *(min)*	Δf_1 *(Hz)*	k_1 *(Hz/min)*	After vesicle rupture t_2 *(min)*	Δf_2 *(Hz)*	k_2 *(Hz/min)*
SiO_2	6 nm	8	10	-87	8.7	20	-53	3.4
Zeolite	21 nm	8	25	-120	4.8	80	-69	0.9
γ-alumina	4 nm	8	30	-90	3.0	-	-	-
		4	12	-84	7.0	30	-74	2.5
YSZ (mesoporous)	41 nm	8	250	-210	0.8	-	-	-
		4	230	-240	1.0	-	-	-
YSZ (macroporous)	25 nm	4	230	-190	0.8	-	-	-

This behavior is similar to results obtained by Weng et al. [Weng et al. 2004] who measured the membrane formation behavior on a xerogel surface (another SiO_2 based system). In their work, the contours induced by particle packing created a surface roughness of 70 nm (compared to 21 nm in this work). They determined that the increased surface area decreased the adsorption rate by 30 times; the behavior was attributed to the additional surface roughness induced by particle contours which limited the ability for the vesicles to interact and rupture to form a continuous membrane [Weng et al. 2004]. The results in Figure 2-11 are also confirmed by Subramaniam et al. [2010], who examined the curvature effects on the quality of lipid bilayer membranes using topographically patterned polydimethylsiloxane (PDMS). Using FRAP analysis, Subramaniam et al. [2010] found that the differences between the diffusion coefficients measured on the planar and curved areas of the substrate were experimentally insignificant. Together with Weng et al. [2004], surface roughness will affect the vesicle adsorption kinetics while preserving the diffusion potential on a SiO_2 surface with curvature effects.

2.3.4.2. Zirconia materials: mesoporous and macroporous YSZ films

Surfaces of identical surface chemistry but varying roughness were chosen for this study to evaluate the effect of surface roughness on the vesicle adsorption kinetics. Figure 2-12 summarizes the vesicle interaction behavior with the macroporous YSZ and the mesoporous YSZ surfaces in terms of (a) frequency and (b) resistance. In this study, vesicles were prepared via sonication with a buffer solution at pH = 4. Buffer solution at pH = 4 was chosen as it has been shown to increase formation kinetics [Cremer & Boxer, 1999; current work]; a lower pH will allow for a better comparison between YSZ materials. Figure 2-12a shows the frequency for each material decreasing in an exponential decay behavior to a final frequency shift of -190 Hz (macroporous YSZ) and -240 Hz (mesoporous YSZ). The exponential decay in the frequency behavior seen in Figure 2-12a is indicative of vesicle adsorption without rupture. This is confirmed by the resistance data in Figure 2-12b, which shows an exponential increase in the resistance response. Each of these behaviors can be explained by the roughness of the surface. As shown in Figure 2-2c/d and Figure 2-3c/d and summarized in Table 2-1, each YSZ surface is relatively rough with the mesoporous surface more rough and disjointed than macroporous surface. The disjointed nature of the film does not allow for sufficient deformation of the vesicle upon adsorption which is required for vesicle rupture. Thus, a vesicle monolayer is formed on each YSZ surface instead of a single lipid bilayer structure. This is also confirmed by the large resistance of the film, as shown in Figure 2-12b.

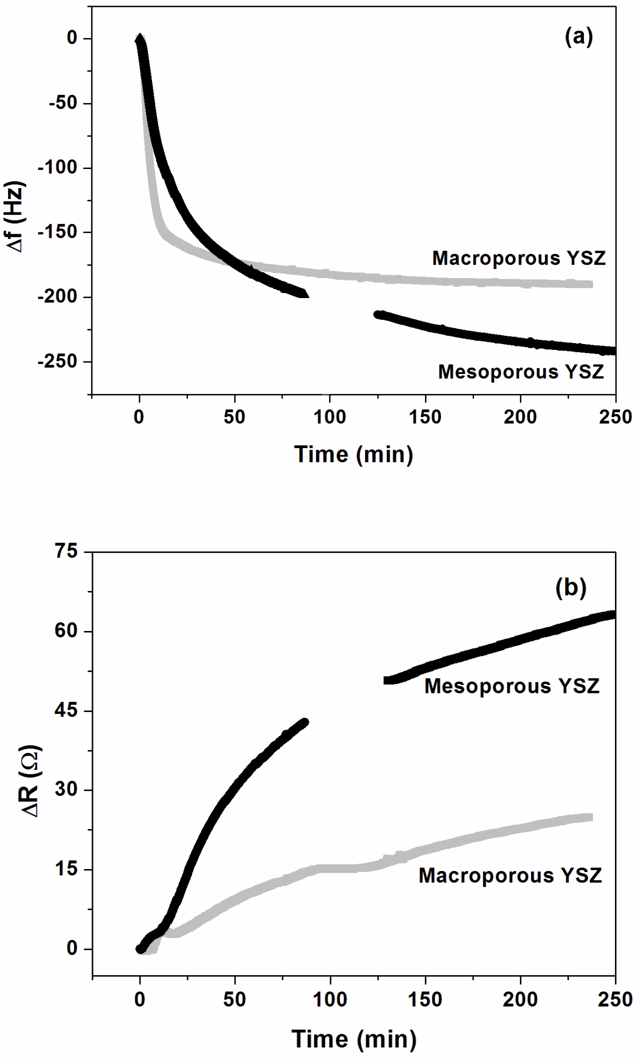

Figure 2-12. Vesicle adsorption kinetics on macroporous YSZ and mesoporous YSZ at pH = 4 measured by (a) frequency and (b) resistance.

It is also important to note that the final frequency shift of the mesoporous film is 50 Hz larger than that of the macroporous film (Figure 2-12a). This can be explained by additional total surface area available for adsorption. As previously discussed, the mesoporous YSZ surface has a disjointed surface topography while the macroporous YSZ has a comparatively smoother surface. The disjointed nature of the film will decrease the propensity for vesicle rupture. However, the disjointed nature of the film does increase the available surface area, which would promote additional adsorption of vesicles on the film surface. This behavior is supported by the higher frequency shift on the mesoporous support. The frequency behavior is supported by the increased resistance response for vesicle adsorption on each surface, as shown in Figure 2-12b. Continuous vesicle adsorption onto each YSZ film type both yield higher resistance, which is consistent with a film of increased viscoelasticity. The resistance for the film supported by the mesoporous YSZ film is substantially higher than that for the macroporous YSZ film. This can also be explained by the increased amount of vesicles adsorbed on the surface with the increase of available surface area. This would lead to higher overall viscoelasticity, which is confirmed by the increased resistance of the film structure.

The adsorption rate of the vesicle monolayer on the macroporous YSZ film was evaluated by the frequency response and was found to be 1.0 Hz/min and while the adsorption rate of the mesoporous YSZ film was measured to be 0.8 Hz/min. These results are also indicative of the surface roughness of the two films. The synthesized macroporous YSZ film has a surface roughness of 25 nm, whereas the surface roughness of the mesoporous YSZ film is 41 nm, as shown in Table 2-1. Since the macroporous YSZ film is a smoother surface, there is more available continuous surface area for the vesicles to adsorb on the surface. Therefore, the adsorption rate would proceed more rapidly on the macroporous support due to the increased available smooth surface area which is conducive to rapid vesicle adsorption. The mesoporous film has an increased surface roughness, which is characterized by greater surface discontinuities and thus does not allow for rapid vesicle adsorption.

2.4. Conclusions

The formation mechanism of eggPC lipid bilayer membranes and vesicle layer adsorption was explored on porous inorganic films of differing surface chemistries and surface topographies and under various buffer pH. A summary of the results found in this work can be found in Figure 2-13. The study found that a single lipid bilayer membrane was formed only on the zeolite (silicalite) surface, due to its similar surface chemistry to SiO_2 (pH = 8). It was found that the surface contours on the zeolite support increased the formation time by 400%. While the formation time was increased, the basic formation process (vesicle adsorption and vesicle rupture) was preserved. The buffer pH was altered to determine its effect on vesicle adsorption behavior. It was found that vesicle ruptured upon adsorption (without vesicle surface accumulation) on the γ-alumina surface under pH = 8. However, under pH = 4, a multi-step vesicle adsorption/rupture processes was found to govern the formation of a hybrid vesicle/lipid bilayer system. A buffer pH adjustment also increased the vesicle adsorption rate on mesoporous YSZ, but did not alter the qualitative behavior of the vesicle adsorption (without rupture) process. Surface roughness was examined using SiO_2 based and zirconia based materials. SiO_2 and zeolite materials were found to maintain bilayer formation behavior, however the increased surface roughness of the zeolite film decreased the formation kinetics. Zirconia materials were each found to promote vesicle adsorption without rupture. However, increased surface roughness was found to decrease adsorption kinetics due to the inaccessibility of vesicles to deform and rupture on the surface due to the jagged structure of the film. However, the additional surface area induced by the surface roughness caused a greater magnitude of adsorption due to the increased surface area. These new porous inorganic materials have emerged as novel supports for lipid bilayer membranes and lipid structures for potential applications for transmembrane ionic gradient studies.

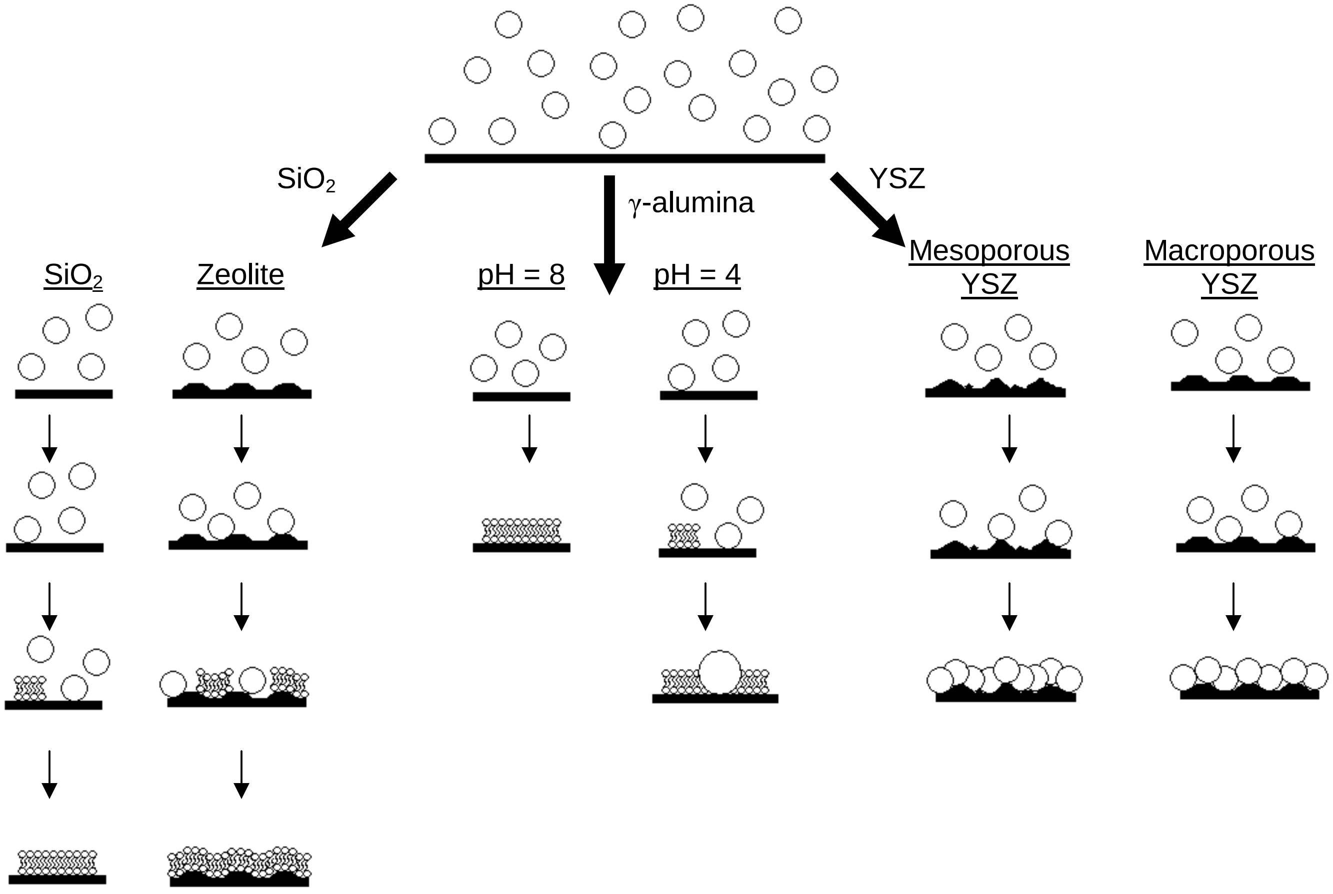

Figure 2-13. Schematic of lipid bilayer formation and vesicle monolayer adsorption models observed in this work.

Chapter 3

STUDY ON THE FORMATION OF LIPID BILAYER MEMBRANES FORMED ON SILICA FIBERS BY DOUBLE-LONG PERIOD FIBER GRATING LASER REFRACTOMETRY

3.1. Introduction

In Chapter 2, the kinetics of vesicle adsorption was explored on porous planar supports. It was determined that the formation rate of lipid bilayer membranes on porous supports were significantly affected by solution pH, surface chemistry and surface roughness. In Chapter 1, the limitations of current supported lipid bilayer membrane technology were discussed. This included the formation and characterization of lipid bilayer membranes on two types of supports: porous inorganic supports and cylindrical supports. As discussed, cylindrical supports will be valuable in biosensing applications.

Biosensors have recently become important in modern biotechnology due to their rapid response time, high sensitivity and in situ detection capability, thus providing an effective tool for studying a wide variety of biological systems [Rokhina et al., 2009]. Several sensing platforms, such as electrochemical, acoustic, calorimetric and optical biosensing devices, have been fabricated to allow for a comprehensive study of both biological process characteristics and selective molecular binding of desired molecules [Paddle, 1996]. Among these techniques, optical fiber biosensing has attracted much attention because of its advantages of small size, continuous monitoring capabilities and the ability to probe otherwise inaccessible regions [Wolfbeis, 2006].

Klee et al. [Klee et al., 1995] recently used a silica optical fiber evanescent wave sensor (EWS) platform to monitor the formation and removal processes of biotin incorporated lipid bilayer membranes. These processes were demonstrated by monitoring the formation and desorption properties of lipid bilayer membranes on a glass optical fiber surface using luminescent labeled lipid molecules. This study demonstrated the feasibility for complete fiber surface regeneration over several successive lipid bilayer formation and removal cycles. Similarly, Abel et al. [Abel et al., 1996] utilized the EWS platform to fabricate a novel optical biosensor engineered to possess rapid surface regeneration after multiple DNA binding events on the fiber surface. Recently, novel optical fiber devices have been fabricated to broaden the available platforms for biosensing applications. One such technique involved a fiber optic coupler based refractive index sensor used to study concentration dependent binding of streptavidin [Tazawa et al., 2007]. Another optical fiber technique utilized two-photon fluorescence measurements to monitor the binding capabilities of a dendrimer-based drug delivery agent for the treatment of cervical cancer [Ye et al., 2002]. The availability and multi-functional uses of optical fiber sensor technology allow for the development of highly effective and miniaturized biosensors for a wide variety of applications [Wolfbeis, 2006].

Refractometry is an optical sensing technique used for process characterization which identifies a specific process by using light to probe the refractive index changes of a material. Refractometry-based optical fiber chemical sensors have been demonstrated to investigate trace organics in both vapor and liquid phases [Zhang et al., 2005; Xiao et al., 2005]. High sensitivity biosensors can also be developed by incorporating refractometry with a long period fiber grating (LPFG). For example, refractometry based LPFG devices have been used to study saline separateness of bovine serum albumin (BSA) and mice-immunoglobulin G (M-IgG) protein solutions [Mao et al., 2007], measure binding and hybridization of DNA molecules [Chen et al., 2007], and, with a coating of silica nanospheres on the fiber surface, to detect antigliadin antibody at low concentrations [Corres et al., 2008]. The studies show that LPFG is a good biosensing platform for building various biosensors.

A supported lipid bilayer membrane biosensor can be fabricated by synthesizing a lipid bilayer membrane on the sensing element (such as an LPFG) yielding a highly sensitive biosensor platform. Structural changes in the membrane (such as DNA binding events) cause a change in the film properties (e.g., refractive index) which is converted to an optical signal by the highly sensitive LPFG. Such biosensors can find a number of applications including uses in studying processes such as DNA hybridization or molecular binding within a natural cellular environment. The development of supported lipid bilayer membrane-based optical fiber biosensors requires a fundamental understanding of lipid membranes and their behavior on the surface of silica optical fibers.

This chapter reports a study of the formation of a supported lipid bilayer membrane on silica fiber surface by a new double-grating LPFG system. A novel LPFG sensing method is developed to minimize environmental effects present during sensing. This chapter will demonstrate how this method lends to the fabrication of a highly sensitive biosensor for supported lipid bilayer membrane technology.

3.2. Materials and Methods

3.2.1. Materials

The lipids used throughout experiments were L-α-phosphatidylcholine lipids (eggPC) (99%, Avanti Polar Lipids) and were used as received. Gramicidin D was purchased from Sigma-Aldrich and was diluted in ethanol (200 proof, Fisher Scientific). Sodium chloride (99.0%) and Tris (Ultrapure) were purchased from Mallinckrodt Chemicals and MP Biomedicals, LLC, respectively. The gas used for chloroform removal during vesicle preparation was Argon (research grade) purchased from Air Liquide. Isopropanol was purchased from Fisher Scientific (reagent grade). Ultrapure water was made using a Millipore Academic filtration system (18.2 MΩ).

3.2.2. Vesicle Formation and Characterization

The preparation procedure for vesicle solutions is identical to that found in Chapter 2. The Tris buffer was 100mM NaCl and 10mM Tris and maintained at pH = 8. Stock vesicle solutions were made at a concentration of 0.8 mg/mL and further diluted to desired lipid concentrations (0.1 mg/mL or 0.4 mg/mL). Gramicidin was incorporated into the lipid film by removing the ethanol solvent using a gentle stream of argon gas after the lipid drying step; all subsequent steps in the vesicle preparation process are the same as detailed in Chapter 2. The final Gramicidin concentration was 0.1 mg/mL solution.

3.2.3. Optical Fiber Preparation and Surface Characterization

The optical fiber used to fabricate the LPFG was a Corning SMF-28 single mode optical fiber with a 9 μm core diameter and a 125 μm cladding diameter made of germanium-doped silica and pure silica, respectively. The polymer protection layer on the fiber surface was removed mechanically using a polymer stripper (Micro-Strip precision stripper), followed by successive low-power sonication (Cole-Parmer bath sonicator, model 8890) treatments in isopropanol and ultrapure water. The surface of the fiber was examined by scanning electron microscopy (Figure 3-1) and no surface scratches or foreign materials were observed thus verifying surface continuity after polymer removal.

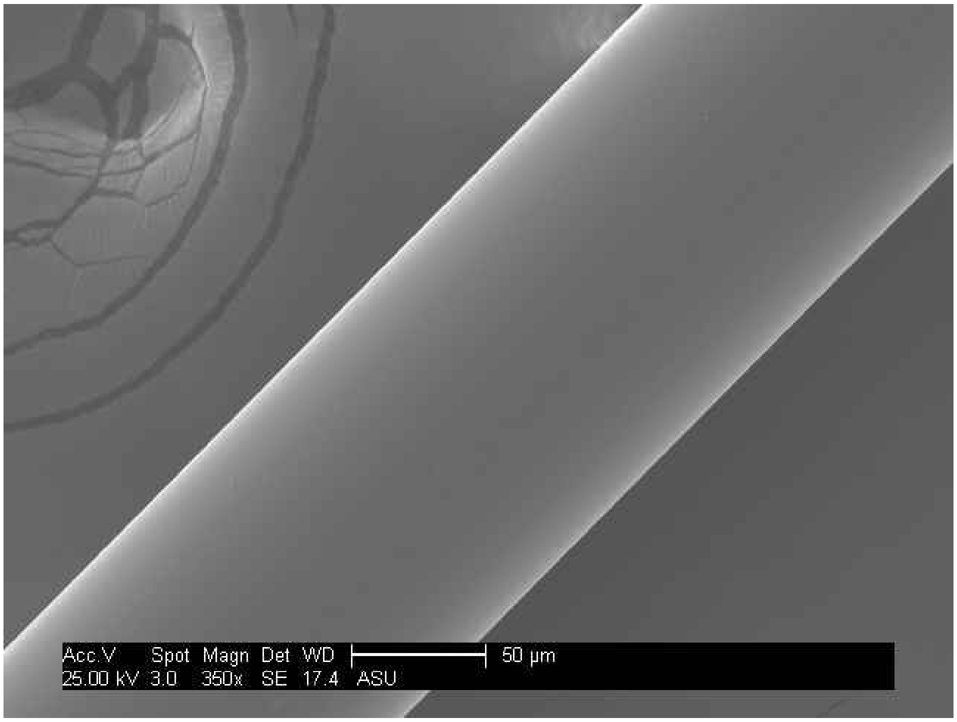

Figure 3-1. Silica optical fiber used as supporting material for lipid bilayer membranes.

The LPFGs were made by point-by-point CO_2 laser irradiation (Firestar V20, Synrad, Inc) on the optical fiber, causing a periodic refractive index modulation inside the fiber core. Several LPFGs of varying grating periods were fabricated for the optical study of sensor functionality. The gratings had periods ranging between 512 μm and 525 μm (the grating period used for each test is noted in the associated figure caption) and all LPFGs had 100 periods. Before each experiment, the LPFG surfaces were cleaned via low-power sonication in isopropanol and ultrapure water for 5 minutes each, and immediately placed into the incubation cell and submerged in ultrapure water to minimize surface contamination. Figure 3-2 shows the three-layered structure of the LPFG immersed in the Tris buffer with lipid layer formed on the surface of the fiber (illustrative purposes only and not to scale).

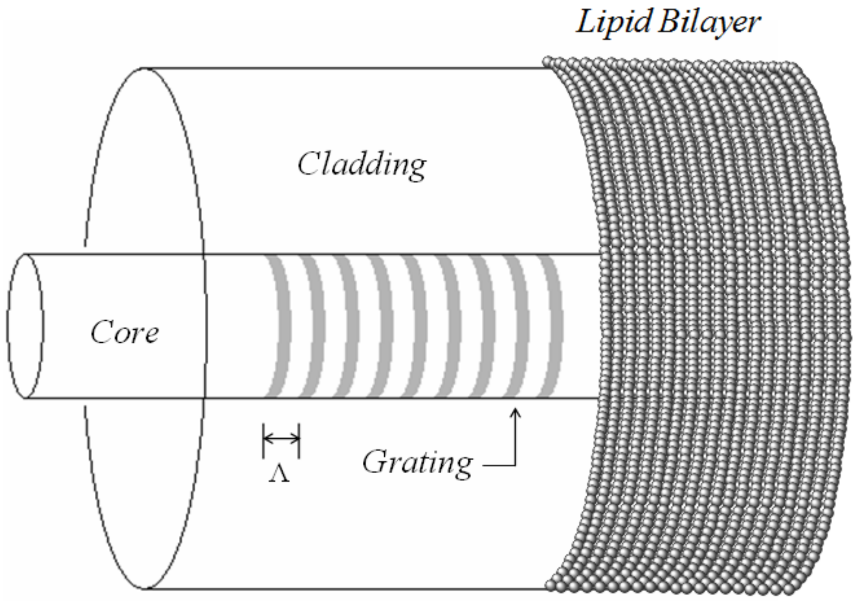

Figure 3-2. Structure of three-layer long period fiber grating including the core, cladding, and lipid thin film immersed within the Tris buffer system (the gray stripes on the core indicate fiber gratings).

3.2.4. Optical Measurements

Following the cleaning, the sensing and reference LPFGs were carefully inserted into two homemade Teflon incubation cells in series, as schematically shown in Figure 3-3.

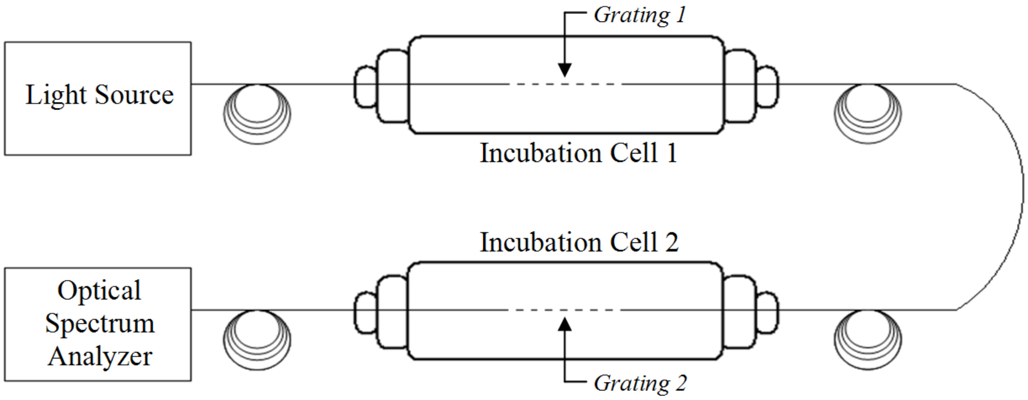

Figure 3-3. Schematic of the optical measurement system and long period fiber grating incubation cells for grating immersion.

The Teflon incubation cells allow approximately 13 cm of the optical fiber, including the grating section of approximately 5 cm, to remain within an aqueous system without stressing the fiber. A constant liquid level is maintained within the Teflon incubation cells through the aid of septums used to eliminate leakage during measurement. Lipid solution and blank buffer solution were simultaneously introduced into the sensing and reference incubation cells and resonance coupling wavelength measurements were immediately recorded to monitor the bioaccumulation on the fiber surface of the sensing LPFG. The broadband source was constructed by multiplexing a C-band (BBS 1550A-TS by AFC Technologies) and an L-band (HWT-L-BS by Highwave Optical Technologies) erbium doped fiber amplified spontaneous emission (ASE) sources, which covered the spectral range from 1530 nm to 1630 nm. The LPFG transmission spectrum was detected by an optical spectrum analyzer (70952B by Hewlett-Packard).

The transmission spectra were measured in two separate wavelength intervals during experimentation: 100 nm, or 5 nm spans. The 100 nm span was used to determine the functionality of the LPFGs in various refractive indices through immersion in air and water (refractive indices of 1.00 and 1.33, respectively). The 5 nm spans were used to detail the resonance coupling wavelength with higher resolution. Regardless of the span width used, the spectra were separated into 1000 discrete units. Therefore, a smaller wavelength scan will give greater resolution when measuring the resonance coupling wavelength. Each collected measurement is an average of two spectra, and the standard error associated with each experiment is 5%.

3.3. Results and Discussion

3.3.1. Characteristics of Double-Grating LPFG System

A primary difficulty with the use of LPFG to detect the formation process of a supported lipid bilayer membrane is the effect of environmental fluctuations (such as temperature or vibration) on the response of the sensing element causing inaccurate measurements. Therefore, a double grating system would allow for correction of the environmental contributions to the sensor response and yield an accurate sensor behavior. Figure 3-4 shows the resonance coupling wavelength (wavelength of minimum transmission) for a single grating (Λ = 522 μm) and a double grating system (Λ = 515 μm and 524 μm).

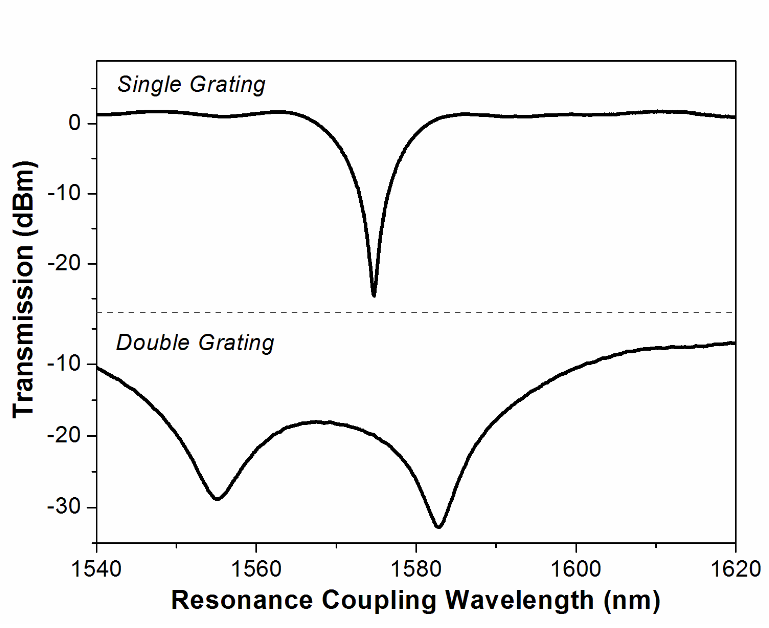

Figure 3-4. Verification of single grating and double grating system functionality when immersed in a Tris buffer solution.

A double grating system is similar to the single grating system shown in Figure 3-3 except only a single incubation cell for grating immersion is used; this single grating is directly connected to both the light source and the optical spectrum analyzer. During testing, each grating was immersed in a pure water solution and the resonance coupling wavelength was measured. The single grating system (top spectrum) shows a single inverse peak at the resonance coupling wavelength of 1575 nm. The double-grating system (bottom spectrum) shows two separate inverse peaks at 1555 nm and 1583 nm corresponding to Grating 1 and Grating 2, respectively.

When two gratings are connected in series, their individual transmission spectrum might overlap to create a cross-coupling effect to each other. It is important to verify that the two gratings in the double-grating system provide independent responses. Grating independence signifies that an effective cladding refractive index variation (thus a resonance coupling wavelength shift) in one grating will not cause a shift in the resonance coupling wavelength of the second grating. To test the grating independence, Grating 1 was exposed to increasing isopropanol concentrations (20 vol%, 30 vol%, 40 vol%) while Grating 2 was exposed to a constant solution of pure water. The results are shown in Figure 3-5.

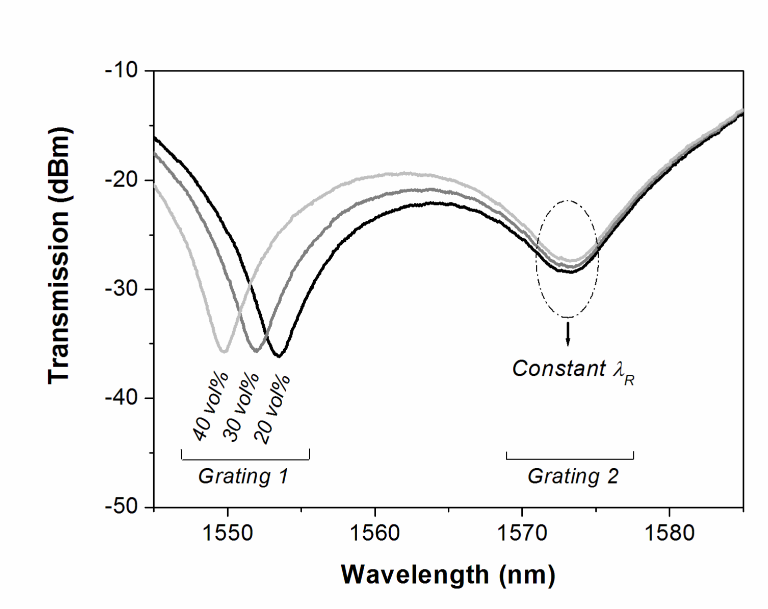

Figure 3-5. Grating independence with varying concentration of IPA surrounding Grating 1 while Grating 2 has a constant bulk concentration of 0 vol% IPA.

The varying isopropanol concentrations of 20 vol%, 30 vol%, and 40 vol% correspond to proportionally increasing refractive indices which therefore cause a decrease in resonance coupling wavelength of Grating 1 (Λ = 516 μm). However, the position of the resonance coupling wavelength for Grating 2 (Λ = 521 μm) remains constant. A shift of 3.2 nm in the Grating 1 spectrum corresponded to a shift of 0.10 nm in the resonance coupling wavelength of

Grating 2. The cross coupling effect was 3.3%. This proves that a wavelength shift in one grating of a double-grating system (with a resonance wavelength separation of 20 nm) will only cause an insignificant wavelength shift in the second grating.

To examine the impact of the environment on the response of the two gratings, the transmission spectrum of the double-grating system was immersed in air and ultrapure water. Air was chosen to elucidate the baseline mode coupling characteristic of the LPFGs. Ultrapure water was chosen because it is the primary component of both the Tris buffer solution and the vesicle solution. The refractive indices along with the associated resonance coupling wavelength in each media can be found in Table 3-1.

Table 3-1. *Summary of properties for air and water used for evaluating sensing functionality*.

Medium	Refractive Index	Resonance Coupling Wavelength (nm), λ_R		Intensity (dB)	
		Grating 1	*Grating 2*	*Grating 1*	*Grating 2*
Air	1.00 [28]	1569.37	1588.34	-32.43	-37.15
Ultrapure Water	1.33 [28]	1547.85	1566.17	-32.60	-43.51

Figure 3-6 shows the laser transmission spectra of the double-grating LPFGs in air and ultrapure water. The left reverse peak for each double grating system is Grating 1 (Λ = 525 μm) while the right reverse peak for each double grating is Grating 2 (Λ = 519 μm). This figure shows that the LPFGs resonance coupling wavelengths decrease, λ_R, when exposed to a material with an increasing refractive index.

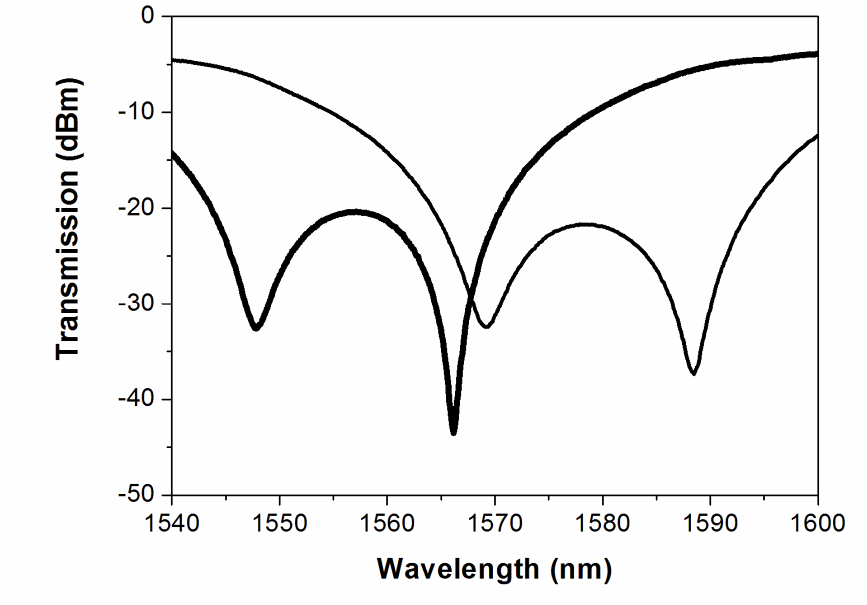

Figure 3-6. Verification of double grating functionality through immersion in solutions of varying refractive indices: air (light line) and water (heavy line).

It is known that the resonance coupling wavelength is related to the effective refractive indices of the core mode and a specific cladding mode order, $n_{eff,co}$ and $n_{eff,cl}$, as described in Equation 3.1 below [Erodgan, 1997] :

$$\lambda_R = \Lambda(n_{eff,co} - n_{eff,cl}) \tag{3.1}$$

where Λ is the grating period. For gratings of the same grating period, λ_R, decreases with decreasing $n_{eff,cl}$ because of the increase in the refractive index of the environment surrounding the fiber. For a given fiber with two gratings of different grating periods in the same environment, λ_R is determined by the grating period Λ, which is 519 μm and 525 μm for Grating 1 and Grating 2 for the double-grating system tested.

The primary purpose of the double-grating system is to establish that one grating can be used as a sensor to monitor a dynamic process and the other can be used to monitor any fluctuations in the environment, such as temperature or vibrations that would affect the sensor response. Therefore it is vital to show that the two gratings respond identically to any environmental changes. To verify this, two gratings in series (as shown in Figure 3-3) were immersed in two ultrapure water baths and the transmission spectrum was measured as a function time. The two baths were placed next to each other in an air-conditioned laboratory room, where the temperature drifted by 1–2 ^{o}C over the course of a day.

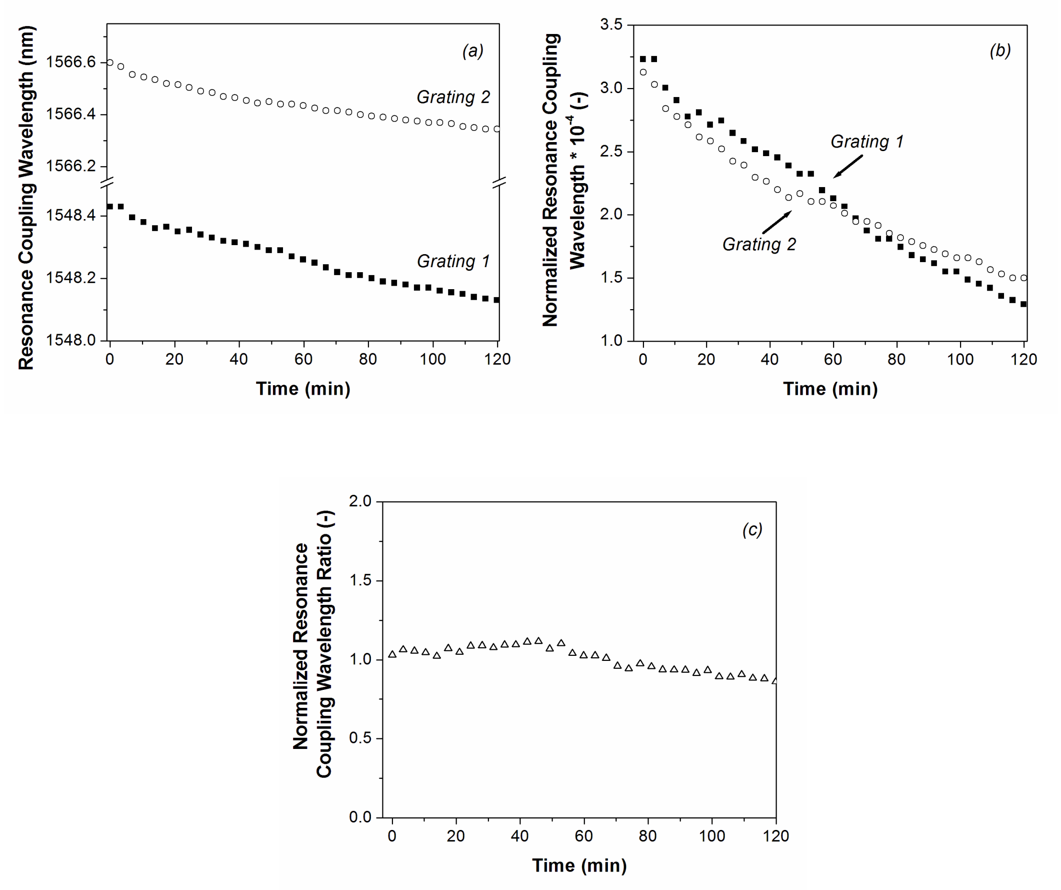

Figure 3-7. Resonance coupling wavelength shift behavior of two gratings in series each immersed in water to verify for behavior similarity: (a) Raw data (b) Normalized wavelength shifts, (c) Normalized wavelength ratio data hovering around unity.

Figure 3-7a (Grating 1 [Λ = 519 μm] and Grating 2 [Λ = 512 μm]) shows the resonance coupling wavelength of the two gratings in the water bath as a function of time. The resonance coupling wavelength for both gratings decreases with time due to the change in the room temperature. At a given time during the process, Equation 3.1 can be rewritten as:

$$\lambda_R(t) = \Lambda \cdot \Delta n_{eff}(t) \qquad (3.2)$$

with:

$$\Delta n_{eff}(t) = n_{eff,co} - n_{eff,cl}(t) \tag{3.3}$$

At the initial state of a dynamic process, Equation (3.2) applies to both gratings and it yields:

$$\lambda_{R,i}(0) = \Lambda_i \cdot \Delta n_{eff}(0) \tag{3.4}$$

where subscript $i = 1$ and $i = 2$ for Grating 1 and Grating 2, respectively. Note that $\Delta n_{eff}(0)$ is the same for Grating 1 and Grating 2 because both gratings are on the same fiber and in the same environment initially (same $n_{eff,cl}(0)$ and $n_{eff,co}$ for both gratings). Equation (3.2) also applies to Grating 1 and Grating 2 at a given time of the process:

$$\lambda_{R,i} = (t) = \Lambda_i \cdot \Delta n_{eff,i}(t) \tag{3.5}$$

Note that $\Delta n_{eff,i}(t)$ for Grating 1 is different from that for Grating 2 when Grating 1 is used as the sensor and Grating 2 as the reference. Combining Equations (3.4) and (3.5) to eliminate the grating period gives:

$$\frac{\lambda_{R,i}(t) - \lambda_{R,i}(0)}{\lambda_{R,i}(0)} = \frac{\Delta n_{eff,i}(t) - \Delta n_{eff}(0)}{\Delta n_{eff}(0)} \tag{3.6}$$

for both Grating 1 and Grating 2. When both gratings are exposed to the same environment (therefore the same dynamic process), $\Delta n_{eff,1}(t) = \Delta n_{eff,2}(t)$. Applying Equation (3.6) for both Grating 1 and Grating 2 yields:

$$\frac{\lambda_{R,1}(t) - \lambda_{R,1}(0)}{\lambda_{R,1}(0)} = \frac{\lambda_{R,2}(t) - \lambda_{R,2}(0)}{\lambda_{R,2}(0)} \tag{3.7}$$

Thus, the normalized change of the resonance coupling wavelength for Grating 1 should be the same as that for Grating 2.

Figure 3-7b plots the normalized coupling wavelength change for Grating 1 and Grating 2, from the data in Figure 3-7a. The two curves in Figure 3-7b have almost the same slope, indicating the compensation feasibility of the double-grating system by referencing one grating to another. The ratio of the two curves shown in Figure 3-7b is plotted in Figure 3-7c. This ratio hovers around unity throughout the 2 hour measurement period, which confirms that the behavior of each grating is similar throughout the entire experiment. It is worth noting that the drifts of the two gratings shown in Figure 3-7 may be caused by various contributions such as temperature variation, light source drift, and chemical composition change. However, the compensation should be adequate to the first order, especially when the range of variation is relatively small. These results suggest that the effect on the resonance coupling wavelength shift by environmental fluctuations experienced by a sensor grating (Grating 1) in a double grating system can be estimated from the response shown in a reference grating (Grating 2) by:

$$\Delta\lambda_{R,1}^{E}(t) = \lambda_{R,1}(0)\frac{\lambda_{R,2}(t) - \lambda_{R,2}(0)}{\lambda_{R,2}(0)} \qquad (3.8)$$

where $\Delta\lambda_{R,1}^{E}(t)$ is the resonance coupling wavelength shift in Grating 1 (sensor grating) which corresponds to the shift due to the environmental variations. If Grating 1 is used as the sensor to measure the dynamics of a particular process such as the lipid bilayer formation on the fiber surface, the corrected resonance coupling wavelength, $\lambda_{R,1}^{C}(t)$, can be obtained from the measured resonance coupling wavelength, $\lambda_{R,1}^{M}(t)$ by:

$$\lambda_{R,1}^{C}(t) = \lambda_{R,1}^{M}(t) - \Delta\lambda_{R,1}^{E}(t) \tag{3.9}$$

3.3.2. Detection of Lipid Bilayer Membrane Formation on Silica Fiber Surface

A double-grating LFPG was used to detect the lipid bilayer formation process on the silica fiber surface. Initially both gratings were placed in incubation cells each filled with Tris buffer solution. Before injection of the vesicle solution, the resonance coupling wavelength was measured for 6 minutes to verify system stability. Once confirmed, both the vesicle solution and blank buffer solution were simultaneously injected into the incubation cells for Grating 1 (sensor, Λ = 513 μm) and Grating 2 (reference, Λ = 524 μm), respectively, and the dynamic behavior of each grating was measured for 60 minutes. Figure 3-8 shows the resonance coupling wavelength shift for Grating 1 and Grating 2 as a function of time. At t = 0, $\lambda_R(0)$ = 1548.5 nm for Grating 1 and 1583.3 nm for Grating 2.

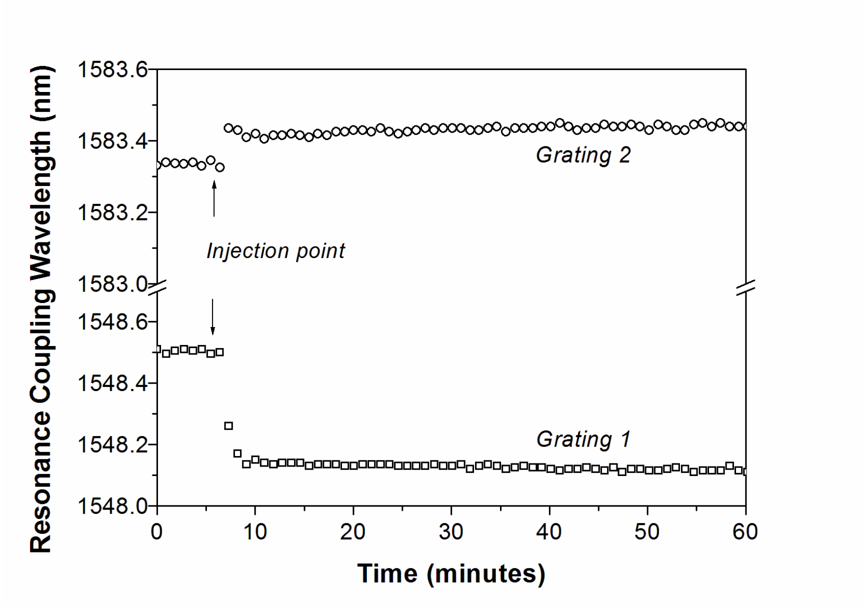

Figure 3-8. Resonance coupling wavelength shift of Grating 1 (sensor) and Grating 2 (reference) in response to the formation of a lipid bilayer membrane on the Grating 1 surface.

The injection points induced liquid circulation in each incubation cell, causing an 85 pm increase in the resonance coupling wavelength, as shown in the response for the reference Grating 2. The injection of solution induces a positive shift in the response for the sensor Grating 1, but this effect is overshadowed by the greater negative shift caused by the formation of lipid film formation on the silica fiber surface of Grating 1.

In order to correct for the environmental effects and liquid injection, the corrected resonance coupling wavelength for the sensor Grating 1 is calculated from the measured resonance coupling wavelength for Grating 1, $\lambda_{R,1}^{M}(t)$, and the measured resonance coupling wavelength for the reference grating, Grating 2, by the following equation combining Equation 3.8 and Equation 3.9:

$$\Delta\lambda_{R,1}^{E}(t) = \lambda_{R,1}^{M}(t) - \lambda_{R,1}(0)\frac{\lambda_{R,2}(t) - \lambda_{R,2}(0)}{\lambda_{R,2}(0)} \tag{3.10}$$

The corrected resonance coupling wavelength for the sensor Grating 1 showing the effect of the lipid bilayer formation is given in Figure 3-9.

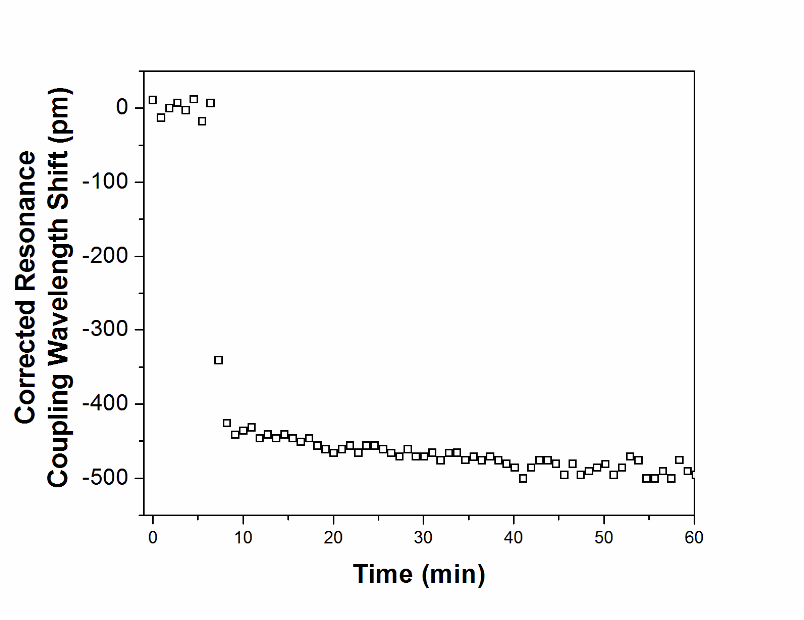

Figure 3-9. Corrected resonance coupling wavelength shift verifying the formation of a lipid bilayer membrane on the surface of Grating 2 with a lipid concentration of 0.1 mg.mL^{-1}.

The resonance coupling wavelength exhibits a rapid decrease in the first 3 minutes, followed by a slow decrease over 60 minutes, with an overall resonance wavelength shift of -500 pm. This wavelength shift is due to formation of a lipid bilayer on the fiber surface, as explained in Chapters 1 & 2. Reimhult et al. [Reimhult, 2006] found that a single supported lipid bilayer membrane was formed after 400 seconds using a vesicle solution concentration of 0.1 mg/mL. The formation time measured using QCM/SPR and the time measured by LPFG differ by 220 seconds. This can be attributed to the differences between vesicle diameters used. The exponential decaying formation rate can be attributed to the continued deposition of biomolecules on the membrane surface due to the presence of surface forces from the solid oxide support, though their presence is minimized.

In Chapter 2 the formation process on SiO_2 was measured on a planar surface using the QCM (Figure 2-7a); a bilayer formation time of approximately 20 minutes was observed. In Chapter 3, the formation process on a cylindrical support was measured using LPFG refractometry (Figure 3-9); a bilayer formation time of approximately 3 minutes was observed. The formation time differences between the two supports can be explained by their surface roughness properties. AFM measurements determined that the surface roughness (RMS) for the planar surface and fiber surface were 6 nm and 0.5 nm, respectively. As discussed in Section 2.3.4.1, differences in the support surface roughness properties will alter the available surface area thus changing the time required to form a bilayer membrane (increased time due to increased amount of vesicles/lipid required for bilayer formation). Thus, a surface roughness increase will proportionally increase the formation time required to form a continuous lipid bilayer membrane (assuming a smooth surface without jagged surface features, similar to the zeolite surface). The 10-fold increase of the RMS surface roughness on the planar support explains the nearly 10-fold increase in the formation time required for a lipid bilayer membrane. Therefore, the formation results on SiO_2 measured on the planar surface and fiber surface in this work at consistent.

The effect of the presence of Gramicidin on the formation process of an eggPC lipid bilayer on a silica fiber surface was studied using the double grating LPFG technique. This was done by using two 0.4 $mg.mL^{-1}$ eggPC solutions: one with a 0.1 $mg.mL^{-1}$ Gramicidin concentration and one without the presence of Gramicidin. Each solution was prepared as previously described and the thin film formation for each solution was monitored using the double grating LPFG system, as shown in Figure 3-10. The gratings used for these tests were as follows: with Gramicidin [$\Lambda_{1,2}$ = 515 μm (sensor), 524 μm (reference)] and without Gramicidin [$\Lambda_{1,2}$ = 516 μm (sensor), 522 μm (reference)].

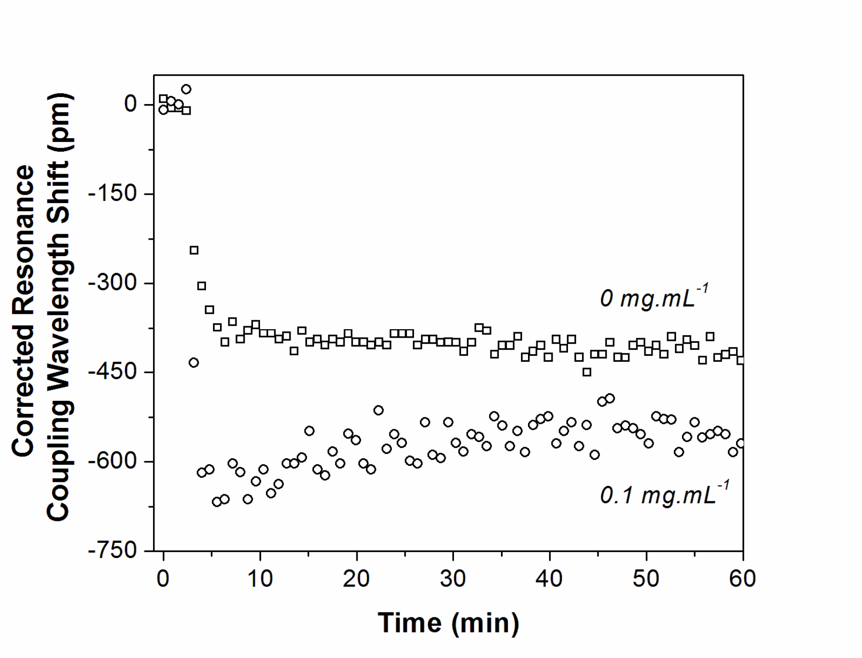

Figure 3-10. Corrected resonance coupling wavelength shift for the formation of a SLBM with a lipid concentration of 0.4 $mg.mL^{-1}$ with and without Gramicidin at concentrations 0.1 $mg.mL^{-1}$.

Figure 3-10 shows that the resonance coupling wavelength rapidly decreases and exponentially decays indicating vesicle adsorption and rupture on the support surface for an eggPC concentration of 0.4 mg.mL^{-1} and a Gramicidin concentration of 0 mg.mL^{-1}, similar to the results shown in Figure 3-8. The Gramicidin-incorporated lipid bilayer experienced a rapid resonance coupling wavelength shift of $\Delta\lambda_R$ = -625 pm. As supported by the data, the initial change occurred in approximately 3 minutes (amount of time required to reach 90% final value), similar to that for the Gramicidin-free lipid bilayer membrane. The rapid decrease in the resonance coupling wavelength shift was followed by a 65 pm shift increase, eventually stabilizing with a total wavelength shift $\Delta\lambda_R$ = -560 pm.

Ganeli et al. [Ganeli et al., 2003] found that the incorporation of Gramicidin into the lipid domain increases a vesicle diameter due to an increase in the number of total molecules per vesicle and the inclusion of water exposed domains of the Gramicidin molecule, thus increasing the vesicle's hydrodynamic radius. Previous work suggests that there is a coupling effect present between Gramicidin proteins and a support surface thus promoting strong surface-protein interactions [Lei et al., 2006]. The inclusion of the Gramicidin in the vesicles as well as the increased vesicle-surface interaction would result in a denser supported film (due to the presence of additional molecules) with a higher thin film refractive index. Thus, a higher resonance coupling wavelength shift is observed for the Gramicidin-containing bilayer membranes when compared to the Gramicidin-free system (as shown in Figure 3-10). Ganeli [Ganeli et al., 2003] found that the presence of Gramicidin in a lipid bilayer system does not significantly affect the kinetic formation process; therefore the kinetic formation rate of the Gramicidin-containing lipid bilayer membrane would be similar to the pure lipid system, as is seen in this work. The slow increase in the resonance wavelength after the initial 3 minute drop may be attributed to readjustment of the structure of the dense Gramicidin-containing lipid bilayer membrane to adopt the final stable structure.

It is believed that the phenomena observed with the Gramicidin-containing lipid bilayer membrane formation process is due to the formation of a single (yet denser) membrane system as opposed to a multi-layer system because of the formation kinetics shown in Figure 3-10. A denser lipid bilayer system response would result in a greater resonance coupling wavelength shift (when compared to the formation of a single lipid bilayer membrane system); a multi-layer system response would show either multiple shifts or a large continuous decrease in the resonance coupling wavelengths indicating multiple layers are formed. Neither of these trends was observed in this work, negating the conclusion of a dense lipid bilayer system or a multilayer system. Instead, a slow decrease was observed in this work, indicating that a single yet dense lipid bilayer was formed.

3.4. Conclusions

The formation of a supported lipid bilayer membrane (SLBM) on a silica fiber was examined using the long period fiber grating (LPFG) – based refractometry technique. A double-grating system was utilized to minimize the environmental influences for more reliable sensor data. Experiments were conducted to confirm the compensation capability of the double-grating system for quantitative study of the processes; it was found that the two LPFGs did not compensate for 100% of all environmental influences because they were in separate measurement cells yet it was sufficient for this application. The data of the resonance coupling wavelength shift show that the formation of a lipid bilayer on the silica optical fiber surface occurs in the first 3 minutes. The measurements also indicate that a multi-phase lipid bilayer system could be formed on the fiber surface during a 60 minute in-situ measurement. The lipid bilayer membrane system continuously deposited biomaterials on the grating surface throughout the entire 60 minute measurement period to yield a -500 picometer shift in the resonance coupling wavelength of the sensing LPFG. Incorporation of Gramicidin into the eggPC vesicles does not affect the formation rate of lipid bilayer membranes on the silica fiber; however, it was found that Gramicidin incorporation into the lipid bilayer membranes causes a greater decrease in the resonance coupling wavelength than a pure eggPC membrane because of the increased refractive index for the Gramicidin-containing eggPC lipid bilayer membrane.

Chapter 4

LATERAL FLUIDITY OF LIPID BILAYER MEMBRANES SUPPORTED ON A SILICA OPTICAL FIBER

4.1. Introduction

As discussed in Chapter 1, the most commonly used method to evaluate the continuity and quality of a lipid bilayer membrane is fluorescence microscopy. Epifluorescence microscopy is a technique that measures the intensity of emitted light from the supported lipid bilayer membrane (either via auto-fluorescent lipids or fluorescently tagged lipids) and is typically used to characterize membrane continuity. A continuous membrane is measured by uniform image fluorescence, while membrane defects are detected by a fluorescence void within the image. The quality of a lipid bilayer membrane is typically measured by its diffusion properties. One of the most frequently utilized techniques for evaluating membrane diffusion is fluorescence recovery after photobleaching (FRAP) [Richter et al., 2006].

Axelrod et al. [1976] were the first group to pioneer the characterization of membrane diffusion via FRAP analysis. This technique involves bleaching a small membrane area with a high-intensity laser beam to remove the fluorescent properties within that bleached region. The fluorescence recovery within the bleached area is dynamically measured and the diffusion coefficient can be extracted from the fluorescence recovery data using mathematical models. Axelrod et al. derived mathematical relationships describing the transport of lipid membranes and verified the theoretical work using experimental results. Assuming an infinite fluorescent sink and a small bleaching area (compared to the entire membrane area), the authors found that the diffusion coefficient can be estimated using Equation 4.1:

$$D = \left(\frac{w^2}{4t_{1/2}} \right) \tag{4.1}$$

Where D = diffusion coefficient (cm^2/s or μm^2/s), w = bleaching radius (cm or μm), $t_{1/2}$ = time (s) required to recover half of the fluorescent intensity (obtained from the fluorescent recovery after bleach curves). Equation 4.1 provides an efficient method for estimating the diffusion coefficient of a lipid membrane supported on a planar surface and allows for direct comparison of various lipid bilayer membrane systems.

The majority of the studies have employed planar SiO_2 materials as supports for lipid bilayer membranes. Using the relationship developed by Axelrod et al., Baksh et al. [2004] determined that the typical diffusion coefficients of model fluid membranes on SiO_2 supports range from 1 to 5μm^2/s [Baksh et al., 2004]. A few studies have been conducted to evaluate lipid bilayer membranes on the surface of SiO_2 beads. Buranda et al. [2003] determined through FRAP analysis that the behavior of a spherically supported lipid bilayer membrane (10 μm bead diameter) was comparable to a planar supported lipid bilayer membrane.

While planar and spherically supported lipid bilayer membranes have been studied, cylindrically supported membranes have yet to be fully characterized for their usefulness in applications such as fiber based biosensing. Chapter 3 detailed the first study examining the formation mechanism of a lipid bilayer membrane on a cylindrical fibrous support; it was found that the formation mechanism was similar to surfaces of identical surface chemistry and roughness measured with other acoustic techniques (i.e. QCM). However, the quality of the final membrane structure must be examined in order to directly compare membranes supported on various macroscopic geometries.

Axelrod et al. [1976] and subsequent groups (for example, Weng et al., 2004) have examined the diffusion behavior of a lipid bilayer membrane in a planar configuration. Planar supports offer the unique property that the entire surface studied can be viewed in one fluorescence image. However, due to the three dimensionality of the fibrous support, the entire fiber supported lipid bilayer membrane cannot be examined in a single image. This limits the ability to accurately measure the diffusion coefficient of the system because the entire bleached region (circular region) cannot be fully measured. Therefore, alternate bleaching configurations must be explored in order to accurately characterize the cylindrically supported lipid bilayer membrane. Additionally, a new theoretical model must be derived in order to accurately measure the diffusion coefficient with the new bleaching configuration.

This chapter will address the current limitations of characterizing the transport behavior of cylindrically supported lipid bilayer membranes. A new mathematical model incorporating a novel bleaching configuration will be explored. Additionally, experimental FRAP results will be examined using the novel theoretical model in an effort to characterize fibrous supported lipid bilayer membranes.

4.2. Experimental Methods

Materials used within this dissertation were consistent throughout all experiments. Vesicle synthesis was completed as detailed in Chapter 2.2.1. The buffer pH was maintained at pH = 8.

4.2.1. Lipid Bilayer Support Preparation and Surface Characterization

Within this study, the support used was a pure silica optical fiber (Corning SMF-28) with a 125μm outer diameter. The surface was successively cleaned in isopropanol and ultrapure water for 60 minutes each via low-power sonication (Cole-Parmer bath sonicator, model 8890). The surface was immediately submerged in ultrapure water to minimize surface contamination during exposure to the ambient air.

Scanning electron microscopy (SEM, Philips XL30) micrographs and atomic force microscopy (AFM, Digital Instruments Nanoscope III Multimode) topographical images of the fiber surface were collected to verify the smoothness and the absence of foreign materials on the fiber surface following polymer removal and successive sonication treatments. A representative SEM micrograph of the fiber surface is shown in Figure 3-1. No surface scratches or any foreign material were observed at high magnification (SEM, 7000X, data not shown) and possessed a surface roughness of 5Å (AFM, 1μm x 1μm, Figure 4-1). These results verify fiber surface continuity following surface preparation.

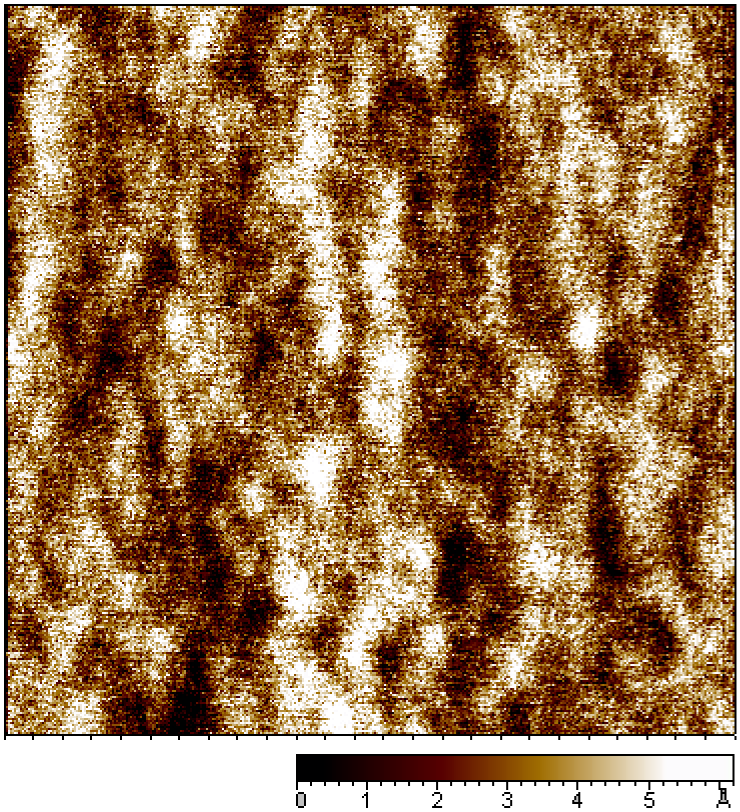

Figure 4-1. AFM measurements of the fiber surface (1x1 μm).

4.2.2. Confocal Microscopy Measurements

Following fiber cleaning, the fiber was secured in an incubation cell and incubated within a concentrated lipid bulk solution for 1–2 hours to ensure adequate lipid bilayer deposition on the fiber surface. After incubation, the fiber was carefully rinsed using excess Tris buffer to remove unbound vesicles from the fiber surface and surrounding solution. The fiber was placed in a culture well (35mm glass-bottomed Petri dish with 20mm microwell, Mastek Corporation), to facilitate fluorescence measurements. Measurements were collected using a Zeiss

LSM DUO 510 confocal microscope (40x Plan-Neofluar, NA 1.3 oil immersion objective, Argon ion laser at 488nm, tube current of 6W). Once placed into a culture well fluorescence microscopy measurements and fluorescence recovery after photobleaching (FRAP) studies were performed to verify both the presence of a lipid bilayer membrane and to measure its mobility on the support surface. Bleaching was done as outlined in Figure 4-2. Figure 4-2a is a schematic of the fiber system indicating fiber orientation and associated axes with the grey stripe indicating the bleaching location and configuration on the fiber surface. Figure 4-2b shows photobleaching technique used throughout this study (bleaching shown by hatched rectangle) and it is assumed constant in both experimental and modeling studies (scale bar measures 50μm. Figure 4-2c is a schematic of bleached area on fiber and method of analysis, with the grey arrows indicating fluorescent directional flow from infinite fluorescent sinks.

The focal points for the confocal microscope were positioned at discrete theta locations (θ_n, see Figure 4-2a) using a constant xy plane (microscope axes) to collect information on the lipid bilayer membrane at different locations.

Bleaching was conducted and the dynamic fluorescence recovery within the bleached regions was measured. Bleaching was carried out in the configuration demonstrated in Figure 4-2b. The bleaching configuration and position were held constant throughout all experiments while the theta positions were varied. Because the bleaching location remained constant throughout experiments, it is vital that the system reached steady state prior to a subsequent bleaching experiment was performed. Thus, the system was allowed to reach steady state for at least 20 minutes between runs. Experiments were performed sequentially either from $\theta_{low \rightarrow high}$ or $\theta_{high \rightarrow low}$. The observed behavior remained constant regardless of run order.

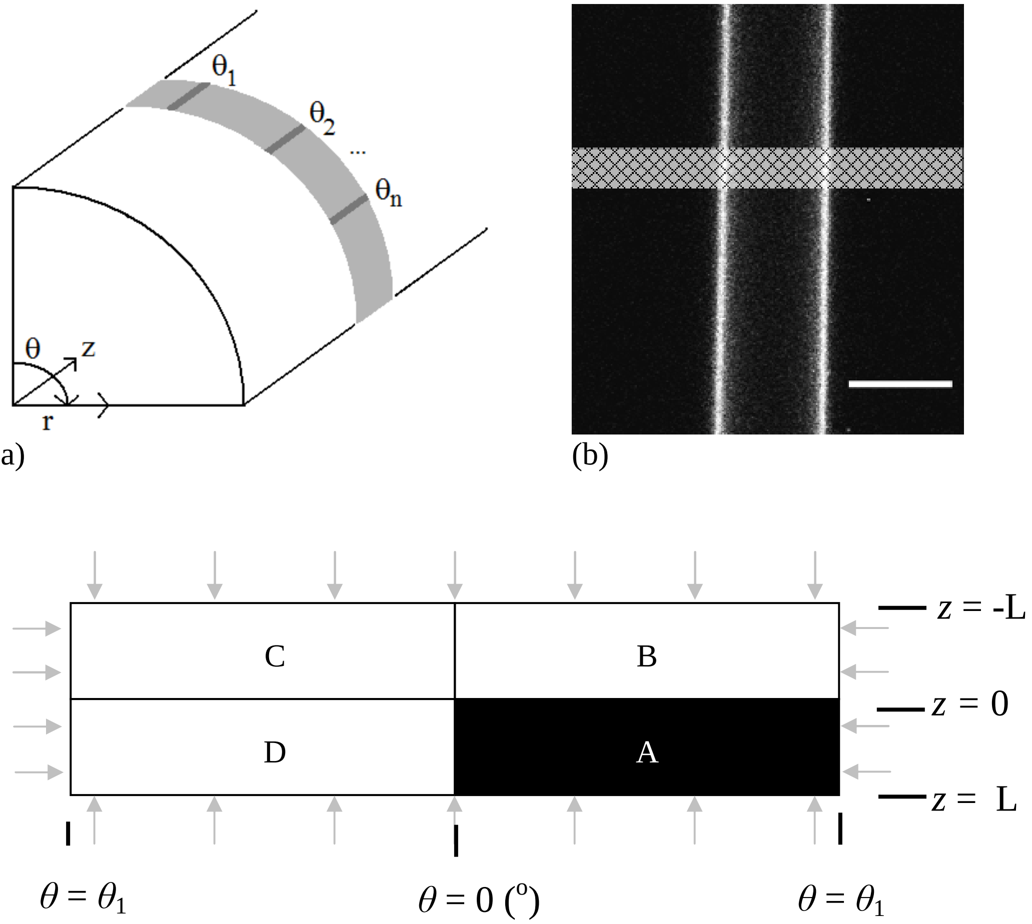

(a)

(b)

(c)

Figure 4-2. Schematic of the bleaching configuration within this study with (a) indicating fiber orientation, (b) photobleaching technique, and (c) recovery area.

The fluorescence recovery data was normalized and calculated using Equation (4.2) to allow for direction comparison between runs.

$$F_{norm} = \frac{F(t) - F(0)}{F(\infty) - F(0)} \tag{4.2}$$

where F_{norm} = normalized fluorescence intensity, F(t) = dynamic measured fluorescence intensity, F(0) = fluorescent intensity at bleaching, and $F(\infty)$ = steady state florescent intensity. Experiments were conducted assuming an infinite lipid reservoir and short bleaching time. Normalized fluorescence recovery curves were analyzed by a two-dimensional diffusion model described next to obtain diffusivity coefficients. Standard error in FRAP experiments was 5%.

4.3. Theoretical modeling for diffusion in a cylindrical geometry

Axelrod et al. [Axelrod et al., 1976] were the first to report a mathematical model describing the diffusion of biological membranes upon photobleaching on planar support assuming a circular beam profile and an infinite sink of fluorescent material. This approach was followed by many other researchers [Richter et al., 2003; Johnson, et al., 2002; Knoll, 1998; Richter et al., 2006; Hennesthal et al., 2000; Lu et al., 1996; Uto et al., 1994; Sackmann & Tanaka, 2000; Tanaka & Sackmann, 2005; Weng et al., 2004] to evaluate the diffusivity of biological membranes on planar supports. However, these planar models cannot be applied to the diffusion of lipid membranes supported on cylindrical geometry.

Bleaching on the lipid bilayer on the silica fiber (125 μm diameter in this work) and the diffusion of unbleached lipid molecules into the bleached area can be illustrated in Figure 4-2. In the present work the bleaching was conducted across the fiber width with dimensions of $-90 < \theta_n < 90^{\circ}$ and $-10 < z < 10$ μm, as shown in Figure 4-2b. The bleached area can be converted to a rectangle in the planar geometry as shown in Figure 4-2c. The area beyond the four sides of the rectangle can be considered as the infinite fluorescent sinks and the unbleached lipid molecules diffuse two dimensionally into the bleached area. The diffusion of unbleached lipid molecules (designated as A) in the lipid bilayer membrane can be modeled using the continuity equation for species A [Bird et al., 2007]:

$$\rho\left(\frac{\partial \omega_A}{\partial t} + v_r \frac{\partial \omega_A}{\partial r} + \frac{v_\theta}{r}\frac{\partial \omega_A}{\partial \theta} + v_z \frac{\partial \omega_A}{\partial z}\right) = \rho D_{AB}\left[\frac{1}{r}\frac{\partial}{\partial r}\left(r\frac{\partial \omega_A}{\partial r}\right) + \frac{1}{r^2}\frac{\partial^2 \omega_A}{\partial \theta^2} + \frac{\partial^2 \omega_A}{\partial z^2}\right]$$

(4.3)

where ρ = density, ω_A = mass of species A, D_{AB} = diffusion coefficient of unbleached molecule A into bleached molecule B. It can be assumed that the diffusion coefficient, D_{AB}, remains constant over the experimental time scale and the membrane maintains a constant density.

Because there is no bulk fluid velocity in the lipid membrane, $v_r = v_\theta = v_z = 0$. Additionally, there is no radial diffusion and upon conversion from a mass to a mole basis, yielding $c_A = c_A(\theta, z)$. Upon application of the above assumptions and non-dimensionalizing Equation (4.3) using:

$$\phi = \frac{c_A}{c_{A_o}} \tag{4.4}$$

$$\xi = \frac{z}{L} \tag{4.5}$$

Equation (2) is reduced to:

$$\frac{\partial \phi}{\partial t} = D_{AB}\left(\frac{1}{R^2}\frac{\partial^2 \phi}{\partial \theta^2} + \frac{1}{L^2}\frac{\partial^2 \phi}{\partial \xi^2}\right) \tag{4.6}$$

where C_{Ao} is the concentration of lipid molecules in the sink, L is length of bleaching area, and R = radius of support fiber (R = 62.5μm for the fiber studied in this work).

The diffusion problem is defined by Equation (4.6) with the following initial and boundary conditions:

$$\phi = 0 \qquad \begin{cases} t = 0 \\ 0 < \theta < \theta_1 \\ 0 < \xi < 1 \end{cases} \tag{4.7}$$

$$\phi = 1 \qquad \begin{cases} \xi = 1 \\ 0 < \theta < \theta_1 \end{cases} \quad \text{, at any t>0} \tag{4.8}$$

$$\phi = 1 \qquad \begin{cases} 0 < \xi < 1 \\ \theta = \theta_1 \end{cases} \quad \text{, at any t>0} \tag{4.9}$$

$$\frac{\partial \phi}{\partial \xi} = 0 \qquad \begin{cases} \xi = 0 \\ 0 < \theta < \theta_1 \end{cases} \quad \text{, at any t>0} \tag{4.10}$$

$$\frac{\partial \phi}{\partial \theta} = 0 \qquad \begin{cases} 0 < \xi < 1 \\ \theta = 0^{\text{o}} \end{cases} \quad \text{, at any t>0} \tag{4.11}$$

The boundary conditions consider the diffusion behavior in area A shown in Figure 4-2c as the diffusion into the bleached rectangle is symmetrical in both dimensions.

A two-dimensional finite element method was used to find the numerical solution to the initial/boundary value problem given by the partial differential equation (4.6) together with the initial condition (4.7) and boundary conditions (4.8) - (4.11). The software ANSYS [ANSYS, 2004] was used to conduct the simulations with a discretization of the bleached area in the axial and circumferential directions. A mesh with the 3-D element (Shell57), which has in-plane diffusion conductivity capability, was used, with a finer structure at the boundaries and in regions with high diffusion gradients and coarser elements in parts with little concentration variation. The element Shell57 is the 4-node finite element with one degree of freedom, concentration, at each node.

4.4. Results and Discussion

4.4.1. Confocal Microscopy Measurements

In confocal microscopy, each specimen is profiled through a collection of optical slices to allow for greater resolution of the sample and to negate the “stacking” phenomena that prevents high resolution of the inner portions of the sample. The optical slices can be focused to image various sample depths and locations on the specimen surface by adjusting microscope parameters (such as the numerical aperture), or adjusting the microscope axis, respectively. Each individual optical slice is a two-dimensional projection of the three dimensional object. These individual slices can be correlated to exact locations on the specimen only if the optical slice depth and information about the specimen geometry is known.

In the present work, a cylindrical silica optical fiber with a 125 μm diameter was used as the support to a lipid bilayer membrane. A lipid bilayer membrane supported with a planar support can be completely imaged in a single x-y plane (microscope plane) due to the planar topography of the support surface; essentially, the entire surface can effectively "fit" inside of a single optical slice. Contrary to the study of a planar support system, the three dimensional optical fiber support must be observed through the study of a series two dimensional optical slices. Within this work, the various optical depths, in increments of 1μm, were studied to isolate the behavior of the lipid bilayer membrane at discrete θ_n values.

Each optical slice of a fiber supported lipid bilayer membrane captures only a small portion of the fiber and consequently the supported lipid bilayer is represented by two parallel lines; each set of parallel lines represent the lipid bilayer membrane at discrete locations on the fiber surface. The distance between the two parallel lines varies with the location on the fiber being imaged, r_n, as shown in Figure 4-3. As the theta position is varied, the separation distance of the parallel lines likewise fluctuates. The distance between the two parallel lines increases with increasing θ_n. After geometric manipulation, the exact position shown on the fiber is represented by θ_n, where $\theta = 0^o$ is at the vertical axis and is located at the fiber's center ($r_n = 0$). The translation of the two-dimensional representation, as shown in Figure 4-3a, to the three dimensional configuration experienced by the lipid bilayer system is illustrated in Figure 4-3b.

Figure 4-4 shows confocal images collected of a lipid bilayer membrane supported on the fiber. Based on the distance between the two parallel lines, the exact location on the fiber surface can be calculated. Various locations on the fiber were studied, sweeping from $\theta = 15^o$ to $\theta = 76^o$ in Figures 4-4a-f. This can be further characterized by analyzing the fluorescence intensity within a constant line scan of each image in Figure 4-4. The results are given in Figure 4-5.

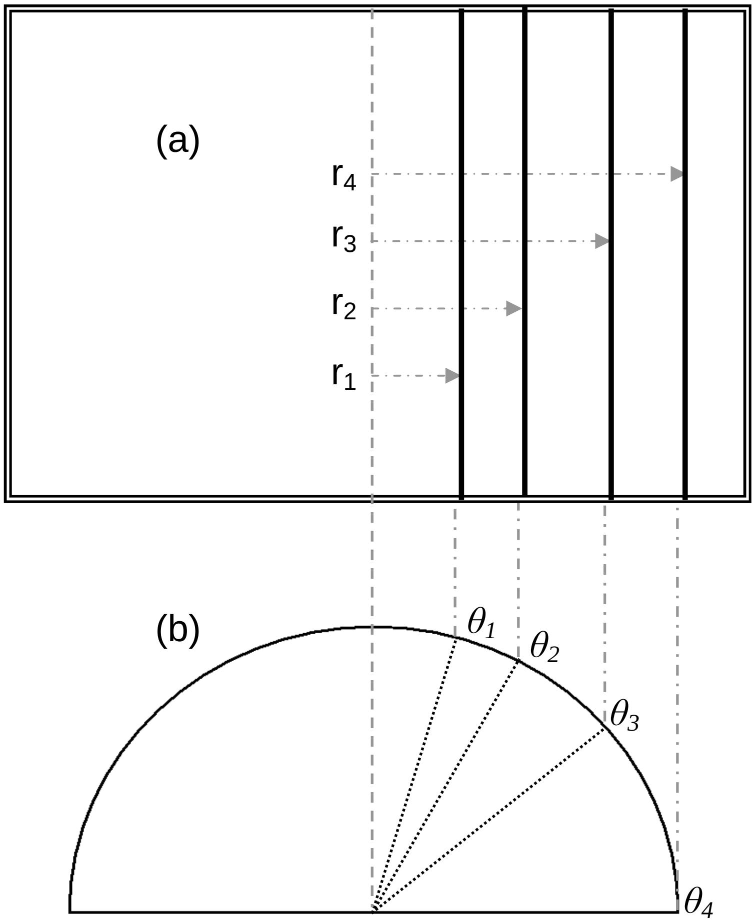

Figure 4-3. Translation of fluorescence images from a planar measurement plane (r_n) to cylindrical coordinates corresponding to its location on the fiber surface (θ_n).

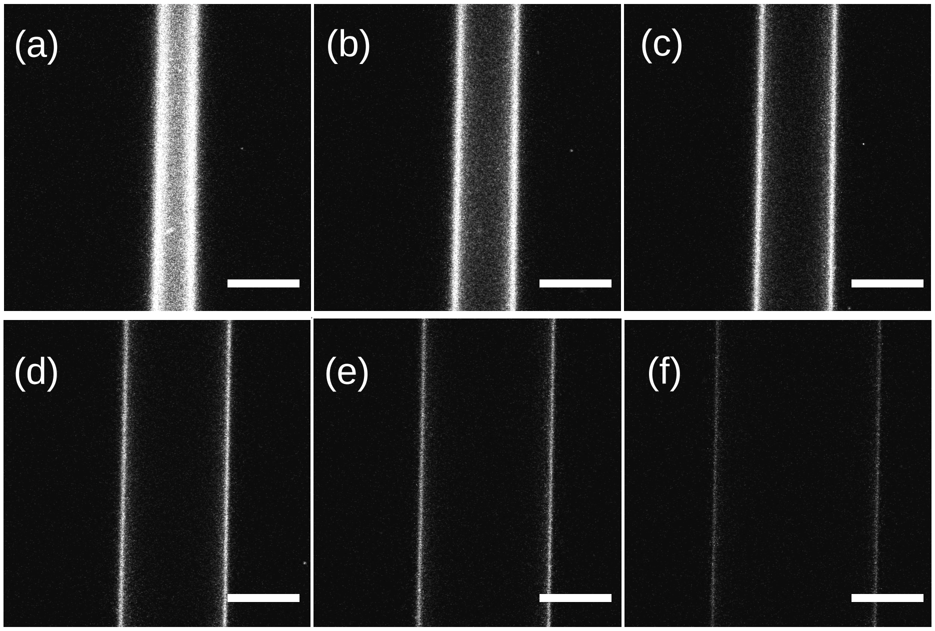

Figure 4-4. Confocal images of the lipid bilayer membrane on a fiber surface at different measurement positions: (a) 15º, (b) 21º, (c) 27º, (d) 39º, (e) 51º, and (f) 76º. Scale bar measures 50µm.

It is clear that the distance between the two parallel lines increases and the maximum fluorescence intensity decrease with increasing theta value. The fluorescence intensity is directly related to the distance between the microscope objective lens and the sampling location. At $\theta = 0^o$, there is a minimum separation distance between the sample and the objective lens; thus, the measured fluorescence intensity is the intensity emitted from the lipid bilayer membrane. As the theta increases, the working distance between the objective lens and the sampling location increases, thus allowing a lower percentage of the emitted fluorescence to reach the objective lens.

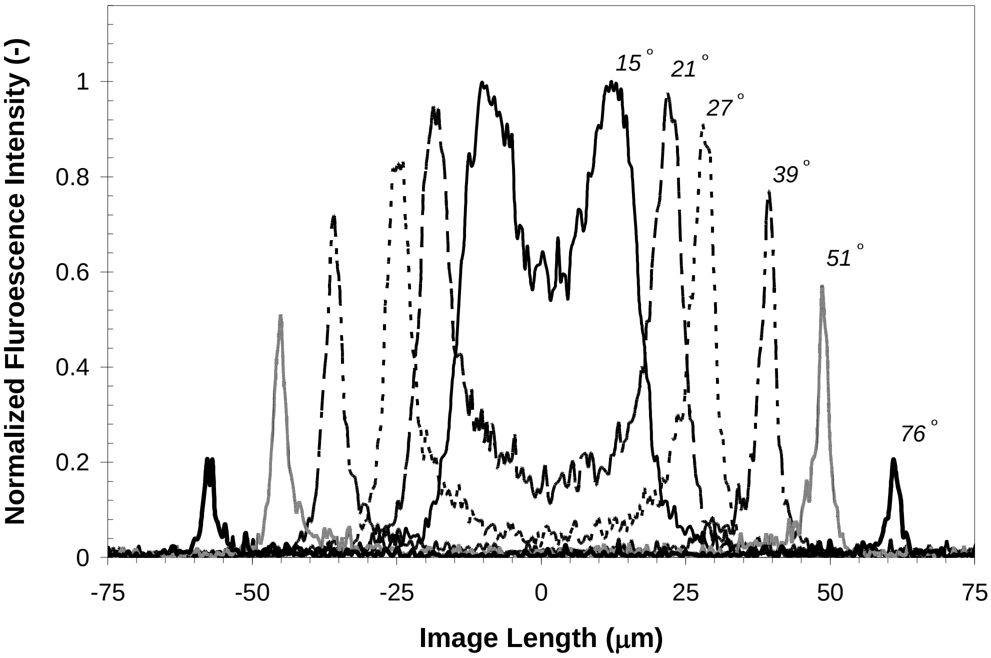

Figure 4-5. Line scans of fluorescent images of a fiber supported lipid bilayer membrane at various measurement positions (θ_n) on the fiber. The center of the fiber is designated at 0 μm and 0^o.

To determine lipid fluidity, the fluorescence intensity at a given θ_n location was measured as a function of time. Although the measured fluorescence intensity before bleaching varies from the θ_n location, as shown in Figure 4-5, it is the normalized transient fluorescence curve that determines measurement of the fluidity of the lipid molecules. The transient fluorescence recovery curves can be obtained from the solution of the mathematical model described in Equation (4.2).

4.4.2. Modeling Results and Analysis of Membrane Diffusion

Figure 4-6 shows numerical solutions of transient dimensionless concentration profiles for the species A in the bleached area of $0 < \theta < 45°$ and

$0 < z < 15$ μm with diffusion coefficient of 2.1 $\mu m^2/s$. It is assumed that there are continuous fluorescent sinks along left and top edges and the bleached area center at the bottom and right.

Figures 4-6a-g show concentration increase from the edges of the rectangle into the center of the entire region (bottom-right corner). The normalized concentration of species A at the center versus time is shown in Figure 4-6h. It should be noted that the fluorescence intensity is proportional to the concentration of the species A; therefore the normalized fluorescence intensity is directly correlated to the dimensionless concentration of species A. As shown in Figure 4-6h, the fluorescence intensity approaches the equilibrium at time larger than 125s.

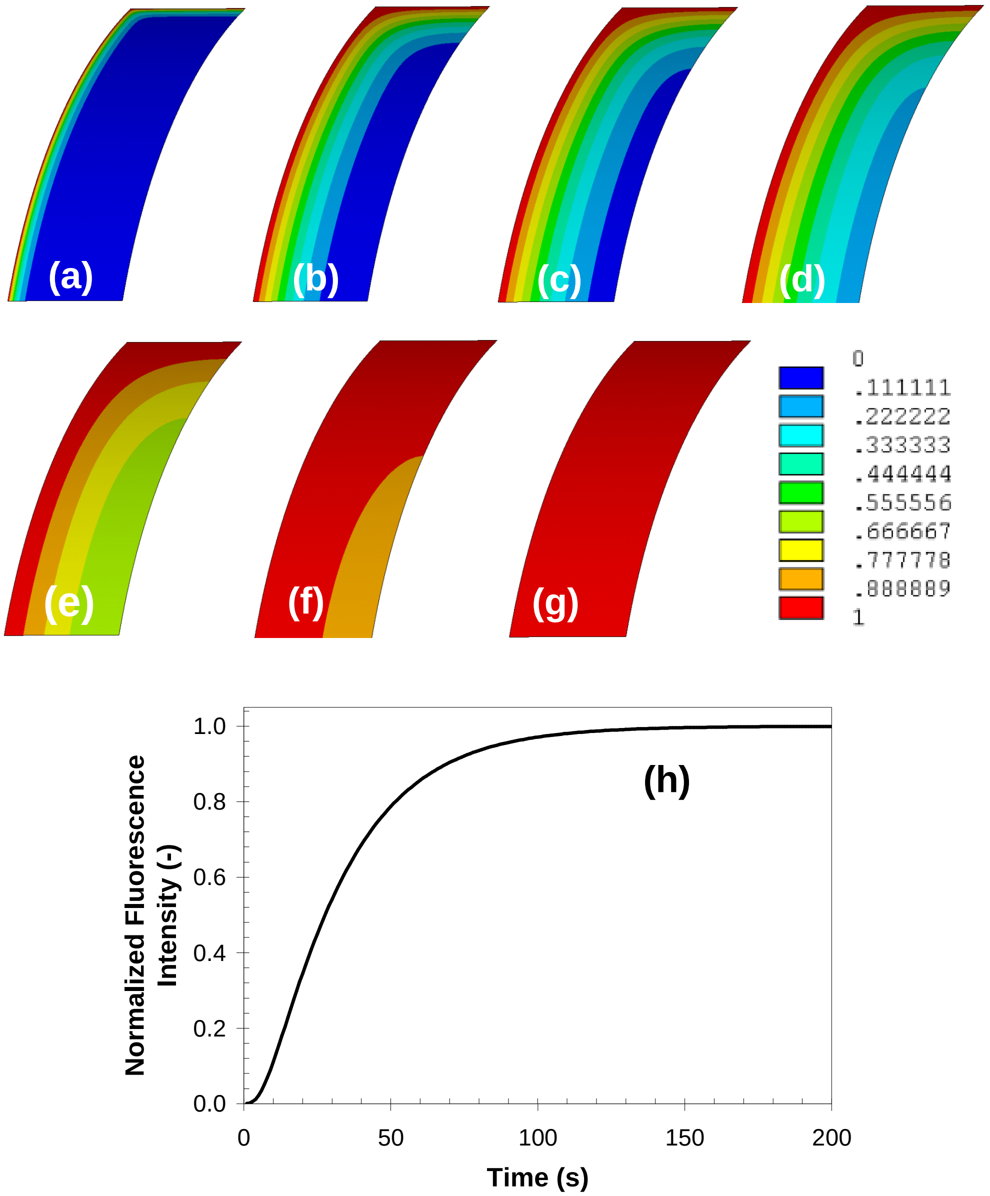

Figure 4-6. Simulated normalized lipid concentration in the bleached area on the surface of cylindrical support at time = (a) 1s, (b) 5s, (c) 25s, (d) 40s, (e) 100s, (f) 200s, (g) 250s, (h) FRAP recovery.

Figure 4-7 shows the normalized transient fluorescence curves for a constant diffusivity at different θ_n locations of the fiber.

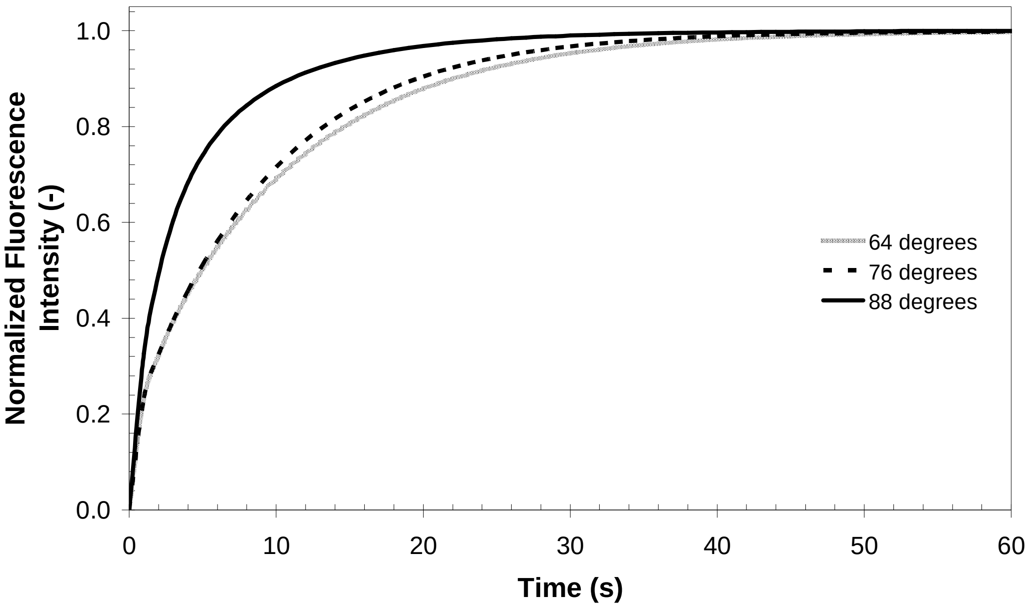

Figure 4-7. Normalized fluorescence intensity recovery curves at 64°, 76° and 88° with a constant diffusion coefficient, *D* = 1.0μm^2/s. Recovery curves for $\theta < 64°$ remains constant.

As shown in Figure 4-7, the fluorescence recovery rate is greatest near to the boundaries of the bleached area at $\theta = 88^o$, and the rate significantly decreases as the physical location shifts to $\theta = 76^o$ with a minor decrease in the modeled rate at $\theta = 64^o$. It is found that the recovery rate remains constant at $\theta < 64^o$ (data not shown).

This behavior can be explained by the two-dimensional diffusion of lipid bilayer molecules from the infinite fluorescent sinks into the bleached region. At $\theta = 90^o$, the lipid bilayer membrane experiences two directional diffusion from the z = 0 μm and $\theta = 90^o$ boundaries, where the contribution for fluorescence recovery is derived equally from both boundaries. As the θ_n decreases, the diffusion contribution from the $\theta = 90^o$ boundary decreases; therefore, the diffusion process transitions from a two directional dominated diffusion scheme to a one directional diffusion scheme. This trend is better explained by the two-dimensional simulation results shown in Figure 4-8 which give fluorescence recovery of a bleached region from (a) t = 1 s after bleach to full recovery at (f) t = 100s. The † designates a two-directional diffusion process while the * signifies a one-directional diffusion process. Color gradient corresponds to the concentration gradient as defined in Figure 4-6.

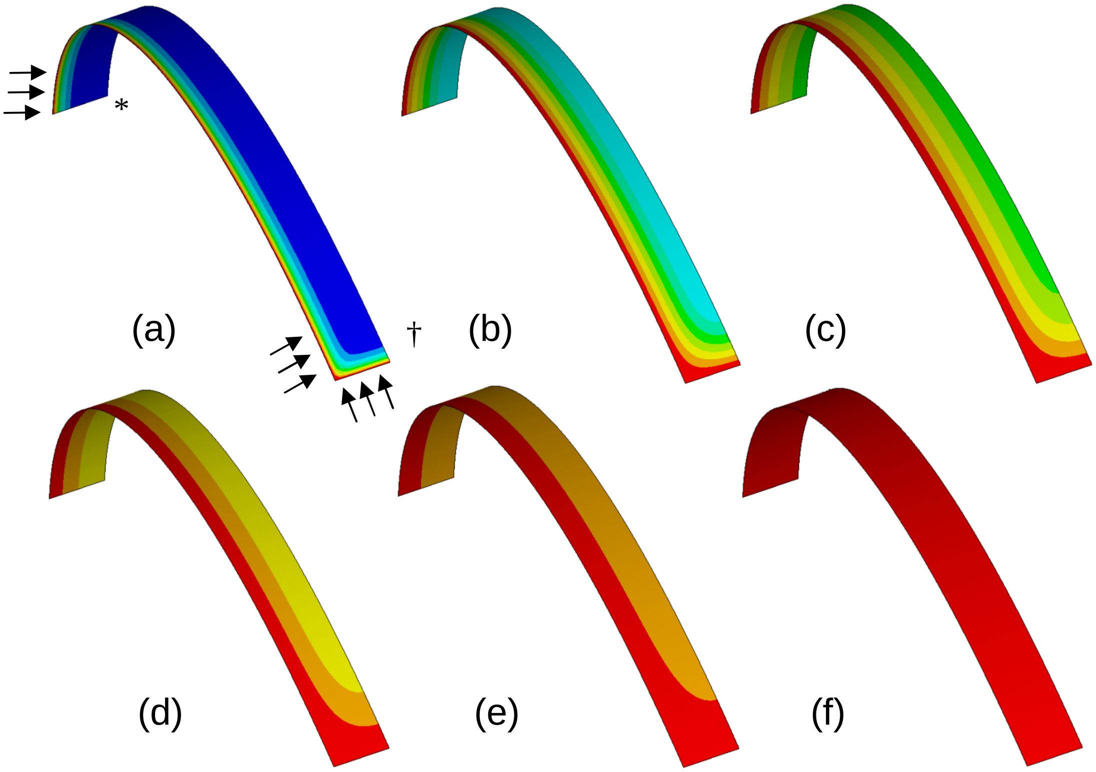

Figure 4-8. Fluorescence recovery with an area of $0 < z < 15\mu m$ by $0 < \theta < 90°$ at time = (a) 1s, (b) 10s, (c) 20s, (d) 30s, (e) 50s, (f) 100s.

The two-dimensional dominated regime seen within the region of interest is designated by a † in Figure 4-8a, while the one-dimensional dominated regime within the region of interest is designated by the * in Figure 4-8a; the included arrows further delineate between one- and two-diffusion dimensionality.

This one- vs. two-directional diffusion is important and must be considered when using the FRAP technique to quantitatively measure the fluidity of the bilayer membrane. Figure 4-9 shows the normalized fluorescence recovery curves at $\theta = 8^o$ for varying values of the membrane diffusivity coefficient using the two-dimensional model presented in this work.

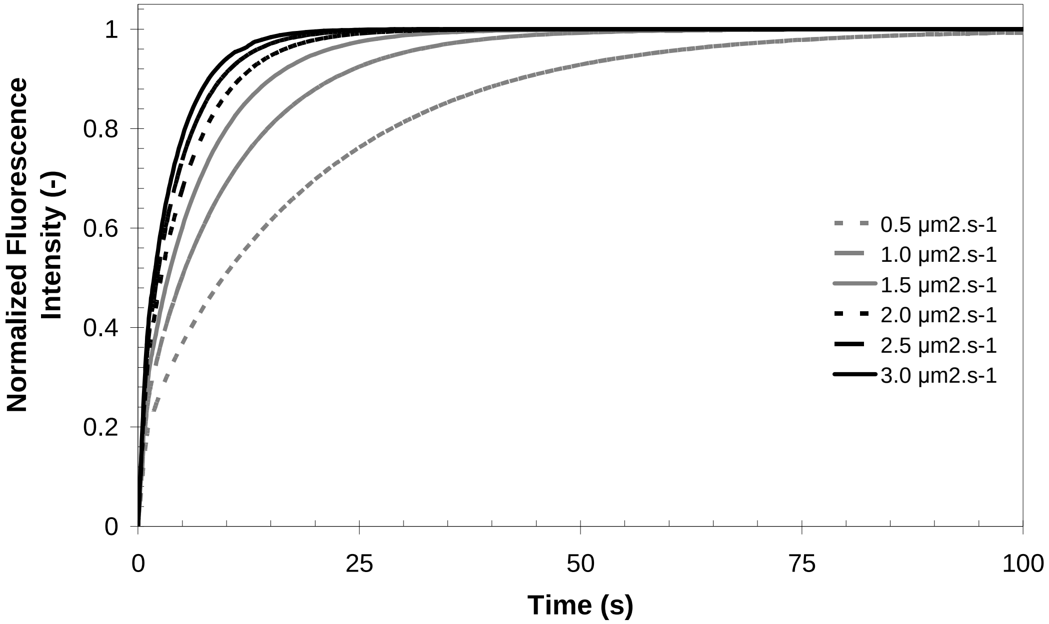

Figure 4-9. Normalized fluorescence intensity recovery as a function of diffusion coefficient at constant location (8°).

As shown in Figure 4-9, the recovery rate increases with increasing diffusivity coefficients. Recovery curves with differing values of membrane diffusivities can be obtained for various positions in the fiber. When using the model to fit the experimental data to obtain the diffusivity, it is critical that the two-dimensional diffusion model at the adequate position on the fiber is used in order to obtain reliable results. Unreliable results will stem from using wrong diffusion model, which will incorrectly determine the membrane behavior.

Figure 4-10 shows experimental transient florescence recovery curves of the lipid bilayer membrane on the silica optical fiber measured at $\theta = 12^o$ and at $\theta = 62^o$.

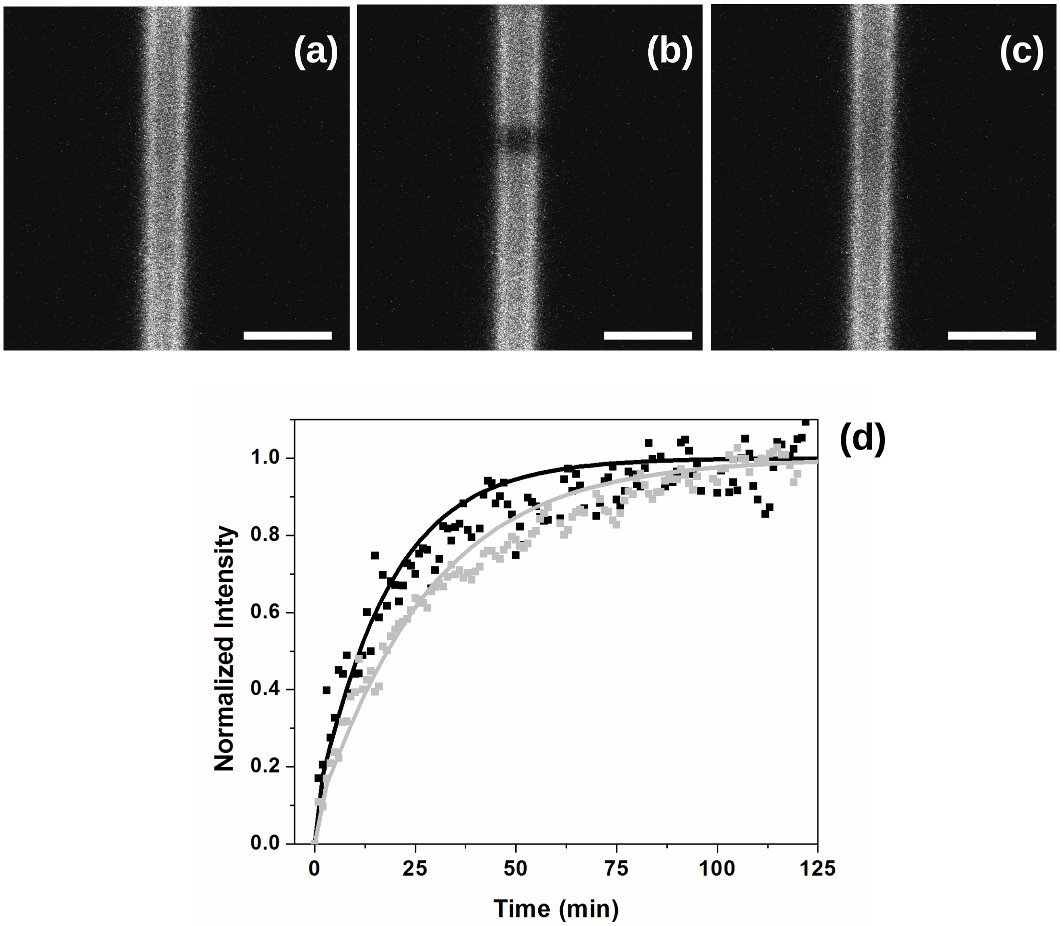

Figure 4-10. FRAP experiments at $\theta_n = 25°$ (a) before bleach, (b) just after bleach and (c) after 100s (full recovery). Solid white bar indicates 50µm. FRAP modeling at 62^o (black dots) and 12^o (grey dots) and their associated modeled behavior are found in (d). Diffusion coefficients for 62^o and 12^o were found to be 1.1 ± 0.2 µm^2/s and 0.78 ± 0.2 µm^2/s.

Figure 4-10 shows the fiber (a) before, (b) just after bleach, and (c) after full recovery [identical to (a)] for $\theta = 12^{o}$. These images verify the transient process and full recovery of the bleached area after bleaching. The same behavior was observed for $\theta = 62^{o}$. Figure 4-10d shows the normalized fluorescence intensity within the bleached region (experimental data shown by individual points, modeling results shown in bold lines). The experimental fluorescence recovery at each location shows full recovery at about 40 seconds. Simulation results for the normalized florescence intensity recovery curves were calculated for each position for the fiber using the model described in this work. The diffusivity coefficient was varied in order to accurately model the experimental results.

It found that upon comparison of the simulation results with the experimental data, the model data with a diffusion coefficient of 1.1 $\mu m^2/s^{-1} \underline{+} 0.2 \mu m^2/s^{-1}$ fits well the experimental data at $\theta = 62^{o}$. Likewise, the model data predicts a diffusivity coefficient of 0.78 $\mu m^2/s^{-1} \underline{+} 0.2 \mu m^2/s^{-1}$ for the lipid bilayer membrane measured at the position of $\theta = 12^{o}$ (Figure 4-10d). These diffusivity values are in agreement with Wagner and Tamm [Wagner & Tamm, 2000] who report diffusivity measurements of 2 wt% NBD-tagged eggPC membranes supported on a planar silica surface. While the two locations yield different calculated diffusion coefficients, the two calculated values are within the experimental range of error; therefore, the two coefficients can be considered the same experimentally. Continuous lipid bilayer membranes should maintain a similar diffusion coefficient across its entirety without barriers on the support surface since barriers have been shown to affect membrane diffusion [Cremer & Boxer, 1999]; this requirement is satisfied within this work. This would allow the one- vs. two- directional diffusion to dominate based on measurement location, thus affecting accurate diffusion coefficient calculations of membrane behavior with position. Therefore, while these results verify that the supported lipid membranes in this work are comparable to similar membranes previously reported, it is critical that the supporting geometry and its associated theoretical model describing the diffusion are considered when calculating the diffusivity coefficient. Failure to account for the support geometry could yield unreliable results which could affect subsequent experimental results and calculations.

4.5. Conclusions

The diffusion behavior of a lipid bilayer membrane supported by a cylindrical silica support was modeled using a two-dimensional unsteady state diffusion and studied experimentally using fluorescence recovery after photobleaching (FRAP). The diffusion model was solved numerically using the ANSYS software to obtain simulated fluorescence recovery curves at different positions on the fiber. Due to the cylindrical geometry of the support and limited optical depth of the confocal microscope during the FRAP analysis, fluorescence recovery curves vary significantly from the measurement positions on the fiber. Fluorescence recovery curves exhibit a slower rate as the measurement position moves from the edge to the center of the fiber due the transition of the diffusion process from two-dimensions to one dimension. The two-dimensional diffusion model at a given measurement position can be used to adequately describe the experimental fluorescence recovery curve. The diffusivity for the silica fiber supported eggPC lipid bilayer membrane was found to range from 0.78 $\mu m^2.s^{-1}$ ± 0.2 $\mu m^2.s^{-1}$ to 1.1 $\mu m^2.s^{-1}$ ± 0.2 $\mu m^2.s^{-1}$ depending on the position measured, which is comparable to membrane diffusivity results of eggPC lipid bilayer membranes formed on a planar silica supporting surface. This work improves the understanding of cylindrically supported lipid bilayer membranes and allows investigators to take this observed rate variation into consideration when designing novel systems for supported lipid bilayer technology in various arenas, such as biosensing and biorecognition.

Chapter 5

SUMMARY AND RECOMMENDATIONS

5.1. Summary

This research work focused on the fundamental study of the synthesis and characterization of lipid bilayer membranes on novel inorganic supports. Direct mass adsorption (using the QCM technique) was used to characterize the formation process of eggPC lipid bilayers on each porous support material. Several parameters were varied to determine their effects on the bilayer formation process. A novel optical sensing technique (long-period fiber grating) was utilized for studying the formation of lipid membranes on cylindrical supports. Experimental and theoretical examination of membrane transport behavior on cylindrical supports was also investigated.

The first objective of this work was to synthesize lipid bilayer membranes supported on porous inorganic thin films. In Chapter 2, the four types of inorganic thin films chosen for this work were zeolite (silicalite), γ-alumina, mesoporous zirconia (yttria stabilized zirconia, YSZ), and macroporous YSZ thin films. The films were prepared via the spincoating method and calcined at $400^{o}C$; the temperature was chosen to remain below the phase transition temperature of the QCM quartz to maintain crystal integrity. A variety of characterization techniques were employed to characterize the films to ensure that film structure was maintained at the lower calcination temperature.

Several parameters were examined in an effort to synthesize lipid bilayer membranes and to study their effects on adsorption properties. The first parameter studied was the effect of surface chemistry on the lipid bilayer formation process Surface chemistry studies found that the vesicle adsorption process yielded a lipid bilayer membrane structure on SiO_2 and a vesicle monolayer on γ-alumina. This can be explained by a differing oxide structure between the two materials (SiO_2 vs. Al_2O_3); the differing oxygen bonding structures promote different van der Waals forces which would significantly affect the forces driving vesicle rupture. This phenomenon has been shown to exist within published literature; however the exact reason explaining this behavior requires further study.

The second parameter examined was the pH of the buffer solution. Within this work, pH was varied between 8 and 4 and the surfaces examined were γ-alumina and mesoporous YSZ. For a pH of 8, the behavior on the γ-alumina film was observed as the formation of a vesicle monolayer. Conversely, changing the pH to 4 had the effect of forming a lipid bilayer with embedded vesicles within the bilayer structure on the γ-alumina film. It is believed that the decrease in pH caused a greater zeta potential difference between the support and vesicles; this increased zeta potential difference is believed to induce greater attractive forces between the support and vesicles thus driving vesicle rupture upon adsorption. Contrary to the γ-alumina film, the mesoporous YSZ film experienced vesicle monolayer adsorption regardless of the buffer pH used. However, a decrease in the pH yielded more rapid vesicle adsorption kinetics, a result of the enhanced attractive forces between the vesicles and support driven by the pH change.

The final parameter examined affected the lipid bilayer membrane formation process was the surface roughness of the support surface. This was evaluated by using supports with identical surface chemistries but different surface roughness properties. It was found that vesicle monolayer adsorption was more rapid on the macroporous YSZ film when compared to the mesoporous film. This can be explained by the disjointed nature of the mesoporous film which decreased the continuous surface area available to vesicle adsorption. Dense SiO_2 and porous zeolite were compared and it was found that a planar lipid bilayer membrane was formed on both SiO_2 surfaces. Quantitatively, the formation process required additional time on the zeolite film due to the increased available surface area.

This is the first systematic study examining the formation of lipid structures on these four porous inorganic support materials. It is also the first study to examine various parameters such as buffer pH and high surface roughness (over 5 nm) to determine their effect on the kinetic vesicle adsorption process.

The second objective was to characterize the formation and transport behavior of lipid bilayer membranes on cylindrical supports. In Chapter 3, a novel sensing technique, long-period fiber grating (an optical fiber sensing platform), was utilized to monitor the lipid bilayer membrane formation process on the cylindrical supports. A double grating system was fabricated in order to account for environmental fluctuations that could affect the kinetic measurements. Double grating functionality was monitored through exposure to air and water to measure the wavelength shift between these two materials with varying refractive indices. Grating independence was measured through incremental introduction of isopropanol to the first grating while the second grating remained in a constant water solution; this test proved that there was an insignificant wavelength shift in the second grating while a grating 1 experienced a significant wavelength shift with a high refractive index change ($\Delta n = 0.01$). Gratings were found to behave very similarly when each exposed to a water bath.

Using the double grating system, it was observed that the lipid membrane was synthesized on the cylindrical support within 3 minutes, which is comparable to the formation process on a dense planar support of the same chemistry; these results verify that a lipid bilayer was formed on the support surface. The formation process of a Gramicidin incorporated membrane was also tested using the double grating system. It was found that the presence of Gramicidin did not affect the formation rate of a lipid bilayer membrane; this is consistent with published results [Ganeli et al., 2003]. The Gramicidin membrane system showed a larger wavelength shift, which is indicative of a denser adsorbed film. The increased density can be attributed to the addition of Gramicidin molecules within the bilayer membrane.

The transport behavior of the fiber supported lipid bilayer membrane was evaluated through experimentation and theoretical modeling, as detailed in Chapter 4. Theoretical modeling was used to model the unsteady state two directional diffusion behavior on the surface of the fiber; the numerical solution was obtained using ANSYS. The model system demonstrated that the measured diffusion coefficient was dependent on the location chosen for measurement on the optical fiber support; theoretical results were confirmed with experimental data. These results are significant, since it is found that the measurement location on the three dimensional surface affects the diffusivity coefficient; the measurement location must be accounted in order to correctly understand diffusion behavior.

This work is the first reported study detailing the use of a novel double grating system, which is useful for accurately measuring dynamic processes. Additionally, this is the first work elucidating the formation process of a lipid bilayer membrane system on cylindrical supports. The information presented in this study will be valuable to supported lipid bilayer membrane biosensing technology, as it will allow for easy and direct application to support lipid bilayer membrane sensing technology.

5.2. Recommendations

Based on the experimental and theoretical studies in this dissertation, the following recommendations are made for future research.

This dissertation has shown the vesicle adsorption and rupture kinetics on porous inorganic supports. This work illustrated that small range of materials formed a planar lipid bilayer membrane system under specific conditions. Further study should be conducted to evaluate the effect of various parameters to further the study of the formation of lipid bilayer membranes as the formation of adsorbed vesicle monolayers was more prevalent in this work.

As discussed in Chapter 1, the overall membrane charge significantly influences the final structure of the lipid bilayer membrane. Richter et al. [Richter et al., 2006] found that increasing the positive character of the membrane transitioned the final structure from zero deposition to a lipid bilayer membrane. Because zwitterionic lipids were explored in this work, positively charged lipids could be used in membrane synthesis to determine if a lipid membrane structure can be achieved on films with pure vesicle adsorption without rupture seen in this work. Additional parameters promoting rupture that can be varied such as the inclusion of fusogenic divalent ions, such as Ca^{2+} or Mg^{2+}, within the buffer solution. These ions are particularly effective with zwitterionic or negatively charged lipids as they are believed to "bridge" the negative to charge which would promote vesicle rupture [Richter et al., 2003].

Another extension of porous supported lipid bilayer membranes is to conduct transmembrane gradient studies. While supported on a dense QCM crystal facilitates measurement of lipid bilayer membrane formation or monolayer vesicle deposition, the dense support does not promote transmembrane flow. All porous thin films explored in this work are typically supported on α-alumina supports [O'Brien-Abraham, 2007]. Chapter 3 demonstrated the successful inclusion of gramicidin within the bilayer structure, thus a natural extension would be to examine the transport properties through the membrane. Therefore, the combination of α-alumina supported porous thin films and Gramicidin incorporated lipid bilayer membranes would allow for studying ion transport through lipid membrane.

The second objective of this dissertation is to understand the fundamental formation and transport behavior of lipid bilayer membranes supported on a cylindrical fibrous support. A comprehensive understanding of the membrane behavior is very beneficial because it allows for direct application to biosensing technology. The results found in the work can easily extend to supported lipid membrane sensing technology coupled with long period fiber grating technology. Because the sensing principle is depending on the surface refractive index, the ideal sensing configuration is to study surface binding events. This can yield high quality information regarding binding kinetics in a very simple and low-cost configuration with a very high time resolution.

REFERENCES

Abel, A.P., Weller, M.G., Duveneck, G.L., Ehrat, M., & Widmer, H.M. (1996) Fiber-optic evanescent wave biosensor for the detection of oligonucleotides. *Analytical Chemistry, 68,* 2905-2915.

Alvarez-Leefmans, Francisco, J.; & Delpire, Eric. (2009). *Physiology and pathology of chloride transporters and channels in the nervous system: From Molecules to Diseases.*, China: Academic Press.

ANSYS Inc. Guide to ANSYS User Programmable Features. Southpointe. USA, 2004.

Axelrod, D., Koppel, D.E., Schlessinger, J., Elson, E., & Webb, W.W. (1976) Mobility measurement by analysis of fluorescence photobleaching recovery kinetics. *Biophysical Journal, 16,* 1055-1070.

Baksh, M.M., Jaros, M., & Groves, J.T. (2004). Detection of molecular interactions at membrane surfaces through colloid phase transitions. *Nature, 427,* 139-141.

Bayerl, T.M., & Bloom, M. (1990). Physical properties of single phospholipid bilayers adsorbed to micro glass beads. A new vesicular model system studied by 2H-nuclear magnetic resonance. *Biophysical Journal, 58,* 357-362.

Bird, R.B., Stewart, W., Lightfoot, E.N. (2007). *Transport Phenomena*, 2nd Ed., New York: John Wiley and Sons. Equation B.11-2,

Brian, A.A., & Mcconnell, H.M. (1984). Allogeneic stimulation of cytotoxic T cells by supported planar membranes. *PNAS: Proceedings of the National Academy of Sciences, 81,* 6159-6163.

Buranda, T., Huang, J., Ramarao, G.V., Ista, L.K., Larson, R.S., Ward, T.L., Skylar, L.A., & Lopez, G.P. (2003). Biomimetic molecular assemblies on glass and mesoporous silica microbeads for biotechnology. *Langmuir, 19,* 1654-1663.

Busca, G., Lorenzelli, V., Ramis, G., & Willey, R.J. (1993). Surface sites on spinel-type and corundum-type metal oxide powders. *Langmuir, 9,* 1492-1499.

Campbell, M.K., Farrell, S.O. *Biochemistry*. (2003), 4th ed. United States: Thomson.

Castellana, E.T. & Cremer, P.S. (2006) Solid supported lipid bilayers: From biophysical studies to sensor design. *Surface Science Reports, 61*, 429–444.

Chang, C.H., Gopalan, R., & Lin., Y.S. (1994). A comparative study on thermal and hydrothermal stability of alumina, titania and zirconia membranes. *Journal of Membrane Science, 91*, 27-45.

Chen, X., Zhang, L., Zhou, K., Davies, E., Sugden, K., Bennion, I., Hughes, M., & Hine, A. (2007) Real-time detection of DNA interactions with long-period fiber-grating-based biosensor. *Optics Letters, 32*, 2541-2543.

Colloidal Dynamics (1999) The Zeta Potential. Electroacoustics Tutorials. www.colloidal-dynamics.com. Accessed 2009.

Cooper, C.A. & Lin, Y.S. (2007). Synthesis and characterization of silicalite powders and membranes with micro–meso bimodal pores. *Journal of Material Science, 42*, 320–327.

Corres, J.M., Matias, I.R., Goicoechea, J., Arregui, F.J., Viegas, D., Araújo, F.M., & Santos, J.L. (2008). Experimental results of antigliadin antibodies detection using long period fiber grating. *Proceedings of SPIE, the international society for optical engineering*. 7004, 700442.

Cowster, H.G.L. (2003) Dielectric and electrical properties of lipid bilayers in relation to their structure. *Planar lipid bilayers (BLMs) and their applications*, Tien, H.T., Ottova-Leitmannova, A., eds., Elsevier, Amsterdam.

Cowster, H.G.L., & Smith, J.R. (1974). Molecular organization of bimolecular lipid-membranes – study of low-frequency Maxwell-Wagner impedance dispersion. *Biochimica Biophysica Acta, 373*, 151-164.

Cremer, P.S., & Boxer, S.G. (1999). Formation and spreading of lipid bilayers on planar glass supports. *Journal of Physical Chemistry B, 103*, 2554-2559.

Domínguez Crespo, M.A., García Murillo, A., Torres-Huerta, A.M., Yanez-Zamora., C., de.J. Carrillo-Romo., F. (2009). Electrochemical behaviour of ceramic yttria stabilized zirconia on carbon steel synthesized via sol–gel process. *Journal of Alloys and Compounds, 483*, 437–441.

Egawa, H. & Furusawa, K. (1999). Liposome adhesion on mica surface studied by atomic force microscopy. *Langmuir, 15*, 1660-1666.

Erdogan, T. (1997). Fiber grating spectra. *Journal of Lightwave Technology, 15,* 1277-1294.

Fatourous, D.F., Klepetsanis, P., Ioannou, P.V. & Antimisiaris, S.G. (2005). The effect of pH on the electophoretic behavior of a new class of liposomes: arsonoliposomes. *International Journal of Pharmaceutics, 288,* 151-156.

Flicke.W., (1998) *Industrial Solvents Handbook,* 5th ed, p 397. Retrieved 2011, from www.knovel.com.ezproxy1.lib.asu.edu.

Funke, H.H., Kovalchick, M.G., Falconer, J.L., & Noble, R.D. (1996). Separation of hydrocarbon isomer vapors with silicalite zeolite membranes. *Industrial & Engineering Chemistry Research, 35,* 1575-1582.

Fricke, H., (1925). *The Journal of General Physiology*, *9*, 137.

Ganeli, A., Rydstrom, J., Kasemo, B., & Hook, F. (2003). Formation of supported lipid bilayer membranes on SiO2 from proteoliposomes containing transmembrane proteins. *Langmuir, 19,* 842-850.

Gennis, R. B. (1989) *Biomembranes: Molecular structure and function,* Springer-Verlag, New York.

Girard-Egrot, A.P., Blum, L.J. *Langmuir-Blodgett Technique for Synthesis of Biomimetic Lipid Membranes,* in Martin, D.K., eds, *Nanobiotechnology of biomimetic membranes.* (2007) Springer, New York.

Goksu, E.I., Hoopes, M.I., Nellis, B.A., Xing, C., Faller, R., Frank, C.W., Risbud, S.H., Satcher, J.H. Jr., Longo, M.L. (2010) Silica xerogel/aerogel-supported lipid bilayers: Consequences of surface corrugation. *Biochimica et Biophysica Acta 1798*, 719–729

Groves, J.T., & Boxer, S.G. (1995). Electric field-induced concentration gradients in planar supported bilayers. *Biophysical Journal, 69,* 1972-1975.

Groves, J.T.; Ulman, N.; Cremer, P.S., Boxer, S.G. (1998). Substrate-membrane interactions: mechanisms for imposing patterns on a fluid bilayer membrane. *Langmuir, 14,* 3347-3350.

Han, X., Studer, A., Sehr, H., Geissbuhler, I., Di Berardino, M. Winkler, F.K. & Tiefenaur., L.X. (2007). Nanopore arrays for stable and functional free-standing lipid bilayers. *Advanced Materials, 19,* 4466-4470.

Hauser, H., Pasher, I., Pearson, R.H., & Sundell, S. (1981). Preferred conformation and molecular packing of phosphatidylethoanolamine and phosphatidylcholine. *Biochimica et Biophysica Acta*, *650,* 21-51.

Hennesthal, C., & Steinem, C. (2000). Pore-spanning lipid bilayers visualized by scanning force microscopy. *Journal of the American Chemical Society*, *122*, 8085-8086.

Hetzer, M., Heinz, S., Grage, S., & Bayerl, T.M. (1998). Assymetric molecular friction in supported phospholipid bilayers revealed by NMR measurements of lipid diffusion. *Langmuir, 14,* 982-984.

Hinterdorfer, P., Baber, G., & Tamm, L.K. (1994). Reconstitution of membrane fusion sites. A total internal reflection fluorescence microscopy study of influenza hemagglutinin-mediated membrane fusion. *Journal of Biological Chemistry, 269,* 20360-20368.

Hladky, S.B., & Gruen D.W.R. (1982). Thickness fluctuations in black lipid-membranes. *Biophysical Journal, 38,* 251-258.

Hench, L.L., Wilson, J. Introduction in : Hench, L.L., & Wilson, J. (Eds.), (1993) *The Use of Alumina and Zirconia in Surgical Implants,* World Scientific: Singapore, 1-24.

Hulbert, S.F. Introduction to bioceramics, in: Hench, L.L., Wilson, J. (Eds.), *The Use of Alumina and Zirconia in Surgical Implants,* World Scientific:Singapore, 1993, pp. 25-40.

Ide, T., & Ichikawa, T. (2005). A novel method for artificial lipid-bilayer formation. *Biosensors and Bioelectronics, 21,* 672-677.

Jass, J., Tjarnhage, T., & Puu, G. (2000). From liposomes to supported, planar bilayer structures on hydrophilic and hydrophobic surfaces: an atomic force microscopy study. *Biophysical Journal*, *79*, 3153-3163.

Johnson, J.M, Ha, T., Chu, S., & Boxer, S.G. (2002). Early steps of supported bilayer formation probed by single vesicle fluorescence assays. *Biophysical Journal, 83,* 3371-3379.

Karolis, C., Coster, H.G.L., Chilcott, T.C., & Barrow, K.D. (1998). Differential effects of cholesterol and oxidized-cholesterol in egg lecithin bilayers. Biochimica et *Biophysica Acta, 1368,* 247-255.

Keller, C.A., & Kasemo, B. (1998). Surface specific kinetics of lipid vesicle adsorption measured with a quartz crystal microbalance. *Biophysical Journal, 75,* 1397-1402.

Keller, C.A., Glasmastar, K., Zhdanov, V. P., & Kasemo, B. (2000). Formation of supported membranes from vesicles. *Physical Review Letters, 84,* 5443-5446.

Kim, J. & Lin., Y.S. (1998). Sol-gel synthesis and characterization of yttria stabilized zirconia membranes. *Journal of membrane science, 139,* 75-83.

Kim, J. & Y. S. Lin. (1999). Synthesis and characterization of suspension-derived, porous ion-conducting ceramic mkembranes. *Journal of the America Chemical Society, 82,* 2641–46

Klee, B., Duveneck, G.L., Oroszlan, P., Ehrat, M., & Widmer, H.M. (1995). A model system for the development of an optical biosensor based on lipid membranes and membrane-bound receptors. *Sensors & Actuators B-Chemical, 29,* 307-311.

Knoll, W., (1998). Interfaces and thin films as seen by bound electromagnetic waves. *Annual Review of Physical Chemistry, 49,* 569-638.

Larson, C., Rodahl, M., & Hook, F. (2003). Characterization of DNA immobilization and subsequent hybridization on a 2D arrangement of streptavidin on a biotin-modified lipid bilayer supported on SiO2. *Analytical Chemistry, 75,* 5080-5087.

Lei, S.B., Tero, R., Misawa, N., Yamamura, S., Wan, L.J., & Urisu, T. (2006). AFM characterization of gramicidin-A in tethered lipid membrane on silicon surface.
Chemical Physics Letters, 429, 244-249.

Lin, Y.S., Kumakiri, I., Nair, B.N., & Alsyouri, H. (2002). Microporous inorganic membranes. *Separation and Purification Methods, 31,* 229–379.

Linseisen, F.M., Hetzer, M., Brumm, T., & Bayerl, T.M. (1997). Differences in the physical properties of lipid monolayers and bilayers on a spherical solid support. *Biophysical Journal, 72,* 1659-1667.

Liu, N., Gao, Z., Zhou, H.Y., & Yue, M. (2007). Detection of SEB gene by bilayer lipid membranes nucleic acid biosensor supported by modified patch-clamp pipette electrode. *Biosensors and Bioelectronics*, *22*, 2371–2376.

Lovallo, M.C., & Tsapatsis, M. (1996). Preferentially Oriented Submicron Silicalite Membranes. *Separations, 42,* 3020-3029.

Lu, X.D., Ottova, A.L., & Tien, H.T. (1996). Biophysical aspects of agar-gel supported bilayer lipid nembranes: a new method for forming and studying planar bilayer lipid membranes. *Bioelectrochemistry and Bioenergetics, 39,* 285-289.

Macedo, M.I.F, Osawa, C.C. & Bertran, C.A. (2004). Sol-gel synthesis of transparent alumina gel and pure gamma alumina by urea hydrolysis of aluminum nitrate. *Journal of Sol-Gel Science and Technology, 30,* 135–140,

Mao, A., Liao, Y., Zhang, M., Lai, S., & Yin, H. (2007). A novel optical fiber biochemical sensor based on long period grating. *Proceedings of SPIE, the international society for optical engineering. 6757,* 67570M.

Martin, D.K. *Nanobiotechnology of biomimetic membranes*. New York: Springer, 2007.

Neher, E., & Eibl, H. (1977). Influence of phospholipid polar groups on gramicidin channels. *Biochimica et Biophysica Acta, 363,* 37-44.

Nellis, B.A., Satcher, J.H. Jr., Risbud, S.H. (2011). Phospholipid bilayer formation on a variety of nanoporous oxide and organic xerogel films. *Acta Biomaterialia, 7*, 380–386.

Noack, M., Kölsch, P., Dittmar, A., Stöhr, M., Georgi, G., Eckelt, R., et al. (2006). Effect of crystal intergrowth supporting substances (ISS) on the permeation properties of MFI membranes with enhanced Al-content. *Microporous Mesoporous Materials , 97*, 88-96.

Nollert, P., Kiefer, H., & Jahnig, F. (1995). Lipid vesicle adsorption versus formation of planar bilayers on solid surfaces. *Biophysical Journal, 69,* 1447-1455.

O'Brien-Abraham, J., Kanezashi, & M., Lin., Y.S. (2007). A comparative study on permeation and mechanical properties of random and oriented MFI-type zeolite membranes. *Microporous and Mesoporous Materials, 105,* 140–148.

van Oudenaarden, A., & Boxer, S.G. (1999). Brownian ratchets: molecular separations in lipid bilayers supported on patterned arrays. *Science, 285,* 1046-1048.

Paddle, B.M. (1996). Biosensors for chemical and biological agents of defense interest. *Biosensors and Bioelectronics, 11,* 1079-1113.

Peterson, I.R. (1990). Langmuir blodgett films. *Journal of Physics, 23,* 379-395.

Pina, M.P., Mallada, R., Arruebo, M., Urbiztondo, M. Navascues, N., de la Iglesia, O., & Santamaria, J. (2011). *Microporous and Mesoporous Materials,* doi:10.1016/j.micromeso.2010.12.00

Plant, A.L. (1999). Supported hybrid bilayer membranes as rugged cell membrane mimics. *Langmuir, 15,* 5128-5135.

Purrucker, O., Hillebrandt, H., Adlkofer, K., & Tanaka, M. (2001). Deposition of highly resistive bilayer on silicon-silicon dioxide electrode and incorporation of gramicidin studied by ac impedance. *Electrochimica Acta, 47,* 791-798.

Puu, G., & Gustafson, I. (1997). Planar lipid bilayers on solid supports from liposomes – factors of importance for kinetics and stability. *Biochimica et Biophysica Acta, 1327,* 149–161.

Reimhult, E., Hook, F., & Kasemo, B. (2002). Vesicle adsorption on SiO_2 and TiO_2 : dependence on vesicle size. *Journal of Chemical Physics, 117,* 7401-7404.

Reimhult, E., Hook, F., & Kasemo, B. (2003). Intact vesicle adsorption and supported biomembrane formation from vesicles in solution: influence of surface chemistry, vesicle size, temperature and osmotic pressure. *Langmuir, 19,* 1681-1691.

Reimhult, E., & Kumar, K. (2008). Membrane biosensor platforms using nano- and microporous supports. *Trends in Biotechnology, 26,* 82-89.

Reimhult, E. Doctoral Dissertation. (2006). On the formation of supported phospholipid bilayers. Chalmers University: Sweden.

Reviakine, I., & Brisson, A. (2000). Formation of supported phospholipid bilayers from unilamellar vesicles investigated by atomic force microscopy. *Langmuir, 16,* 1806-1815.

Richter, R., Mukhopadhyay, A., & Brisson, A. (2003). Pathways of lipid vesicle deposition on solid surfaces: a combined QCM-D and AFM study. *Biophysical Journal, 85*, 3035-3047.

Richter, R.P., Berat, R., & Brisson, A.R. (2006). Formation of solid-supported lipid bilayers: an integrated view. *Langmuir, 22*, 3497-3505.

Rodahl,, M., Hook, F., Fredriksson, C., Keller, C.A., Krozer, A., Brzezinski, P., Voinova, M., Kasemo, B. (1997).Simultaneous frequency and dissipation factor QCM measurements of biomolecular adsorption and cell adhesion. *Faraday Discussions, 107,* 229-246.

Rokhina, E.V., Lens, P., Virkutyte, J., (2009). Low-frequency ultrasound in biotechnology: state of the art. *Trends in Biotechnology, 27,* 298 – 306.

Sackmann, E. (1996). Supported membranes: scientific and practical applications. *Science, 271,* 43-48.

Sackmann, E., & Tanaka, M. (2000). Supported membranes on soft polymer cushions: fabrication, characterization and applications. *Trends in Biotechnology, 18,* 58-64.

Salafsky, J., Groves, J.T., & Boxer, S.G., (1996). Architecture and function of membrane proteins in planar supported bilayers: a study of photosynthetic reaction centers. *Biochemistry, 35,* 14773-14781.

Salamon Z., & Tollin, G. (2001). Optical anisotropy in lipid bilayer membranes: coupled plasmon-waveguide resonance measurements of molecular orientation, polarizability, and shape. *Biophysical Journal, 80*, 1557-1567.

Salamon, Z., & Tollin, G. (1996a). Surface plasmon resonance studies of complex formation between cytochrome c and bovine cytochrome c oxidase incorporated into a supported planar lipid bilayer. I. Binding of cytochrome c to cardiolipin/phosphatidylcholine membranes in the absence of oxidase. *Biophysical Journal, 71,* 848-857.

Salamon, Z., & Tollin, G. (1996b). Surface plasmon resonance studies of complex formation between cytochrome c and bovine cytochrome c oxidase incorporated into a supported planar lipid bilayer. II. Binding of cytochrome c to oxidase-containing cardiolipin/phosphatidylcholine membranes. *Biophysical Journal, 71,* 858-867.

Saravanan, L., & Subramanian, S. The importance of zeta potential in ceramic processing (2) Zirconia. Malvern Instruments. Application Note. MRK709-01.

Schmitt, E.K., Nurnabi, M., Bushby, R.J., & Steinem, C. (2008) . Electrically insulating pore-suspending membranes on highly ordered porous alumina obtained from vesicle spreading. Soft Matter, 2008, 4, 250–253

Schneider, M.S., Jenkins, J.T., & Wedd, W.W. (1984). Thermal fluctuations of large quasi-spherical bimolecular phospholipid vesicles. *Journal de Physique, 45,* 1457-1472.

Schonherr, H., Johnson, J.M., Lenz, P., Frank, C.W., & Boxer, S.G. (2004). Vesicle adsorption and lipid bilayer formation on glass studied by atomic force microscopy. *Langmuir, 20,* 11600-11606.

Scott, M.J., & Jones, M.N. (2002). A microcalorimetric study of the interaction of phospholipid liposomes with colloidal titanium dioxide and silica: an example of enthalpy–entropy compensation. *Colloids Surface A, 207,* 69-79.

Seantier, B., Breffa, C., Felix, O., & Decher, G. (2004). In situ investigations of the formation of mixed supported lipid bilayers close to the phase transition temperature. *Nanoletters,4,* 5-10.

Shouten, S., Stroeve, P. & Longo M.L. (1999). DNA adsorption and cationic bilayer deposition on self-assembled monolayers. *Langmuir, 15,* 8133-8139.

Simon, A., Girard-Egrot, A., Sauter, F., Pudda, C., Picollet D’Hahan, N., Blum , L., Chatelain, F. & Fuchs., A. (2007). Formation and stability of a suspended biomimetic lipid bilayer on silicon submicrometer-sized pores. *Journal of Colloid and Interface Science, 308,* 337–343.

Song, Xiao-Lan. (2005). Study on dispersion and stability for slurry of γ-Al_2O_3 nanoparticles. *Cailiao kexue yu gongyi, 13,* 506-508.

Starr, T.E., & Thompson, N.L. (2000). Formation and characterization of planar phospholipid bilayers supported on TiO_2 and $SrTiO_3$ single crystals. *Langmuir, 16,* 10301-10308.

Stelzel, M., Miehlich, R., & Sackmann, E. (1992). Two-dimentional microelectrophoresis in supported lipid bilayers. *Biophysical Journal, 63,* 1346-1354

Stroumpoulis, D., Parra, A., & Tirrell, M. (2006). A kinetic study of vesicle fusion on silicon dioxide surfaces by ellipsometry. *AIChE Journal, 52,* 2931–2937.

Subramaniam, A.B., Lecuyer, S., Ramamurthi, K.S., Losick, R., & Stone, H.A. (2010). Particle/Fluid Interface Replication as a Means of Producing Topographically Patterned Polydimethylsiloxane Surfaces for Deposition of Lipid Bilayers. *Advanced Materials, 22,* 2142–2147

Tamm, L. K., & McConnell, H.M. (1985). Supported phospholipid bilayers. *Biophysical Journal, 47*, 105–113.

Tanaka, M., & Sackmann, E. (2005). Polymer-supported membranes as models of the cell surface. *Nature, 437,* 656-664.

Tang, Z., Dong, J., & Nenoff, T.M. (2009). Internal surface modification of MFI-type zeolite membranes for high selectivity and high flux for hydrogen. *Langmuir, 25,* 4848–4852.

Tazawa, H., Kanie, T., & Katayama, M. (2007). Fiber-optic coupler based refractive index sensor and its application to biosensing. *Applied Physics Letters, 91,* 113901.

Tien, H. T. (1995). Self-assembled lipid bilayers as a smart material for nanotechnology. *Materials Science & Engineering C-Biomimetic Materials Sensors and Systems, 3,* 7-12.

Tien, H.T., & Ottova, A.L. (2001). The lipid bilayer concept and its experimental realization: from soap bubbles, kitchen sink, to lipid bilayer membranes. *Journal of Membranes Science, 189,* 83-117.

Tien, H. T., Ottova-Leitmannova, A. (2003) The lipid bilayer concept: Experimental realization and current applications, Tien, H.T., Ottova-Leitmannova, A., eds., *Planar lipid bilayer (BLMs) and their applications,* Elsevier, Amsterdam.

Tien, H.T., & Salamon, Z. (1989). Formation of self-assembled lipid bilayers on solid substrates. *Bioelectrochemistry and Bioenergetics, 22,* 211-218.

Tjarnhage, T., Puu, G. (1996). Liposome and phospholipid adsorption on a platinum surface studied in a flow cell designed for simultaneous quartz crystal microbalance and ellipsometry measurements. *Colloids and Surfaces B: Biointerfaces 8,* 39-50.

Uto, M., Araki, M., Taniguchi, T., Hoshi, S., & Inoue, S. (1994). Stability of an agar-supported bilayer lipid membrane and its application to a chemical sensor. *Analytical Sciences, 10,* 943-946.

Valenzuela, Stella. (2007). Liposome techniques for synthesis of biomimetic lipid membranes. in Martin, D.K., *Nanobiotechnology of biomimetic membranes.* Springer, New York,

Wagner, M.L., & Tamm, L.K. (2007). Tethered polymer-supported planar lipid bilayers for reconstitution of integral membrane proteins: silane-polyethyleneglycol-lipid as a cushion and covalent linker. *Biophysical Journal, 79,* 1400-1414.

Weng, K.C., Stalgren, J.J.R, Duval, D.J., Risbud, S.H., & Frank, C.W. (2004). Fluid biomembranes supported on nanoporous aerogel/xerogel substrates. *Langmuir, 20,* 7232-7239.

Weng, K.C., Stalgren, J.J.R, Risbud, S.H., & Frank, C.W. (2004). Planar bilayer lipid membranes supported on mesoporous aerogels, xerogels, and vycor® glass: an epifluorescence microscopy study. *Journal of Non-crystalline Solids, 350,* 46-53.

Wiedemann, I., Benz,R., & Sahl, H.-G. (2004). Lipid II-Mediated Pore Formation by the Peptide Antibiotic Nisin: a Black Lipid Membrane Study. *Journal of Bacteriology, 186,* 3259-3261.

Wolfbeis, O.S. (2006). Fiber-optic chemical sensors and biosensors. *Analytical Chemistry, 78,* 3859-3873.

Xiao, H., Zhang, L., Dong, J.H., Luo, M., Lee, R., & Romero, V. (2005). Synthesis of MFI zeolite films on optical fibers for detection of chemical vapors. *Optics Letters, 30,* 1270-1272.

Ye, J.Y, Myaing, M.T., Norris, T.B., Thomas, T., & Baker Jr., J. (2002). Biosensing based on two-photon fluorescence measurements through optical fibers. *Optics Letters, 27,* 1412-1414.

Zagoni, M., Sandison, M.E., & Morgan, H. (2009). Microfluidic array platform for simultaneous lipid bilayer membrane formation. *Biosensors and Bioelectronics, 24,* 1235-1240.

Zhandov, V.P., & Kasemo, B. (2001). Comments on rupture of adsorbed vesicles. *Langmuir, 17,* 3518-3521.

Zhang, J., Dong, J., Luo, M., Xiao, H., Murad, S., & Normann, R.A. (2005). Zeolite-fiber integrated optical chemical sensors for detection of dissolved organics in water. *Langmuir, 21,* 8609–8612.

Zhao, Y.T., Zhang, Z., Dai, Q.X., Lin, D.Y., Li., S.M. (2006). Microstructure and bond strength of HA(+ZrO_2+Y_2O_3)/Ti6Al_4V composite coatings fabricated by RF magnetron sputtering. *Surface & Coatings Technology, 200,* 5354 – 5363.

Zwang, T.J., Fletch, W.R., Lane, T.J., & Johal, M.S. (2010). Quantification of the layer of hydration of a supported lipid bilayer. *Langmui*r, *26*, 4598–4601.

APPENDIX A

SYNTHESIS OF VESICLES

1. Cover clean test tube with aluminum foil to minimize light exposure to sample during preparation.
2. Place lipid mixture* within aluminum foil - covered test tube.
3. Angle a stream of inert gas (best to use Argon (UHP is not needed) onto the sample for 10-20 minutes to remove the chloroform solvent.
    a. The flow rate needs to be high enough to expel chloroform, but not so high to disturb the dried lipid film.
4. After chloroform is removed, place sample into a cleaned vacuum oven overnight at 25 in Hg vacuum (temperature must be ambient).
    a. Note: cover window with aluminum foil to minimize light exposure.
5. The next morning, remove the test tube from the vacuum oven and gently pour 5mL buffer solution into the test tube (gently to not disturb lipid film).
6. Cover the test tube with parafilm and aluminum foil. Leave for 1 hour.
7. Vortex test tube for 10 minutes using TouchMixer (setting 10).
8. Remove aluminum foil and parafilm. Place test tube in sonicator bath (Sonicator: Laboratory Supplies) using a ring stand and clamp for 10 – 30 minutes. Remove when solution is clear (indicates small vesicles are formed).

9. After sonication is complete, cover with parafilm and aluminum foil and store in a dark place at ambient temperature (unless storing for extended periods of time).
10. Use promptly. Resonicate before use if 1 hour has passed after sonication.

*Note: the vesicles were made using a lipid:fluorophore ratio of 97:3 only for FRAP analysis

Note: all glassware must be thoroughly cleaned with soap and water and rinsed with 18.2MΩ water before use in experiments

APPENDIX B

CONFOCAL MEASUREMENTS

B-1: SYNTHESIS OF LIPID BILAYER MEMBRANES FOR CONFOCAL MEASUREMENTS

1. Secure clean substrates in the lid of the culture well (35mm glass-bottomed Petri dish with 20mm microwell, Mastek Corporation) using double sided tape.
    a. Substrates are cleaned by sequential sonication in ethanol and water for over 1 hour each.
2. Immerse the substrates in the lipid solution for 60 – 90 minutes. If there is not sufficient concentrated lipid solution in the culture well lids to cover the supports, add additional Tris buffer solution to completely immerse the substrate in liquid.
3. Carefully inject 2-3 mL Tris buffer solution into the lid of the culture well to start lipid dilution. Make sure that the injection does not direct the liquid towards the support surface which may remove the lipid bilayer from the support surface. Likewise, carefully remove 2-3 mL concentrated solution and discard into waste beaker/bottle (this can later be poured down the sink).
4. Exchange a total of 150mL buffer solution to ensure the only lipids in the system are attached to the substrate of interest. This is a very important step to make sure the fluorescence stems only from the supported lipid bilayer membrane.
5. Remove the substrate from the lid of the culture well and place into the bottom of the culture well into the inset to facilitate measurement. Ensure

that only 2 mL liquid is in the culture well to minimize spilling on the microscope.

6. Place culture well on the microscope stage and measure membrane properties.

B-2: DIFFUSION MEASUREMENTS OF SUPPORTED LIPID BILAYER MEMBRANES

Experimental

1. Set-up microscope as instructed by equipment manager (inverted confocal microscope: Doug Daniel, upright confocal microscope: Debra (Page) Baluch

a. If using the NBD-PE tag, the excitation is ~460 nm and emission is 534 nm, so choose lasers (typically a 488 nm (argon) laser) and filters carefully. If incorrectly chosen, fluorescence will not be seen.

2. Choose bleaching region of interest (ROI) on the sample. Within the bleaching program, choose to collect 5-10 fluorescent images prior to bleaching and up to 200 images following bleach (this will ensure steady state has been reached).
3. Bleach the samples with sufficient bleaching iterations to completely remove the fluorescent characteristic of the bleached area.

Data analysis

1. Using ImageJ, open the series of interest using the path: File>Open>“file name”.
2. To analyze image intensity, use the path: Plugins>Time Series Analyzer. Two windows will open: “Time Series_V3_2” and “ROI Manager”.
    a. NOTE: the “Time Series” plug-in needs to be downloaded and installed prior to use (follow instructions accompanying the plug-in).
3. Draw the area of interest on the image and “Add it” in the “ROI manager” popup. Within the “Time Series” window, click “Get Average”. This will output a “Time Trace Average” window with the fluorescence intensity characteristics within the region of interest. Fluorescence data can be obtained through the “list” function.

APPENDIX C

OPTICAL MEASUREMENTS

1. Carefully feed the fiber into the two gas septums of the homemade Teflon liquid incubation cell. Gently tighten the nut to seal the fiber in the cell without any slack in the fiber.

   NOTE: Make sure that the gratings are in the center of the incubation cell.
2. Splice the fiber to fiber connectors using a fiber optic splicer (SUMITOMO TYPE-36). A typical dB loss is <0.5dB.
3. Allow the system to sit overnight to allow the fiber to reach temperature and tension equilibrium.

   NOTE: If conducting liquid experiments, immerse the fiber in water before leaving the system overnight.
4. Verify system stability by measuring the resonance coupling wavelength peak for at least two hours to verify grating stability. Double grating stability occurs when the behavior of both gratings are identical (□□$_r$ = ± 50pm).
5. Synthesize vesicle solution (of desired lipid concentration) using standard procedures (Appendix A). Measure out an identical volume of blank solvent solution (typically Tris buffer solution) as the lipid solution volue. Allow each solution to sit in the room for ~1 hour at a location nearest to the experimental location as possible to allow the liquids to reach temperature equilibrium.
6. Upon optical system stability, simultaneously inject the lipid solution and blank buffer solution into their respective incubation cells. Make sure that

the introduction of the liquids does not occur during a measurement collection cycle.

APPENDIX D

SYNTHESIS OF ZEOLITE FILMS

D-1: SYNTHESIS OF ZEOLITE SEEDS

1. Add 0.7g of NaOH (Aldrich, 99.99%) into 50 mL (1M) TPAOH (Aldrich, Cat.# 25, 253-3) solution which is placed in a 250 mL Teflon flask.
2. Stir until a clear solution is obtained.
3. Turn on the heater.
4. Keep stirring, when the temperature reaches ~80C, add 10g of fumed silica into the solution.
5. Keep stirring until a "clear sol" (homogeneous sol) is obtained (5-10 min).
6. Add ~3 g DI water into the sol.
7. Cool down the synthesis sol to room temperature and place the flask in air for 3 hours (total time for cooling and aging).
8. The flask should be capped throughout preparation.

D-2: SYNTHESIS OF ZEOLITE THIN FILMS

1. Mix zeolite seed solution, HPC, and water (6:3:3).. Shake by hand for one minute. Sonicate the solution using a Cole-Parmer 4800 bath sonicator for 1 hour immediately prior to coating. NOTE: for best results, complete this step immediately prior to coating to prevent agglomerates in solution.
2. Place one or two drops of ethanol in the center of a microscope glass slide. Make sure that only a small amount of ethanol is used as too much will cause ethanol to leak onto the surface of the crystal which will necessitate another substrate cleaning step.

3. Center a clean QCM crystal on the microscope slide with ethanol. Using a low-flow rate of nitrogen, evaporate the ethanol to “seal” the QCM crystal to the microscope slide.
   - Make sure the QCM crystal is centered, otherwise the crystal will break upon rotation.
   - Before the first coating, QCM crystals are cleaned for 45 seconds in a Piranha solution (3:1, H_2SO_4:H_2O_2) at 90 ^{o}C. Crystals are immediately rinsed in H_2O, soaked in water for 30 minutes, and re-rinsed. Surfaces are dried in N_2 and placed in a UVO cleaner for 15 minutes. Crystals are used immediately after UVO.
     - NOTE: Piranha solution is extremely hazardous!!! Use acid gloves, safety glasses and a lab coat at all times while handling material.
4. Upon sealing, immediately place the microscope slide on the spin coater and apply vacuum.
5. Add the zeolite/HPC solution solution drop-wise to cover the QCM crystal surface. Allow the sol to incubate on the QCM surface for 10 seconds. NOTE: make sure there are no air bubbles in the sol within the pipette when coating crystal – this will cause a discontinuous film.
6. Start rotations at 2000 RPM (55 seconds) and 300 RPM (45 seconds). Immediately after completion, remove the microscope slide from the spin coater and detach the QCM crystal from the microscope slide.

7. Immediately place the freshly coated crystal in a humidity chamber at 35-40 ^{o}C for 2.5 days.
8. Calcine the film at 400 ^{o}C for 12 hours (ramp rate = 0.3 ^{o}C).
9. Repeat coating procedure for as many iterations as necessary to create a continuous film.
   - With a zeolite concentration 6x the normal concentration, 2 coats are required to synthesize continuous film.

APPENDIX E

SYNTHESIS OF ZIRCONIA THIN FILMS

E-1: SYNTHESIS OF ZIRCONIA PRECURSOR SOLUTION

1. Make a solution by adding 123 ml of zirconium n-propoxide (Alfa, MW = 327.56 g/mole, 70% purity, 0.25 mole = 116.98 g = 123 mi) into 500 ml of anhydrous isopropanol with stirring at room temperature and in water-free atmosphere (in nitrogen box).
2. Add the solution dropwise to 900 ml deionized water with stirring at 70°C and last 1-2 hours. A white precipitate should form.
3. Filter with vacuum suction and wash the precipitate in water several times.
4. Dilute the product in 1 liter of water and peptize with 125 ml of 1M HNO_3 solution.
5. Refluxing at 90-100°C over night with stirring.
6. Redisperse the sol in an ultrasonic bath for 30 minutes before use.

E-2: SYNTHESIS OF ZIRCONIA THIN FILMS

1. Mix zirconia sol and PVA solution (1g/mL) in a 7:3 volume ratio. Shake by hand for one minute. Sonicate the solution using a Cole-Parmer 4800 bath sonicator for 1 hour immediately prior to coating. NOTE: for best results, complete this step immediately prior to coating to prevent agglomerates in solution.
2. Place one or two drops of ethanol in the center of a microscope glass slide. Make sure that only a small amount of ethanol is used as too much will cause ethanol to leak onto the surface of the crystal which will necessitate another substrate cleaning step..

3. Center a clean QCM crystal (See Appendix D-2-3) on the microscope slide with ethanol. Using a low-flow rate of nitrogen, evaporate the ethanol to “seal” the QCM crystal to the microscope slide. (NOTE: make sure the QCM crystal is centered, otherwise the crystal will break upon rotation).
4. Upon sealing, immediately place the microscope slide on the spin coater and apply vacuum.
5. Add zirconia sol/PVA solution drop-wise to cover the entire QCM crystal surface. Allow the sol to incubate on the QCM surface for 10 seconds. NOTE: make sure there are no air bubbles in sol when coating crystal – this will cause a discontinuous film.
6. Start rotations at 2000 RPM (55 seconds) and 300 RPM (45 seconds). Immediately after completion, remove the microscope slide from the spin coater and detach the QCM crystal from the microscope slide.
7. Immediately place the freshly coated crystal in a humidity chamber at 35-40 ^{o}C for 2.5 days.
8. Calcine the film at 400 ^{o}C for 6 hours (ramp rate = 0.5 ^{o}C).
9. Repeat coating procedure for as many iterations as necessary to synthesize a continuous film.
    - This work found that three coats were required to form a continuous film.

APPENDIX F

SYNTHESIS OF GAMMA ALUMINA THIN FILMS

F-1: SYNTHESIS OF BOEHIMITE SOL

1. Heat while stirring 1 liter of water to 70-90 °C.
2. Weigh 1 mole aluminum-tri-sec-butoxide (ALTSB, Janssen, MW = 246.33 g/mole, 97% purity, 1 mole = 253.95 g = 260 ml) by graduated cylinder.
3. Add the ALTSB into the warm water with a gradually increasing stirring speed and last for 1-2 hours.
4. Keep stirring the solution at 90°C for a half to one hour.
5. Add 70 ml 1M HNO_3 solution into the Boehmite solution
6. Shut off heating, slow down the stirring speed.
7. Reflux at 90-100°C over night (at least 10 hours).

F-2: SYNTHESIS OF □-ALUMINA THIN FILMS

1. Mix boehmite sol and PVA solution (1g/mL) in a 7:3 volume ratio. Shake by hand for one minute. Sonicate the solution using a Cole-Parmer 4800 bath sonicator for 1 hour immediately prior to coating. NOTE: for best results, complete this step immediately prior to coating to prevent agglomerates in solution.
2. Place one or two drops of ethanol in the center of a microscope glass slide. Make sure that only a small amount of ethanol is used as too much will cause ethanol to leak onto the surface of the crystal which will necessitate another substrate cleaning step..

3. Center a clean QCM crystal (See Appendix D-2-3) on the microscope slide with ethanol. Using a low-flow rate of nitrogen, evaporate the ethanol to “seal” the QCM crystal to the microscope slide. (NOTE: make sure the QCM crystal is centered, otherwise the crystal will break upon rotation)
4. Upon sealing, immediately place the microscope slide on the spin coater and apply vacuum.
5. Add boehmite sol/PVA solution drop-wise to cover the entire QCM crystal surface. Allow the sol to incubate on the QCM surface for 10 seconds. NOTE: make sure there are no air bubbles in sol when coating crystal – this will cause a discontinuous film.
6. Start rotations at 2000 RPM (55 seconds) and 300 RPM (45 seconds). Immediately after completion, remove the microscope slide from the spin coater and detach the QCM crystal from the microscope slide.
7. Immediately place the freshly coated crystal in a humidity chamber at 35-40 ^{o}C for 2.5 days.
8. Calcine the film at 400 ^{o}C for 6 hours (ramp rate = 0.5 ^{o}C).
9. Repeat coating procedure for as many iterations as necessary to synthesize a continuous film.
    - This work found that two coats were required to synthesize a continuous film.

APPENDIX G

SYNTHESIS OF YSZ SUSPENSION THIN FILMS

G-1: SYNTHESIS OF YSZ SUSPENSION

1. Mix YSZ powder (8 mol%, Tosoh) and dilute nitric acid (pH=3-4) with the weight ratio of 1 to 2, and put into PE pot with zirconia milling balls.
2. Treat the solution ultrasonically to bresk the agglomerates.
3. Ball-mill for 1 week.
4. Add more dilute nitric acid with the same pH to adjust the powder to solvent ratio to 10 wt%.

G-2: SYNTHESIS OF YSZ THIN FILMS

1. Mix YSZ suspension and PVA solution (1g/mL) in a 7:3 volume ratio. Shake by hand for one minute. Sonicate the solution using a Cole-Parmer 4800 bath sonicator for 1 hour immediately prior to coating. NOTE: for best results, complete this step immediately prior to coating to prevent agglomerates in solution.
2. Place one or two drops of ethanol in the center of a microscope glass slide. Make sure that only a small amount of ethanol is used as too much will cause ethanol to leak onto the surface of the crystal which will necessitate another substrate cleaning step.
3. Center a clean QCM crystal (See Appendix D-2-3) on the microscope slide with ethanol. Using a low-flow rate of nitrogen, evaporate the ethanol to “seal” the QCM crystal to the microscope slide. (NOTE: make sure the QCM crystal is centered, otherwise the crystal will break upon rotation)

4. Upon sealing, immediately place the microscope slide on the spin coater and apply vacuum.
5. Add YSZ suspension/PVA solution drop-wise to cover the entire QCM crystal surface. Allow the sol to incubate on the QCM surface for 10 seconds. NOTE: make sure there are no air bubbles in sol when coating crystal – this will cause a discontinuous film.
6. Start rotations at 2000 RPM (55 seconds) and 300 RPM (45 seconds). Immediately after completion, remove the microscope slide from the spin coater and detach the QCM crystal from the microscope slide.
7. Immediately place the freshly coated crystal in a humidity chamber at 35-40 ^{o}C at 40% relative humidity for 2.5 days.
8. Calcine the film at 400 ^{o}C for 6 hours (ramp rate = 0.5 ^{o}C).
9. Repeat coating procedure for as many iterations necessary to synthesize a continuous film.
    - This work found that two coats were required to make a continuous thin film.

APPENDIX H

QCM MEASUREMENTS

1. Place the clean QCM crystal in the QCM flow cell. Tighten the lid and place within the foam piece to minimize vibrations.
2. Allow to reach equilibrium for at least 8 hours to eliminate tension effects induced by tightening the lid onto the cell.
    a. Make sure that the tubing is already connected to the lid. The connection will induce tension on the cell which will require additional time for equilibrium.
3. Inject 1-2 mL H_2O (via syringe) into the measurement cell. Allow to sit for 3-4 hours to ensure that the film is hydrated before measurement (indicated when frequency reaches equilibrium).
4. During stabilization, fill syringes with buffer solution [~20mL and ~18mL] for buffer syringe and lipid syringe.
    a. Minimize handling of the syringes as it will induce temperature variations within the sample.
5. Secure the syringe in the syringe pump. Flow buffer across the crystal surface (50 μL/min) for 1-2 hours until frequency equilibrium is reached.
6. Begin vesicle preparation when buffer flow begins (Appendix A).
7. After vesicle synthesis and frequency stabilization, inject 2mL lipid solution (1mg/mL) into 18mL buffer to yield a final 0.1mg/mL lipid solution.
8. Secure syringe into the second pump. Begin flow to outlet flow using coupled 3-way valves (these coupled valves must be secured using a vice).

9. Once the flow is stabilized from the lipid syringe, stop both syringe pumps and carefully switch the valve to allow the lipid syringe to flow across the QCM cell. Restart the lipid flow.
10. During experiments, keep the lights off and make every effort to make sure that no one enters the room (this will <u>significantly</u> affect results).